T1rho MRI in Brain Aging, Lumbar Disc Degeneration, and Liver Fibrosis: Clinical and Experimental Studies

ZHAO, Feng

A Thesis Submitted in Partial Fulfillment
of the Requirements for the Degree of
Doctor of Philosophy
in
Imaging and Interventional Radiology

The Chinese University of Hong Kong
July 2013

Thesis/Assessment Committee

Professor James F. Griffith (Chair)

Professor Wang Yi-xiang (Thesis Supervisor)

Professor Yuan Jing (Thesis Co-supervisor)

Professor Yeung Ka Wai David (Committee Member)

Professor Lu Gang (Committee Member)

Professor Liu Xin (External Examiner)

論文評審委員會

James F. Griffith 教授 (主席)

王毅翔 教授 (論文導師)

袁璟 教授 (論文共同導師)

Yeung Ka Wai David 教授 (委員)

路剛 (委員)

劉新 教授 (校外委員)

ABSTRACT

T1rho relaxation is spin-lattice relaxation in the rotating frame. It determines the decay of the transverse magnetization in the presence of a spin-lock radiofrequency pulse, which applied along the transverse magnetization. T1rho MRI is sensitive to low frequency motional processes, so it can be used to investigate the interaction between water molecules and their macromolecular environment. T1rho imaging is suggested to have the potential to identify early biochemical changes in tissues.

Aging and chronic hypertension are two major risk factors for common neurodegenerative disease. However, whether normal brain aging and chronic spontaneous hypertensive are associated with brain T1rho values changes were not reported. We longitudinally measured the T1rho value in rat brain of Sprague-Dawley (SD) rats from 5-month to 15-month, and spontaneous hypertensive rats (SHR) with Wistar Kyoto (WKY) rats from 6-month to 12-month. The T1rho values in three brain regions of thalamus, hippocampus, and cortices increased with aging process, and were significantly higher in SHR than WKY rats.

For intervertebral disc, the correlation between T1rho and degenerative grade has been reported. However, whether and how T1rho specifically offer better evaluation of disc degeneration compared with T2 was not studied previously. T1rho and T2

value of nucleus pulposus (NP) and annulus fibrosus (AF) was compared with reference to the five-level and eight-level semi-quantitative disc degeneration grading systems. For NP, T1rho and T2 decreased quadratically with disc degeneration grades and had no significant trend difference (P=0.40). In NP, T1rho and T2 decrease in a similar pattern following disc degeneration. For AF, T1rho and T2 decreased linearly and the slopes of T2 were significantly flatter than those of T1rho (P<0.001). Therefore, the T1rho is better suited for evaluating AF in degenerated disc than T2.

Liver fibrosis, a common feature of almost all causes of chronic liver disease, involves macromolecules accumulated within the extracellular matrix. Male Sprague-Dawley rats received intraperitoneal injection of 2 ml/kg CCl4 twice weekly for up to 6 weeks. Then CCl4 was withdrawn for recovery. The liver T1rho values increased slightly on day 2, then increased further and were highest at week 6 post CCl4 insults, and decreased upon the withdrawal of the CCl4 insult. This study demonstrated that T1rho MRI is a valuable imaging biomarker for liver injury and fibrosis induced by CCl4. Liver T1rho value was only mildly affected by edema and acute inflammation when there was no apparent fibrosis.

To translate liver T1rho MRI to clinical application, the technical feasibility of T1rho MRI in human liver was explored and the normal range of T1rho values in healthy volunteers was determined. We found it is feasible to obtain consistent liver

T1rho measurement for healthy human liver with six spin-lock time (SLT) points of 1, 10, 20, 30, 40, and 50ms; the mean liver T1rho value of the healthy subjects was 42.5ms, with a range of 38.8-46.5ms. Adopting 3-SLT points of 1, 20, and 50ms for T1rho measurement could provide reliable measurement and reduce the scanning time, while 2-SLT points of 1 and 50ms do not provide reliable measurement.

(500 words)

摘要

T1rho 弛豫是旋轉坐標系中的自旋晶格弛豫，它決定橫向磁化向量在存有自旋鎖定射頻脈衝情況下的衰減，自旋鎖定脈衝與橫向磁化向量同向。T1rho 磁共振成像對於低頻運動過程敏感，故可研究水與其周大分子物質環境間的交互作用，有鑒別組織內早期生化改變的潛力。

衰老與慢性高血壓是常見腦退行性疾病的兩個主要危險因素。但是正常腦衰老過程及慢性高血壓兩個因素與腦組織 T1rho 是否有相關性，尚缺乏研究。序貫性測量 SD 老鼠自 5 至 15 月齡、WKY（血壓正常）和 SHR（患有自發性高血壓）老鼠自 6 至 12 月齡的雙側丘腦、海馬、和皮質的腦組織 T1rho 值。發現三組老鼠的丘腦、海馬及皮質的 T1rho 均隨年齡增長而增高；且 SHR 的顯著高於 WKY 老鼠。

T1rho 值與椎間盤退變等級的相關性已有報導。但相比 T2 值，T1rho 在評價椎間盤退變方面是否優於或如何優於 T2 值尚缺乏研究。將椎間盤髓核及纖維環的 T1rho 和 T2 值與 5 級和 8 級椎間盤退變等級系統做比較；發現髓核的 T1rho 及 T2 與椎間盤退變等級的相關性均呈二次函數降低，且無顯著差別(P=0.40)。纖維環的 T1rho 及 T2 與椎間盤退變等級的相關性呈線性函數降低，T2 降低的斜率明顯比 T1rho 降低的斜率要平坦(P<0.001)。故 T1rho 值比 T2 值更加適合評價纖維環退變，而兩者在評價髓核時相似。

肝纖維化是幾乎所有慢性肝病的常見特徵，包括大分子物質在細胞外基質的沉積。選用四氯化碳 CCl4 腹腔注射 6 周來製造肝纖維化模型。肝臟 T1rho 在注射後的第二天輕度上升，然後持續上升，直到注射六周後 T1rho 達最高值，此後 T1rho 隨 CCl4 注射停止而降低。顯示 T1rho 磁共振成像對於監測慢性注射 CCl4 誘導的肝纖維化及肝損傷有價值。當沒有明顯肝纖維化時，肝 T1rho 輕微受水腫及急性炎症的影響。

為將肝臟 T1rho 磁共振成像轉化到臨床使用，我們研究了其可行性，以及正常志願者肝臟 T1rho 值分佈範圍。發現採用六個自旋鎖定時間來測量健康志願者肝 T1rho，結果有較高的可重複性和一致性，肝 T1rho 平均值為 42.5ms，分佈範圍為 38.8 到 46.5ms。採用三個自鎖鎖定時間點掃描，可以減少一半掃描時間，且可以得到可信的肝 T1rho 值，但採用兩個自旋鎖定時間點則不行。

（799 字）

ACKNOWLEDGEMENTS

I would like to express my deepest gratitude to my supervisor Prof. Wang Yi-Xiang for his inspiration, guidance, support and encouragement during the course of my study and preparation of this thesis. He is an enthusiastic scientist, a role model for me. He teaches me not only the knowledge but also the principle on how to become a scientist for exploring the unknowns. I treasure everything I learned from him, which helped me accomplish my study with smoothness and will continue to help me thrive in my future career. Without his continuous support and encouragement, this work would not have been possible.

I would like to acknowledge my co-supervisor Prof. Yuan Jing for his guidance, support and encouragement. Especially in aspect of MRI technology, he gives me great supports. I am grateful for his expert advice and valuable discussion during the years.

Special thanks are extended to Dr. Lu Gang, Dr. Deng Min, Dr. Lau Shuang, Dr. Lau Pi-Chu, Dr. Chu Eagle, Dr. Wang Yong, Dr. Zen Xian-Jun, Dr. He Lai-Chang, Dr. Yu Jian-Wen, and Mr. Qing Wei. Thanks to all of them for helping me throughout my doctoral program, not only in research work, but also in daily life.

I also appreciate the MR staff members of the Department of Imaging and Interventional Radiology in the Chinese University of Hong Kong for their kind

assistance in this work.

Further thanks are due to all the volunteers who participated in this project.

Last but not least, I would like to express my endless gratitude to my parents and my girlfriend, my mother in particular, for their love, understanding and selfless support.

LIST OF FIGURES

coefficient of determination R^2>0.8 evaluation. Five regions of interest (ROIs) are placed on the liver parenchyma region, excluding observable artifacts and blood vessels.

Figure 5.4: The T1rho-weighted images acquired with different spin-lock time (SLT) ranging from 1 to 50ms.

Figure 5.5: One healthy volunteer's T1rho maps constructed using 6-SLT (upper row), 3-SLT (middle row), and 2-SLT (lower row). Left column: coefficient of determination (R^2) maps, middle column: T1rho maps without R^2 evaluation, right column: T1rho maps with R^2>0.8 evaluation. When SLT point decrease, R^2 evaluation is less efficient to remove blood vessel contamination and artifact. When SLT point is 2, the R^2 is always equal to one, so no pixels are excluded by criteria of R^2>0.8.

Figure 5.6: Bland and Altman plots for comparison of 3-SLT v.s. 6-SLT liver T1rho measurement (A) and 2-SLT v.s. 6-SLT liver T1rho measurement (B). 3-SLT measurement demonstrates good agreement with 6-SLT measurement. SLT= spin-lock time.

LIST OF TABLES

LIST OF ABBREVIATIONS

^{1}H	hydrogen proton
^{17}O	oxygen
2D	two-dimensional
3D	three-dimensional
AD	Alzheimer's disease
AF	annulus fibrosus
ANOVA	one-way analysis of variance
B_0	static magnetic field
B_1	radiofrequency field strength
b-FFE	balanced fast field echo
BOLD	blood oxygen level-dependent
B_{SL}	spin-lock radiofrequency strength
C	frontal cortices
CCl4	chronic carbon tetrachloride
CoV	coefficient of variation
CSF	cerebrospinal fluid
CT	computed tomography
ETL	echo train length
FFE	fast field echo
FSL	spin-lock frequency (in Hz)
fMRI	functional magnetic resonance imaging
FOV	field of view
GRE	gradient echo

H	hippocampus
H&E	haematoxylin and eosin
ICC	intraclass correlation coefficient
MTL	medial temporal lobe
MRI	magnetic resonance imaging
NP	nucleus pulposus
NSA	number of signal average
PD	Parkinson's disease
PDD	Parkinson's disease with dementia
PET	positron emission tomography
R^2	coefficient of multiple determinations
RF	radiofrequency
ROI	region of interest
SAR	specific absorption rate
SD	standard deviation
SD rat	Sprague–Dawley rat
SE	spin echo
SHR	spontaneously hypertension rats
SLT	spin-lock time
SPAIR	spectral adiabatic inversion recovery
T	thalamus
T1	spin-lattice relaxation time
$T_{1\rho}$	T1rho
T2	transverse relaxation time
T2*	effective transverse relaxation time

T2WI	T2-weighted image
TE	echo time
TFE	turbo field echo
TI	inversion time
TR	repetition time
TSE	turbo spin echo
WKY rat	Wistar Kyoto rat
γ	gyromagnetic ratio
ω_0	Larmor frequency
ω_{SL}	spin-lock frequency (in rad)

CONTENTS

CHAPTER 1 INTRODUCTION

1.1 Conventional Magnetic Resonance Imaging

1.1.1 Basic Principle of Conventional Magnetic Resonance Imaging

Magnetic resonance imaging (MRI) is a powerful and versatile medical imaging technique and has been widely used in routine clinical practice. Compared with other medical imaging methods such us computed tomography (CT), X-ray, and positron emission tomography (PET), MRI provides high quality images with good soft tissue contrast and has no ionizing radiation. T1-weighted imaging, T2-weighted imaging, and proton-density weighted imaging are three most common imaging motilities for routine clinical application.

Atoms with an odd number of protons and /or odd number of neutrons possess a nuclear spin angular momentum, and therefore exhibit the MR phenomenon. In biological specimens, hydrogen (^1H), with a single proton, is the most abundant (the body consists largely of H_2O), the most sensitive (give rise to the largest signals), and by far the most studied.

In the absence of an external magnetic field, the spins are oriented randomly and the net macroscopic magnetic moment is zero. In the presence of an external magnetic

field B_0, the magnetic moment vectors tend to align in the direction of B_0 (z-direction or longitudinal direction). In addition, the nuclear spins exhibit resonance at a Larmor frequency ω_0. This Larmor frequency is dependent on the applied magnetic field strength, and can be calculated from Larmor Equation:

$$\omega_0 = \gamma B_0 \qquad \text{Equation [1.1]}$$

where γ is the gyromagnetic ratio, a known constant for each type of atom (For ^1H, $\gamma/2\pi = 42.58$ MHz/Tesla).

In the context of magnetic resonance imaging, only oscillating signal can be transmitted and received. To obtain an MR signal, a radiofrequency (RF) pulse B_1 is applied to flip the longitudinal magnetization into the x-y (transverse) plane, exciting these spins out of equilibrium. The strength of B_1 is much weaker than B_0.

1.1.2 T1 Relaxation

Once the RF pulse is turned off, the protons gradually give the energy they obtained from the RF pulse to the surrounding environment and return to the equilibrium state (the magnetization vector along z-axis or longitudinal direction). This process is spin-lattice (T1) relaxation, which is defined by the equation:

$$M_Z(t) = M_0(1 - exp^{(-t/T1)}) \qquad \text{Equation [1.2]}$$

T1 relaxation time is the time constant in milliseconds required for 63%

longitudinal magnetization recovered. Because greater energy exchange is required at higher frequencies, this relaxation effect will take longer at higher fields. Hence T1 values lengthen with increasing B_0.

1.1.3 T2 Relaxation

Meanwhile, transverse magnetization decays due to proton getting out of phase as a result of in-homogeneities in the magnetic field created by adjacent nuclei. This course is spin-spin (T2) relaxation, which is defined by the equation:

$$M_{xy}(t) = M_0(1 - exp^{(-t/T2)}) \quad \text{Equation [1.3]}$$

T2 relaxation time is the time constant in milliseconds required for transverse magnetization decays to 37% of original magnetization.

T1 and T2 relaxation are important MR parameters which have distinct values for different tissues. Based on the differences of T1 and T2 for different tissues, MR images with T1-weighted contrast and T2-weighted contrast can be generated by manipulating MRI pulse sequences and imaging parameters.

1.2 T1rho Magnetic Resonance Imaging

1.2.1 T1rho Relaxation

T1rho (or $T_{1\rho}$) relaxation is fully named as spin-lattice relaxation in the rotating frame, where the subscript 'rho' or 'ρ' indicates the 'rotating' frame. T1rho relaxation

presents a relaxation procedure different from T1 and T2 relaxation. T1rho-weighted contrast provides different or extra information of tissues beyond T1 and T2-weighted contrast.

T1rho relaxation determines the decay of the transverse magnetization in the presence of a spin-lock radiofrequency pulse, of amplitude B_{SL}, aligned with the net magnetization vector.

1.2.2 Principle of T1rho Magnetic Resonance Imaging

As mentioned above, magnetization undergoes T2 relaxation in the transverse plane and decays exponentially due to the dephasing process. However, if an external RF pulse is applied aligned with the spins with the same processing frequency as spins in the transverse plane, the spins are considered stationary relative to this external RF field in the rotating frame. In the presence of this external RF field, spins undergo with a longer relaxation time than the normal T2 relaxation time, which is named as spin-lattice relaxation time in the rotating frame, or T1rho value. This external RF pulse is called spin-lock RF pulse.

In the rotating frame, the spin-lock field plays the role of the B_0 static field in the frame where magnetization undergoes spin-lattice relaxation described by T1. As mentioned above, in T1 relaxation, spin exchange energy with the surrounding lattice

via processes that occur near the Larmor frequency. The spin-lock condition changes the environment in which individual spins are able to interact with the lattice.

In the presence of spin-lock radiofrequency field, spins are able to efficiently couple to the lattice at frequencies close to the nutation frequency of the spin-lock pulse ($\omega_{SL} = \gamma B_{SL}$(in rad), FSL= $\omega_{SL}/2\pi$(in Hz), where γ is the gyromagnetic ratio, for ^1H, $\gamma/2\pi = 42.58$ MHz/Tesla; B_{SL} is the amplitude of the spin-lock pulse, B_{SL} is much smaller than B_0;) which is typically far below the Larmor frequency.

Therefore, the T1rho relaxation time is sensitive to low frequency physic-chemical interactions between water and macromolecules with exchange correlation times and rotational correlation times that are close to the reciprocal of the spin-lock frequency ($1/\omega_{SL}$). Note that although FSL has a unit of Hz as frequency, it is proportional to the spin-lock field strength and used to evaluate the field strength of a spin-lock pulse. Here we could neglect the precession rate of spins with B_0 in the rotating frame because the spin-lock pulse is assumed on-resonance.

1.2.3 Radiofrequency Pulse for T1rho Magnetic Resonance Imaging

The magnetization evolution during a spin-lock pulse cluster is given in Figure 1.1. The initial radiofrequency pulse (P1, $90°_x$) is applied along x-axis (Figure 1.1a), and flips magnetization vector into the transverse plane (Figure 1.1b) from its longitudinal

equilibrium position (Figure 1.1 a). A spin-lock pulse (P_{SL}, y) is applied subsequently along y-axis in the rotating frame with a duration of SLT (spin-lock time) (Figure 1.1c). After the end of the SLT period, the magnetization vector has been decayed according to T1rho relaxation (Figure 1.1d), then a final radiofrequency pulse (P2, $90°_{-X}$) is applied along the negative x axis (Figure 1.1d) to return the T1rho-relaxed transverse magnetization to the longitudinal axis (Figure 1.1e). The resultant T1rho prepared magnetization can be excited and spatially-encoded using a conventional pulse sequence. The M (SLT) vector shortened due to T1rho decay which is described by Equation:

$$\mathrm{M(SLT)} = M_0 \cdot exp^{(-SLT/T1rho)} \quad \text{Equation [1.4]}$$

Where M(SLT) and M_0 is the T1rho-prepared magnetization with the duration of spin-lock and equilibrium magnetization; where SLT is the duration of the spin-lock pulse.

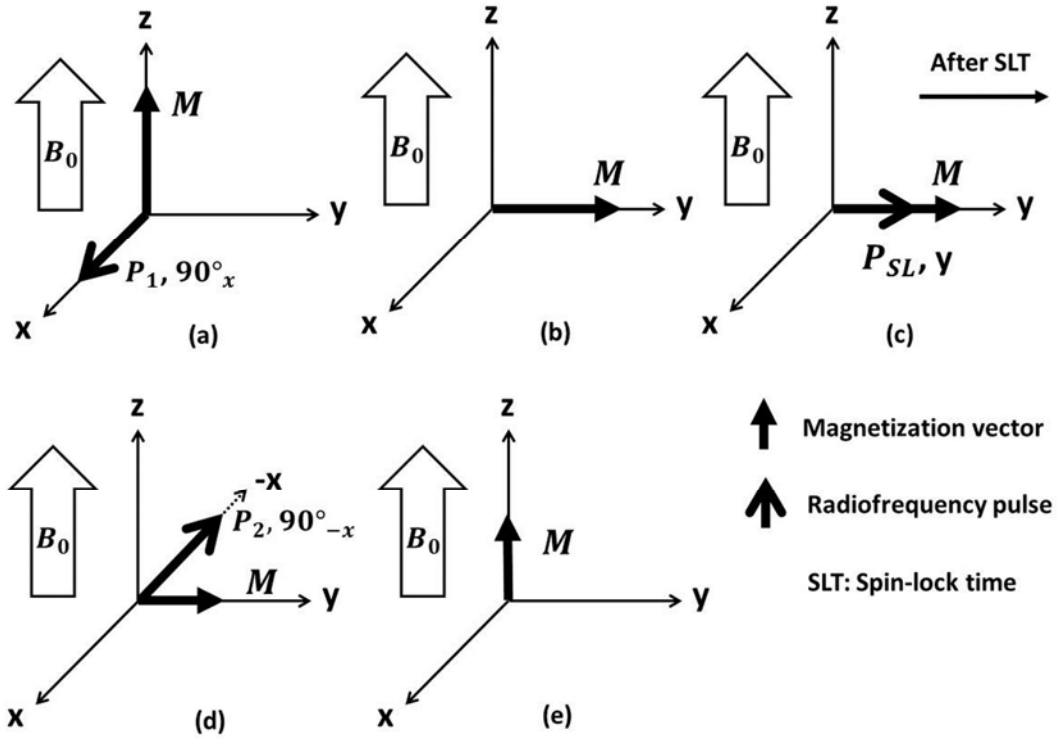

Figure 1.1: The diagram of the magnetization evolution during a spin-lock pulse cluster.

The diagram of a radiofrequency pulse sequence cluster for T1rho preparation is shown in Figure 1.2. Pulse 1(P1) is a hard pulse used to excite the magnetization vector (M) from the longitudinal equilibrium position into the transverse plane along the y-axis. Spin-lock pulse (P_{SL}) is applied parallel to the M vector along the y-axis. ($\theta_y = 2\pi \cdot FSL \cdot SLT$, where FSL is the frequency of spin-lock pulse, SLT is the duration of spin-lock time.) Pulse 2(P2) is a hard pulse used to return the T1rho-relaxed transverse magnetization vector M(SLT) to the longitudinal axis.

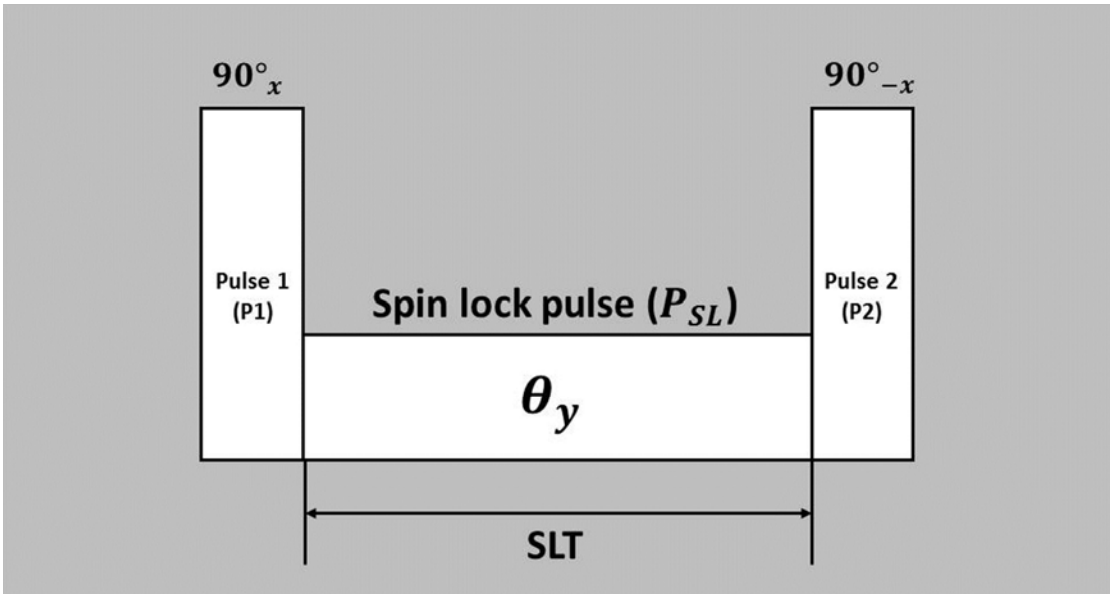

Figure 1.2: The diagram of a radiofrequency pulse sequence cluster for T1rho magnetization preparation. The flip angle of P_{SL} is calculated by $\theta_y = 2\pi \cdot FSL \cdot SLT$.

Because of the relatively long duration of spin-lock pulses, the T1rho method is sensitive to B_1 inhomogeneity. If the magnetization vector is poorly aligned with the spin-lock pulse, there is ample opportunity for it to undergo pronounced off-axis nutation, resulting in an unexpected orientation at the end of spin-lock (Charagundla et al., 2003). The rotary echo spin-lock pulse ("self-compensating" spin-lock pulse) is introduced to reduce the potential image artifacts arising from B_1 inhomogeneity (Charagundla et al., 2003; Solomon, 1959). This spin-lock pulse cluster is given in Figure 1.3, it consists two halves with the equal duration but the opposed phase, and the effectively refocuses the rotation spin-lock phase accumulation.

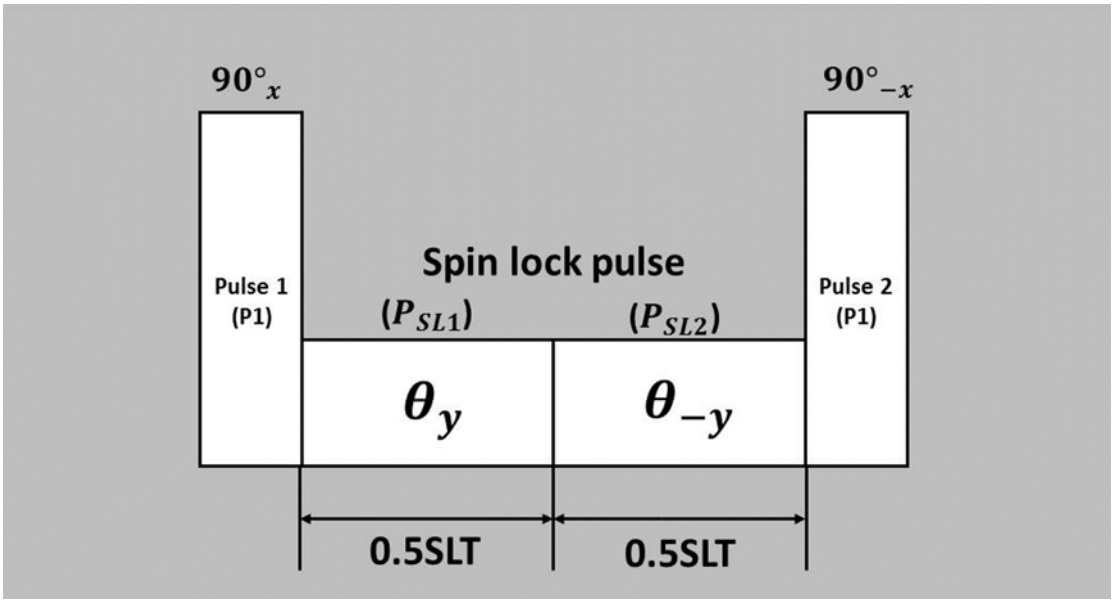

Figure 1.3: The diagram of rotary echo spin-lock pulse cluster for T1rho magnetization preparation. The flip angle of P_{SL} is calculated by $\theta_y = 2\pi \cdot FSL \cdot SLT/2$.

Like any other magnetization preparations such as saturation, inversion and magnetization transfer, T1rho-weighted magnetization preparation itself cannot generate T1rho-weighted MR images unless it is combined with the subsequent pulse sequences to acquire the T1rho-relaxation-prepared MR signal. The T1rho-relaxed magnetization can be acquired by almost any conventional pulse sequence. A block diagram for a typical T1rho imaging experiment is given in Figure 1.4.

At first, a spin-lock pulse is applied for the preparation of T1rho-weighted magnetization. After the T1rho-weighted magnetization is flipped back to the longitudinal plane, the residual transverse magnetization is eliminated by a strong gradient crusher. Then a normal acquisition pulse sequence, like spin echo (SE) type

or gradient echo (GRE) type sequences, either in 2D or 3D, is applied for image acquisition. Finally, a sufficiently long (a couple of times of T1) wait time is often applied after image acquisition to allow magnetization to fully restore in the longitudinal direction for the next T1rho-weighted magnetization preparation.

In addition, other module blocks can be added into the T1rho imaging diagram according to the requirements on specific clinical application. Such us, other magnetization modules of fat suppression or fluid suppression can be applied before or after the spin-lock pulse if necessary.

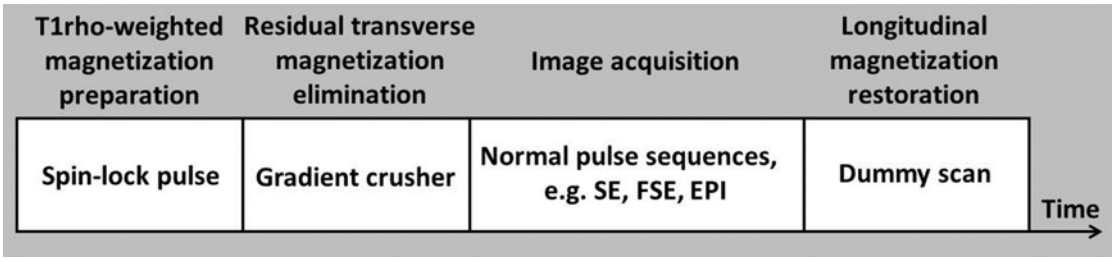

Figure 1.4: Block diagram for a typical T1rho imaging experiment. The purpose of each module is described above the block.

1.2.4 T1rho-weighted Contrast Imaging and Application

T1rho MRI is normally utilized in three forms, including T1rho-weighted contrast imaging, T1rho mapping, and T1rho dispersion imaging.

T1rho-weighted contrast imaging is the most basic form of T1rho MRI. It provides

different or additional tissue contrast information compared with T1 or T2-weighted contrast imaging. With this kind of novel contrast, T1rho-weighted MR images have been used to distinguish breast tumors (Santyr et al., 1989), brain tumors (Aronen et al., 1999; Poptani et al., 2001), head and neck tumors (Markkola et al., 1996), and liver lesions(Halavaara et al., 1998) from healthy tissue. Because muscle has faster relaxation rates and greater magnetization transfer than blood, T1rho-weighted contrast has been used to suppress the background myocardium to enhance myocardium-blood contrast in cardiac imaging (Dixon et al., 1996; Muthupillai et al., 2004; Witschey et al., 2012). Furthermore, T1rho-weighted contrast has also been used for functional MRI (fMRI) to obtain better contrast than the normal T2*-weighted blood oxygen level-dependent (BOLD) contrast (Hulvershorn et al., 2005).

1.2.5 Quantitative T1rho Mapping and Application

A series of T1rho-weighted images acquired at varying duration of SLT (spin-lock time) provide the data for T1rho mapping. The T1rho maps can be calculated on a pixel-by-pixel basis, using a mono-exponential decay with Equation 1.4. T1rho mapping provides versatile quantitative data for making comparisons for different study groups or longitudinally monitoring the progression of T1rho values in same

group. T1rho mapping is the most common form of T1rho imaging and has been most intensively used for various clinical applications.

The number of T1rho-weighted images at different SLT for fitting a single T1rho map is at least two (Yuan et al., 2012). In addition, more T1rho-weighted images at varying SLTs are always used for getting more accurate and precise T1rho maps. However, T1rho MRI is relatively time-consuming due to the long delay time for longitudinal magnetization restoration.

During the recent years, quantitative T1rho MRI has been extensively studied, covering various organs and a wide range of disease processes, particularly in the areas of knee cartilage and intervertebral discs. T1rho mapping was used to quantitative evaluate the cartilage degeneration in the knee joints and intervertebral discs degeneration. The studies indicated that T1rho values are significantly positive correlated with the degree of cartilage degeneration (Nishioka et al., 2012; Regatte et al., 2006; Tsushima et al., 2011), and significantly negative correlated with disc degeneration (Blumenkrantz et al., 2010; Borthakur et al., 2011; Wang et al., 2013a; Wang et al., 2013b). With biliary duct ligation induced rat liver fibrosis model, the recent study showed that MR T1rho imaging is able to detect liver fibrosis, and the degree of fibrosis is correlated with the degree of elevation of the T1rho measurement (Wang et al., 2011a). Furthermore, the quantitative T1rho mapping has been used in

the patients with Alzheimer's disease (Borthakur et al., 2008; Haris et al., 2009a; Haris et al., 2011a; Haris et al., 2011b); the T1rho values of hippocampus and medial temporal lobes in patients with Alzheimer's disease are significantly lower than those of healthy volunteers.

1.2.6 T1rho Dispersion and Application

T1rho dispersion is the dependence of T1rho relaxation time with spin-lock field strength, or spin-lock frequency. If frequency of spin-lock (FSL) approaches zero, the weak spin-lock field is unable to continue to lock individual spins from dephasing. Hence, the T1rho approaches T2 at low FSL. On the other hand, if the FSL increases, T1rho begins to approach T1, although in practical applications in biological tissue this limit is never encountered due to the large spin-lock frequency needed to achieve.

T1rho dispersion imaging usually involves T1rho mapping for at least two spin-lock frequencies. Because T1rho is sensitive to the low-frequency motional processes around or at spin-lock frequency, T1rho dispersion imaging becomes a powerful tool to study the low frequency spin-lattice interaction in biological tissues and provides useful information like proton exchange between water and macromolecules. T1rho dispersion has been shown to be sensitive to conditions which affect proton exchange such as pH (Makela et al., 2001) and ^{17}O concentration

(Charagundla et al., 1998; McCommis et al., 2010; Tailor et al., 2004; Tailor et al., 2003).

1.3 Thesis Overview

T1rho MR imaging provides us a viable approach to study low-frequency motional processes in biological tissues; it could provide useful information on composition of macromolecules such as protein, proton exchange between water and macromolecules and so on, that is not feasible by using T1 and T2 imaging.

This thesis is divided into six Chapters. The purpose of this introductory Chapter is to provide background on the T1rho magnetic resonance imaging, briefly explain the basic theoretical aspects of T1rho MRI and application of T1rho MRI.

In Chapter 2, we studied the whether and how normal brain aging and chronic spontaneous hypertensive is associated with brain T1rho value changes. The T1rho values in rat brain of Sprague-Dawley (SD) rats from 5-month to 15-month, and spontaneous hypertensive rats (SHR) with Wistar Kyoto (WKY) rats from 6-month to 12-month, were longitudinally measured. The experimental results showed that the T1rho value in three brain regions of thalamus, hippocampus, and cortices increased with aging process, and the T1rho value was significantly higher in hypertensive rats (SHR) than normotensive rats (WKY).

In Chapter 3, fifty-two human subjects were recruited for a clinical study to study

the whether and how T1rho value specifically offer better evaluation of disc degeneration compared with T2 value. The T1rho and T2 values for nucleus pulposus and annulus fibrosis of discs were evaluated using five-level and eight-level semi-quantitative disc degeneration grading systems. The results showed that both T1rho and T2 values decreased in a similar pattern following disc degeneration for nucleus pulposus; T1rho value decreased progressively faster than T2 value for annulus fibrosis; both T2 and T1rho values of nucleus pulposus and annulus fibrosis did not reduce further by disc-space narrowing. Therefore, T1rho value is better suited for evaluating AF in degenerated disc than T2 value. The eight-level grading system will still be useful for clinical evaluation, particularly for those with severe disc degeneration and disc space narrowing.

Recently it was shown that T1rho value increased with the severity of liver fibrosis in rats with bile duct ligation. In Chapter 4, a rat carbon tetrachloride (CCl4) liver injury model was used for further investigating the merit of T1rho MRI for liver fibrosis evaluation. Male Sprague-Dawley rats received intraperitoneal injection of 2 ml/kg CCl4 twice weekly for up to 6 weeks. Then CCl4 was withdrawn and the animals were allowed to recover. Liver T1rho MRI and conventional T2-weighted images were acquired. Animals underwent MRI at baseline and at 2 days, 2 weeks, 4 weeks and 6 weeks post CCl4 injection, and they were also examined at 1 week and 4

weeks post CCl4 withdrawal. Liver histology was also sampled at these time points. The results showed rat liver T1rho values increased slightly, though significantly, on day 2, and then increased further and were highest at week 6 post CCl4 insults. The relative liver signal intensity change on T2-weighted images followed a different time course compared with that of T1rho. Liver T1rho values decreased upon the withdrawal of the CCl4 insult. Histology confirmed the animals had typical CCl4 liver injury and fibrosis progression and regression processes. Therefore, T1rho MRI can monitor CCl4-induced liver injury and fibrosis; liver T1rho was only mildly affected by edema and acute inflammation; liver MR T1rho decreased when liver fibrosis and injury regressed.

In Chapter 5, in order to translate liver T1rho MRI to a clinically applicable imaging biomarker, 20 healthy human subjects were recruited in this clinical study to explore the feasibility of T1rho MRI for human liver, and get the normal liver T1rho values range for healthy subjects at 3 T. It was found that it is feasible to obtain consistent liver T1rho measurement for healthy human liver with six spin-lock time (SLT) points of 1, 10, 20, 30, 40, and 50ms. When a 3T scanner and a spin-lock frequency was 500 Hz and six SLT points was used, the mean liver T1rho value of the healthy subjects was 42.5 ms, with a range of 38.8-46.5ms. The feasibility of using three (1, 20, and 50ms) or two (1, and 50ms) SLT points to measure liver T1rho value

was further explored. With the 38 examinations, the ICC for 6-SLT vs. 3-SLT T1rho measurements was 0.949, while the ICC for 6-SLT vs. 2-SLT T1rho measurement was 0.625. The scan-rescan reproducibility ICC was 0.811, 0.804 and 0.69 for 6-SLT, 3-SLT and 2-SLT measurement, respectively. Therefore, adopting 3-SLTs of 1, 20, and 50ms can be an acceptable alternative for the liver T1rho measurement, while 2-SLT of 1 and 50ms do not provide reliable measurement.

In Chapter 6, extensions of the T1rho MRI for future studies would be discussed.

CHAPTER 2 T1RHO MRI IN BRAIN AGING OF ANIMAL MODEL

2.1 Introduction

For neuroimaging, though limited, promising studies on brain T1rho MR imaging have been reported, including T1rho dispersion in the health human brain (Borthakur et al., 2004), T1rho MRI in the patients with Alzheimer's disease (Borthakur et al., 2008; Haris et al., 2009a; Haris et al., 2011a; Haris et al., 2011b), the patients with Parkinson's disease with and without dementia (Haris et al., 2011a; Nestrasil et al., 2010a), as well as, the animal model of Alzheimer's disease (Borthakur et al., 2004) and cerebral ischemia (Jokivarsi et al., 2010). These studies suggest neuro-degenerative lesions are potentially associated with the change of the T1rho relaxation time.

Aging and hypertension are the common risk factors for neurodegenerative disease. However, whether normal aging process and chronic hypertension are associated with brain T1rho relaxation change remains unknown. With aging process, decrease of cerebral blood flow (Heiland et al., 2002; Lee et al., 2011), dysfunction of blood brain barrier (Knox et al., 1980; Tomassoni et al., 2010), occurrence of brain atrophy (Amenta et al., 2010), and loss of nerve cells (Napoleone et al., 1990; Tomassoni et

al., 2010) commonly exhibited in the brain of aged rats. Spontaneously hypertension rats (SHR) are normotensive at birth and gradually develop severe hypertension in the first 2-4 months of life. At 6 months they develop a sustained hypertension compared to their normotensive control strain, the Wistar Kyoto (WKY) rats. The hypertensive rats exhibit these similar changes with aging rats (Amenta et al., 2010; Knox et al., 1980; Lee et al., 2011; Napoleone et al., 1990; Tomassoni et al., 2010), but they can be more advanced than the age-matched normative rats.

Therefore, the purpose of study described in this Chapter is to observe the T1rho values in rat brain associated with normal aging process and chronic hypertension. We longitudinally investigated the T1rho values changes in the Sprague–Dawley (SD) rats, Wistar–Kyoto (WKY) rats and Spontaneously Hypertensive rats (SHR).

2.2 Materials and Methods

2.2.1 Animal Model of Brain Aging

With the animal ethics approval, 18 male Sprague-Dawley (SD) rats, 11 male Wistar-Kyoto (WKY) rats, and 11 male Spontaneously Hypertensive rats (SHR) were included in our study. The SD rats were scanned longitudinally at the age of 5-month, 8-month, 10-month and 15-month. The SHR and the age matched-WKY rats were

scanned longitudinally at the age of 6-month, 9-month, and 12-month. The animals were housed in cages (3 or 4 rats per cage) on a 12-h light/12-h dark cycle in an air-conditioned room at 25°C. Food and water were available ad libitum.

2.2.2 T1rho Data Acquisition

MRI was performed on a 3 T clinical scanner (Achieva, Philips Healthcare, Best, The Netherlands). The Ketamine/Xylazine combination anesthetic was used for MR scanning; the dose of Ketamine/Xylazine for rat in this study was 100 mg/kg and 10 mg/kg body weight. After anesthesia, animals were positioned prone and a custom made quadrature volume RF coil of 7cm internal diameter was used as signal transmitter and receiver. 14-16 axial slices were used to cover the whole rat brain. The diagram of sequence for T1rho MRI is given in Figure 2.1 and Figure 2.2. For T1rho measurement, a rotary echo spin-lock pulse was implemented in a 3D fast field echo (FFE) sequence. Spin-lock frequency was set as 500 Hz, TE and TR were 3.6ms and 7.4ms respectively. The voxel size was $0.3\times0.35\times1.50$ mm^3. The flip angle was 40 degree. The TI (delay time) after T1rho acquisition was set as 5500ms to restore equilibrium magnetization prior to the next T1rho preparation.

T1rho MR scanning schedule for SD rats, WKY rats and SHR is given in Figure 2.3. The images of SD rats were acquired at three spin-lock time points (SLT) of 1ms,

20ms, and 50ms (Figure 2.3). The MR images of SHR and WKY rats were acquired at four spin-lock times (SLT) of 1ms, 20ms, 50ms and 80ms (Figure 2.3). The number of signal average (NSA) was 3 for SD rats and 4 for SHR and WKY rats. For the SD rat, an inversion TFE prepulse (inversion time: 1700ms) was used to remove the contribution from cerebrospinal fluid (CSF) to T1rho maps; and was not used in SHR and WKY rats (Figure 2.2).

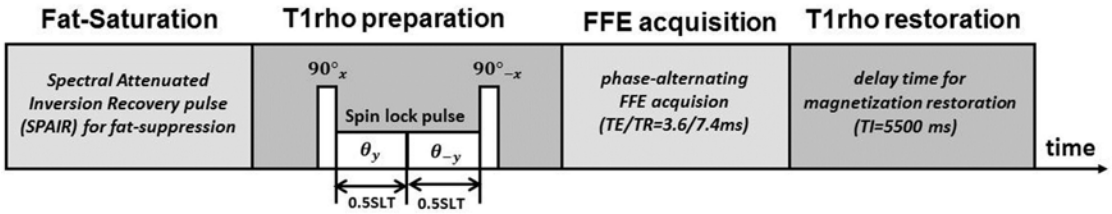

Figure 2.1: Diagram of the sequence, which is the spin-lock fast field echo (FFE) imaging sequence for T1rho MRI, the rotary echo spin-lock pulse cluster is used for T1rho preparation. SLT= spin-lock time.

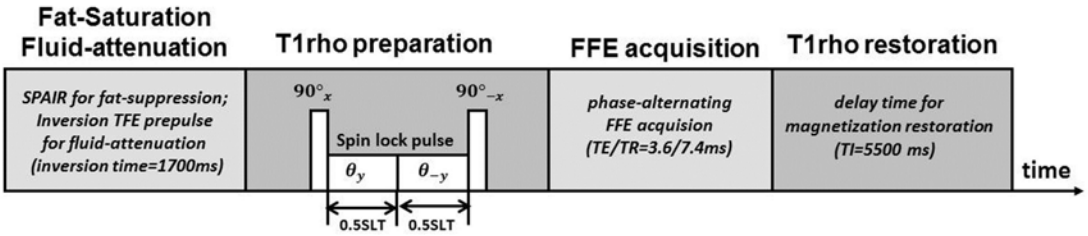

Figure 2.2: Diagram of the sequence, which is the spin-lock fast field echo (FFE) imaging sequence for T1rho MRI, the rotary echo spin-lock pulse cluster is used for T1rho preparation. The inversion TFE prepulse (inversion time=1700ms) is inserted before the T1rho preparation pulse for fluid attenuation. SLT= spin-lock time.

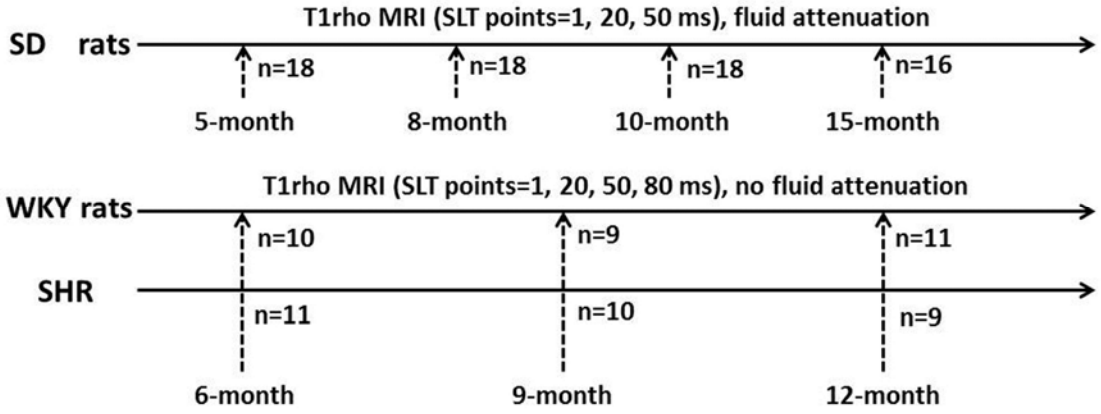

Figure 2.3: T1rho MR scanning schedule for SD rats, WKY rats and SHR. For the SD rats, fluid attenuation was used in order to remove the contribution from CSF to T1rho maps. SLT= spin-lock time.

2.2.3 T1rho Data Processing

T1rho maps were computed on a pixel-by-pixel basis by using a mono-exponential decay model with a homemade Matlab program (Mathworks, Natick, MA):

$$\mathrm{M(SLT)} = M_0 \cdot exp^{(-SLT/T1rho)} \quad \text{Equation [1.4]}$$

Where M0 and M(SLT) denote the equilibrium magnetization and T1rho-prepared magnetization with the spin-lock time of SLT, respectively. This mono-exponential equation was linearized by logarithm and T1rho maps were generated by fitting all pixel intensity data as a function of SLT using linear regression. T1rho was calculated as -1/slope of the straight-line fit. The T1rho-weighted images acquired at different spin-lock time points and T1rho map for a typical SD rat is shown in Figure 2.4. The

T1rho-weighted images acquired at different spin-lock time points and T1rho map for a typical hypertensive rat (SHR) is shown in Figure 2.5.

2.2.4 T1rho Measurement and Statistical Analysis

These measurements were performed in the thalamus, hippocampus, and cortices region of the brain that is primarily associated with neuro-degenerative disease (Hughes et al., 2012; Yankner et al., 2008). T1rho values were measured in user-defined regions of interest (ROIs) in the bilateral thalamus (T), hippocampus (H), and frontal cortices (C) from T1rho map of rat brains (Fig 4, Fig 5), according the standard rat brain atls (right lower) by Paxinos, G. and Watson, C. (2005). Note that the MRI image does not exactly match with the atlas image because they have different slice thickness (1.5 mm for the MRI image and 0.12 mm for the atlas image).

We performed statistical tests showing that there were no significant differences in T1rho values when comparing the two hemispheres. Therefore, we pooled the data of the corresponding regions of both hemispheres. Data are presented as mean ± standard deviation. All statistical analyses were done using SPSS 14.0 (SPSS, Chicago, IL). The Mann-Whitney U test was used for non-paired comparison. The one way analysis of variance (ANOVA) test was performed with linear trend study of variable “T1rho values” with age process.

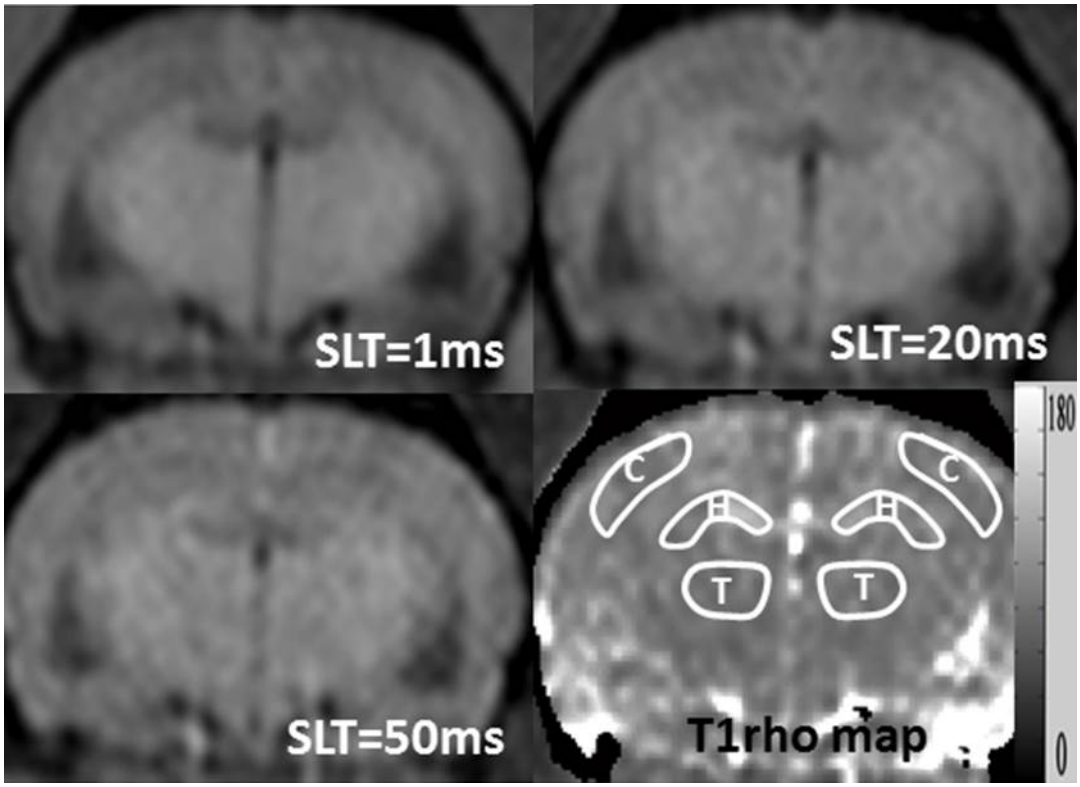

Figure 2.4: T1rho-weighted images of a SD rat with spin-lock time points of 1ms, 20ms, and 50ms. The bilateral thalamus (T), hippocampus (H), and cortices (C) were manually defined in the T1rho map according the standard rat brain atls by Paxinos, G. and Watson, C. (2005) (see Figure 2.5). SLT= spin-lock time.

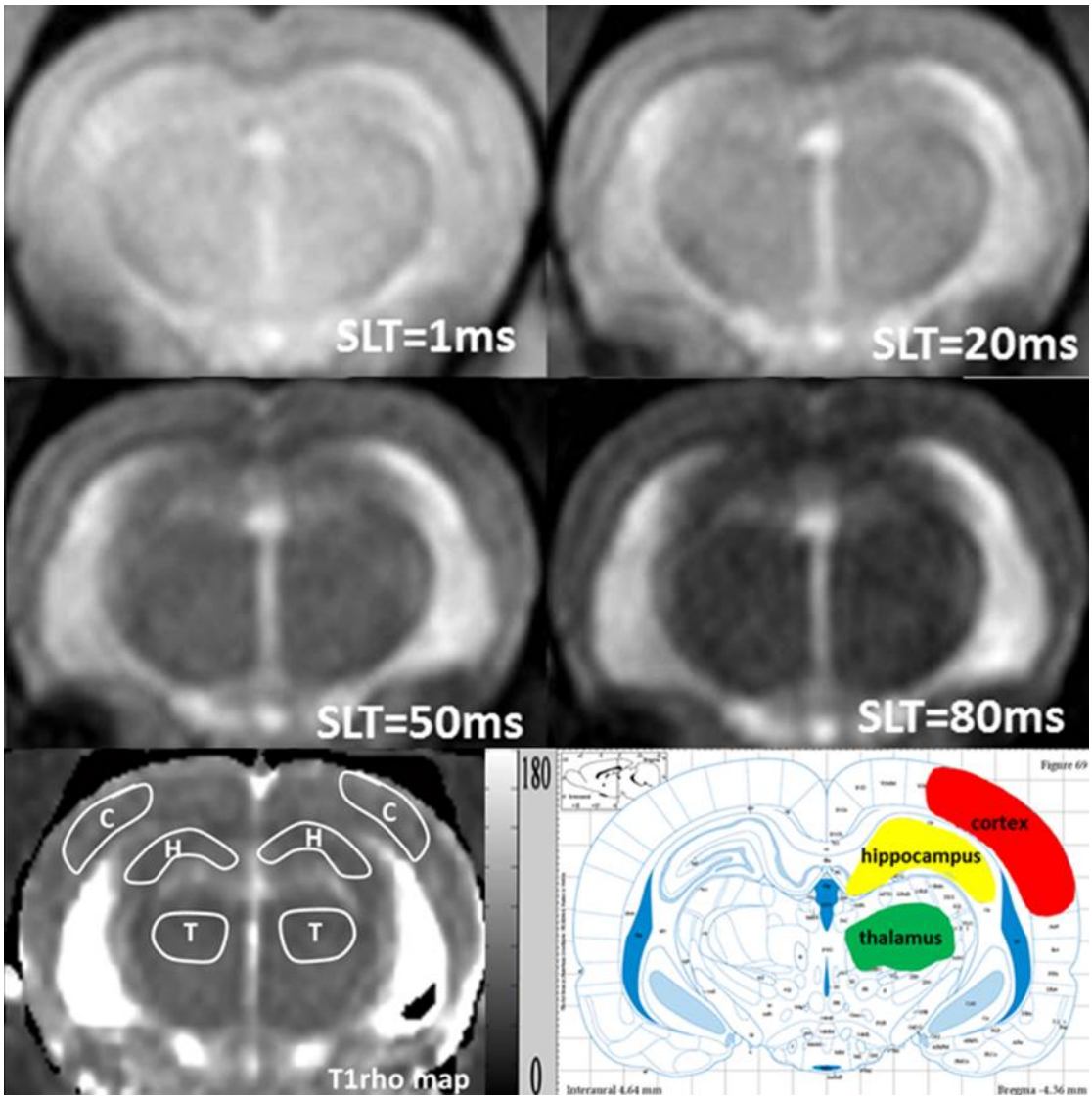

Figure 2.5: T1rho-weighted images of a SHR with spin-lock time points of 1ms, 20ms, 50ms, and 80ms (upper and middle row). The bilateral thalamus (T), hippocampus (H), and cortices (C) were manually defined in the T1rho map (left lower) according the standard rat brain atls (right lower) by Paxinos, G. and Watson, C. (2005). Note that the MRI image does not exactly match with the atlas image because they have different slice thickness (1.5 mm for the MRI image and 0.12 mm for the atlas image). SLT= spin-lock time.

2.3 Results

Two SD rats died at age of 14-month, so there were only 16 SD rats' image data at age of 14-month. The images of a WKY rat at age of 6-month, 2 WKY rats at age of 9-month, a SHR at age of 9-month and 2 SHR at age of 12-month were not included in this study due to imaging artifact. The T1rho measurement data (mean±SD) for SD rats, WKY rats, and SHR were summarized in the Table 2.1 and Table 2.2.

For the SD rats (Figure 2.6, Figure 2.7, Figure 2.8,), at age of month 8, T1rho values in the thalamus, hippocampus and cortices increased on average by 5.1% ($p<0.05$), 9.7% ($p<0.05$) and 5.2% ($p<0.05$) compared with the values at month 5. At month 10, T1rho values in the thalamus, hippocampus and cortices increased on average by 5.8% ($p<0.05$), 5.7% ($p<0.05$) and 6.4% ($p<0.05$) respectively compared with the value at month 8. At month 15, T1rho values in the thalamus, hippocampus and cortices increased on average by 7.5% ($p<0.05$), 5.7% ($p<0.05$) and 6.6% ($p<0.05$) compared with the value at month 10, as well as increased by 19.5%, 22.4% and 19.4% compared with the value at month 5. In addition, the one-way analysis of variance (ANOVA) test for linear trend showed that T1rho values in thalamus, hippocampus and cortices had a significant linear trend for increasing during the aging process from 5-month to 15-month ($p<0.05$, Table 2.1, Figure 2.9).

For the WKY rats and SHR, the T1rho values in thalamus, hippocampus and

cortices also had a significant linear trend for increasing during the aging process from 6-month to 12-month ($p<0.05$, Table 2.2, Figure 2.10, Figure 2.11). At the age of 12-month, T1rho values in thalamus, hippocampus and cortices of WKY rats increased on average by 20.0% ($p<0.05$), 9.5% ($p<0.05$), and 8.5% ($p<0.05$) compared with the values at month 6. Similarly, at the age of 12-month, T1rho values in thalamus, hippocampus and cortices of SHR increased on average by 14.7% ($p<0.05$), 8.7% ($p<0.05$), and 7.5% ($p<0.05$) compared with the values at month 6.

Furthermore, T1rho values in thalamus, hippocampus and cortices of SHR were consistently higher than those of WKY control rats at the age of 6-month, 9-month and 12-month. At the age of 6-month, T1rho values in thalamus, hippocampus and cortices of SHR were 12.6% ($p<0.05$), 7.7% ($p<0.05$), and 8.9% ($p<0.05$) higher than WKY rats (Table 2.2, Figure 2.12, Figure 2.13, Figure 2.14). At the age of 9-month, T1rho values in thalamus, hippocampus and cortices of SHR were 4.7% ($p<0.05$), 4.7% ($p<0.05$), and 5.2% ($p<0.05$) higher than WKY rats (Table 2.2, Figure 2.12, Figure 2.13, Figure 2.14). At the age of 12-month, T1rho values in thalamus, hippocampus and cortices of SHR were 7.0% ($p<0.05$), 7.0% ($p<0.05$), and 7.9% ($p<0.05$) higher than WKY rats (Table 2.2, Figure 2.12, Figure 2.13, Figure 2.14). Meanwhile, the percentage regional T1rho values difference between SHR and WKY rats did not increase with aging process (Table 2.2).

Table 2.1: T1rho values (mean±SD) in the thalamus, hippocampus, and cortices of SD rats at age of 5, 8, 10 and 15 months.

	5 months	8 months	10 months	15 months
thalamus (ms)	67.2±2.4	70.6±3.1 [a]	74.7±4.0 [b]	80.3±3.9 [c,d]
hippocampus(ms)	73.2±2.3	80.3±3.0 [a]	84.9±3.7 [b]	89.7±3.7 [c,d]
cortices (ms)	71.6±1.9	75.3±3.1 [a]	80.1±3.6 [b]	85.4±4.1 [c,d]

Note: [a]: p<0.05 vs. 5-month old SD rats; [b]: p<0.05 vs. 8-month old SD rats; [c]: p<0.05 vs. 10-month old SD rats; [d]: p<0.05 for linear trend effect during the aging process from 5-month to 15-month.

Table 2.2: T1rho values (mean±SD) in the thalamus, hippocampus, and cortices of WKY rats and SHR at age of 6, 9, and 12 months.

	6 months			9 months			12 months		
	WKY	**SHR**	**Diff%**	**WKY**	**SHR**	**Diff%**	**WKY**	**SHR**	**Diff%**
T (ms)	60.1±1.5	67.6±1.7[a]	12.6%	65.1±1.7	68.2±1.1[a]	4.7%	72.0±4.3[b]	77.1±3.8[a,b]	7.0%
H (ms)	68.6±2.4	73.9±2.1[a]	7.7%	73.6±3.0	77.1±2.7[a]	4.7%	75.1±2.6[b]	80.3±2.1[a,b]	7.0%
C(ms)	75.6±2.9	82.3±2.8[a]	8.9%	79.9±3.6	84.1±2.5[a]	5.2%	82.0±2.0[b]	88.5±4.4[a,b]	7.9%

Note: T: thalamus; H: hippocampus; C: cortices; Diff%= (measurement of SHR - measurement of WKY) / measurement of WKY. [a]: p<0.05 vs. age-matched WKY rats. [b]: p<0.05 for linear trend effect during the aging process from 6-month to 12-month.

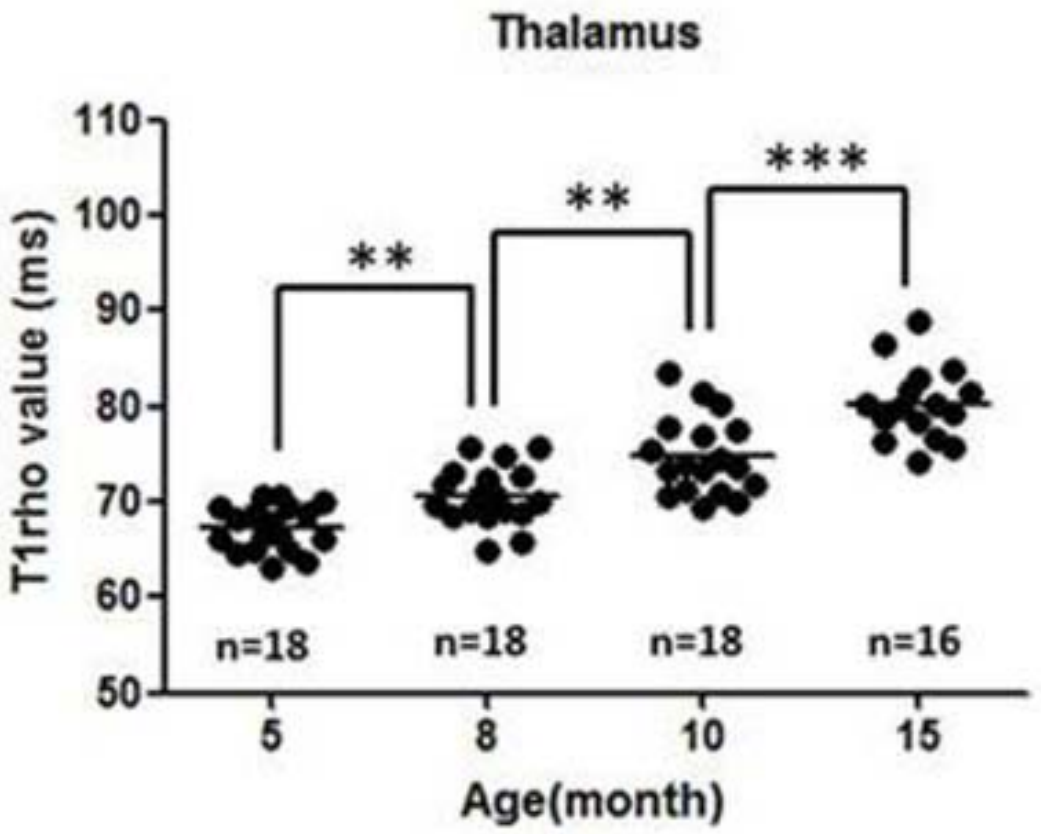

*Figure 2.6: T1rho values in the thalamus of SD rats at the age of 5, 8, 10, and 15 months. ***: $p<0.001$, **: $p<0.01$.*

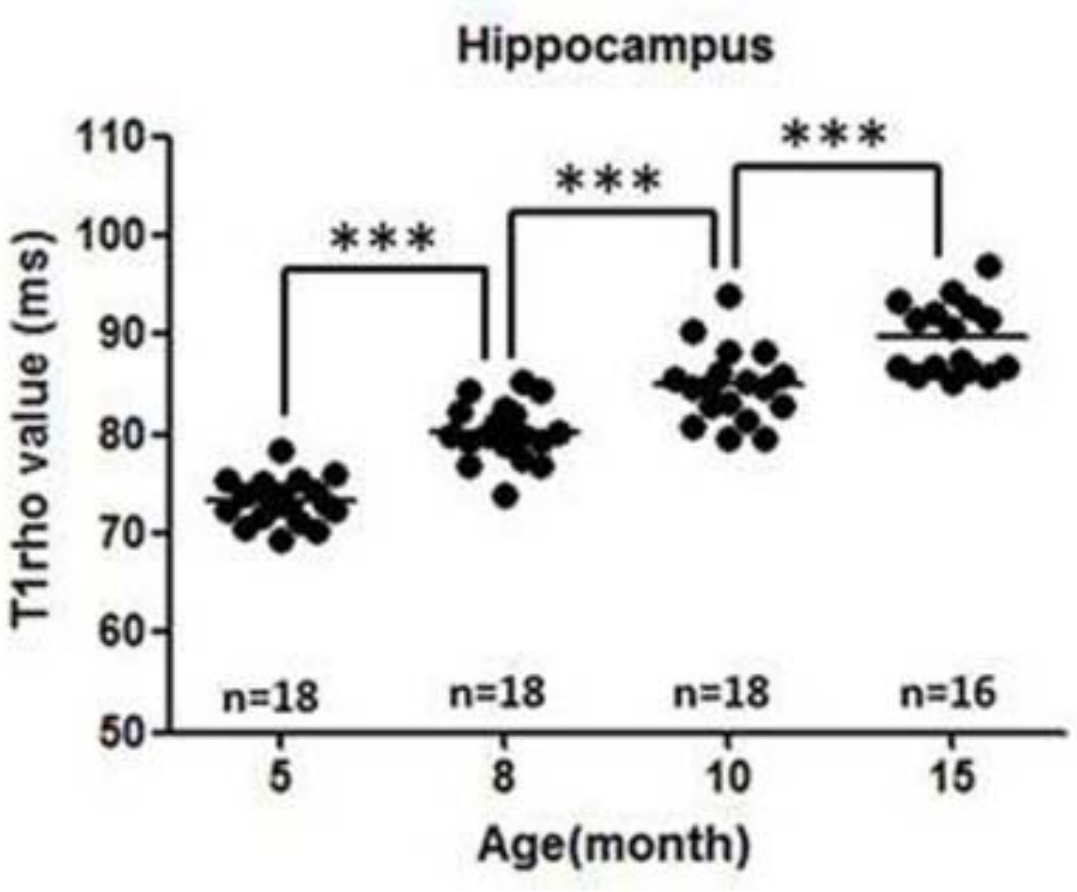

*Figure 2.7: T1rho values in the hippocampus of SD rats at the age of 5, 8, 10, and 15 months. ***:p<0.001.*

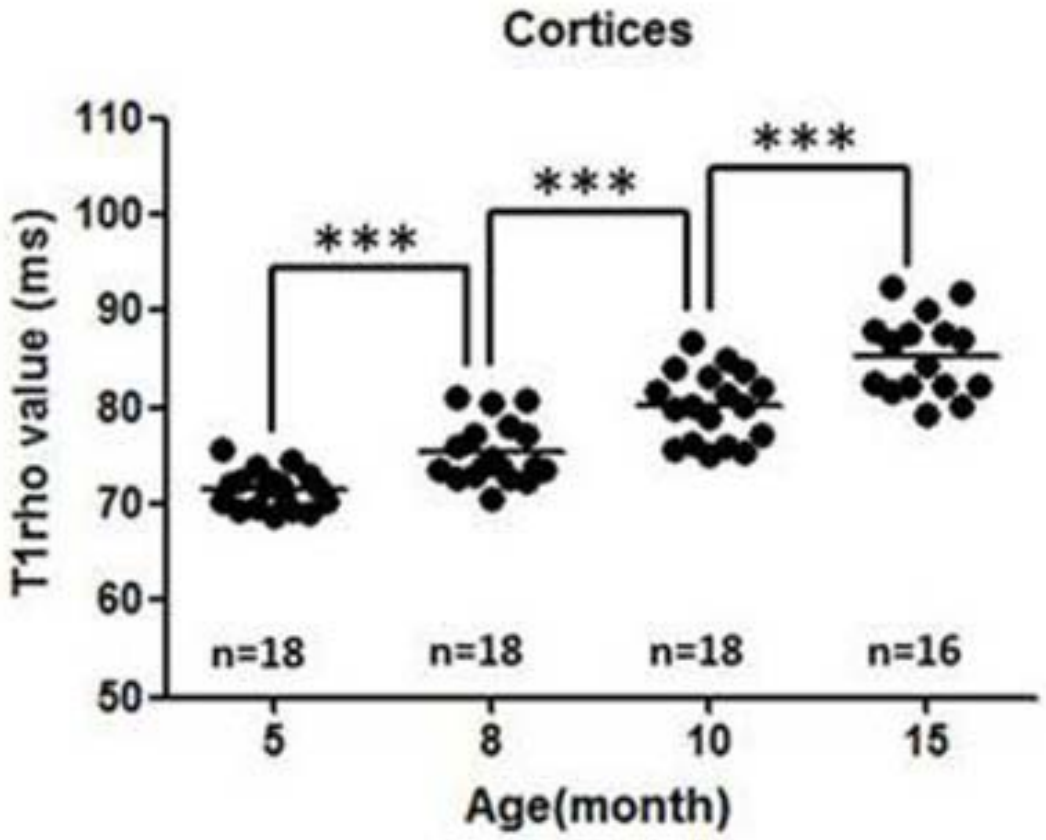

*Figure 2.8: T1rho values in the cortices of SD rats at the age of 5, 8, 10, and 15 months. ***:p<0.001.*

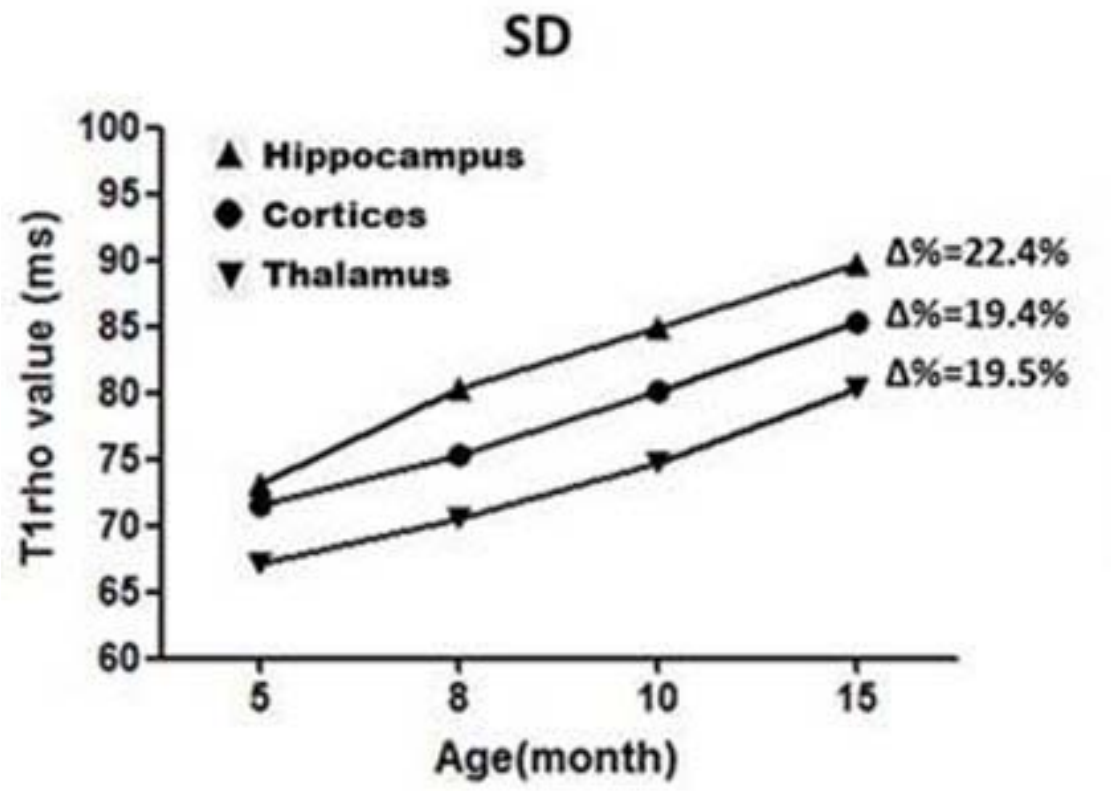

Figure 2.9: The mean plots of T1rho values for SD rats at the different age. Δ%=(measurement data at 15-momth - measurement data at 5-month)/ measurement data at 5-month.

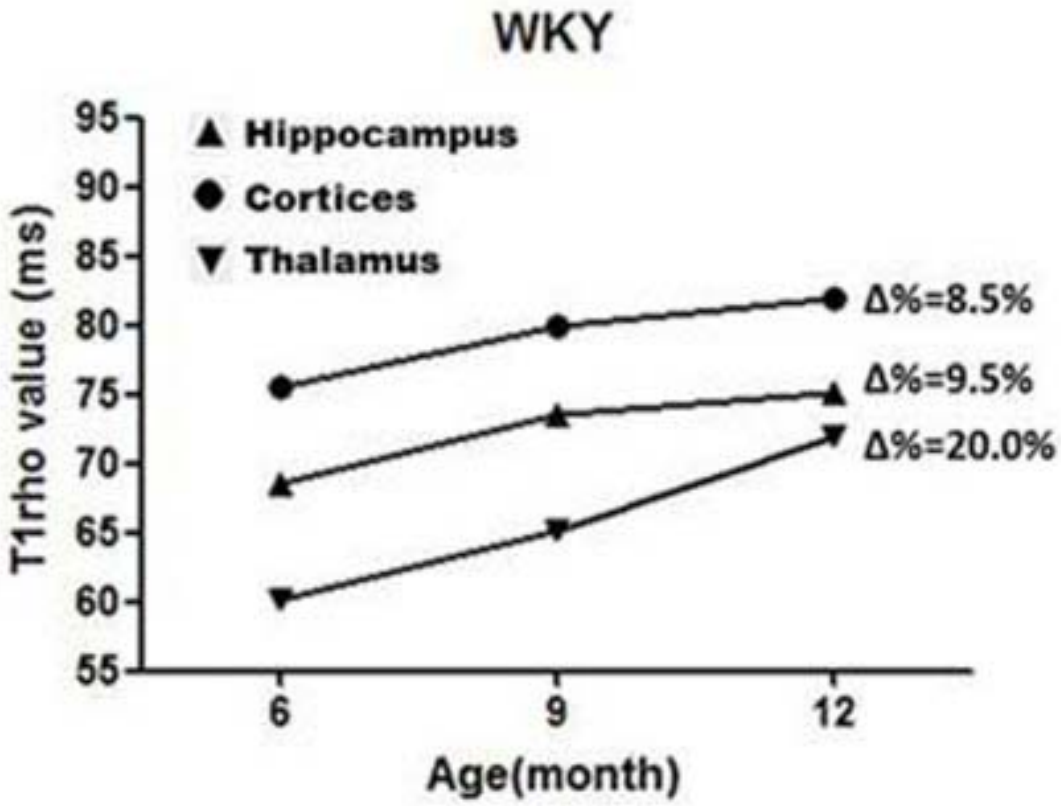

Figure 2.10: The mean plots of T1rho values for WKY rats at the different age. Δ%=(measurement data at 12-momth - measurement data at 6-month)/ measurement data at 6-month.

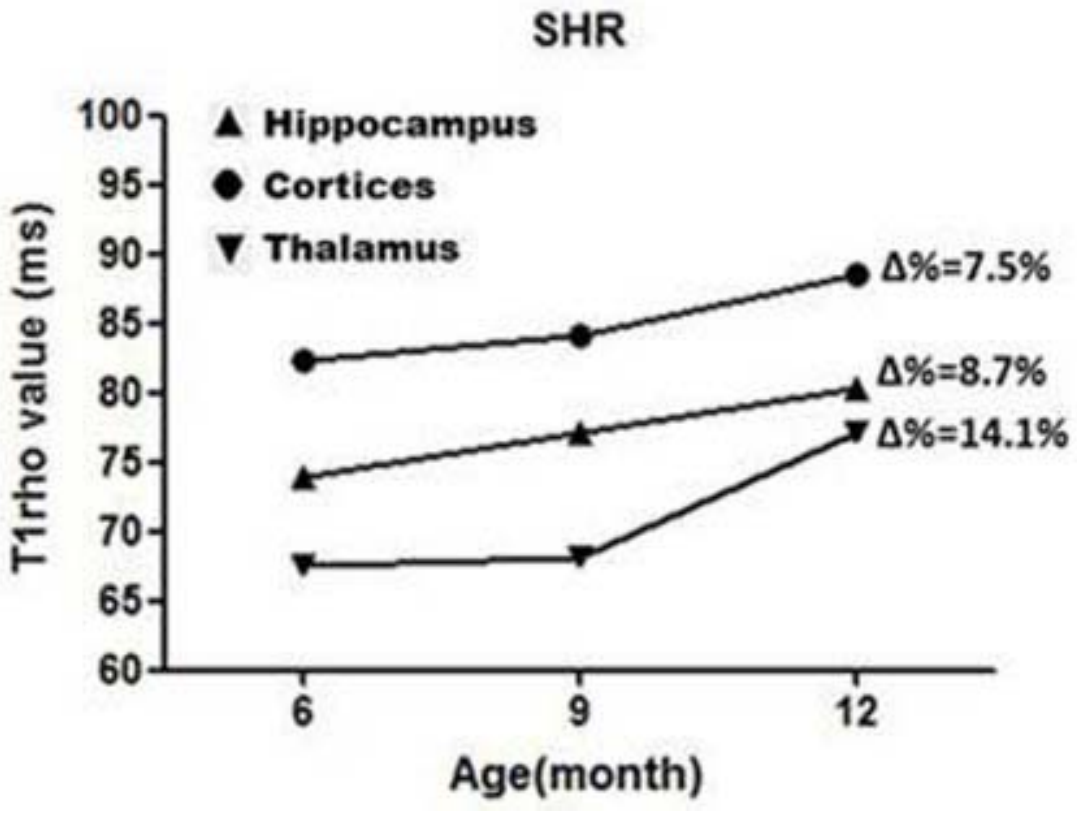

Figure 2.11: The mean plots of T1rho values for SHR at the different age. Δ%=(measurement data at 12-momth - measurement data at 6-month)/ measurement data at 6-month.

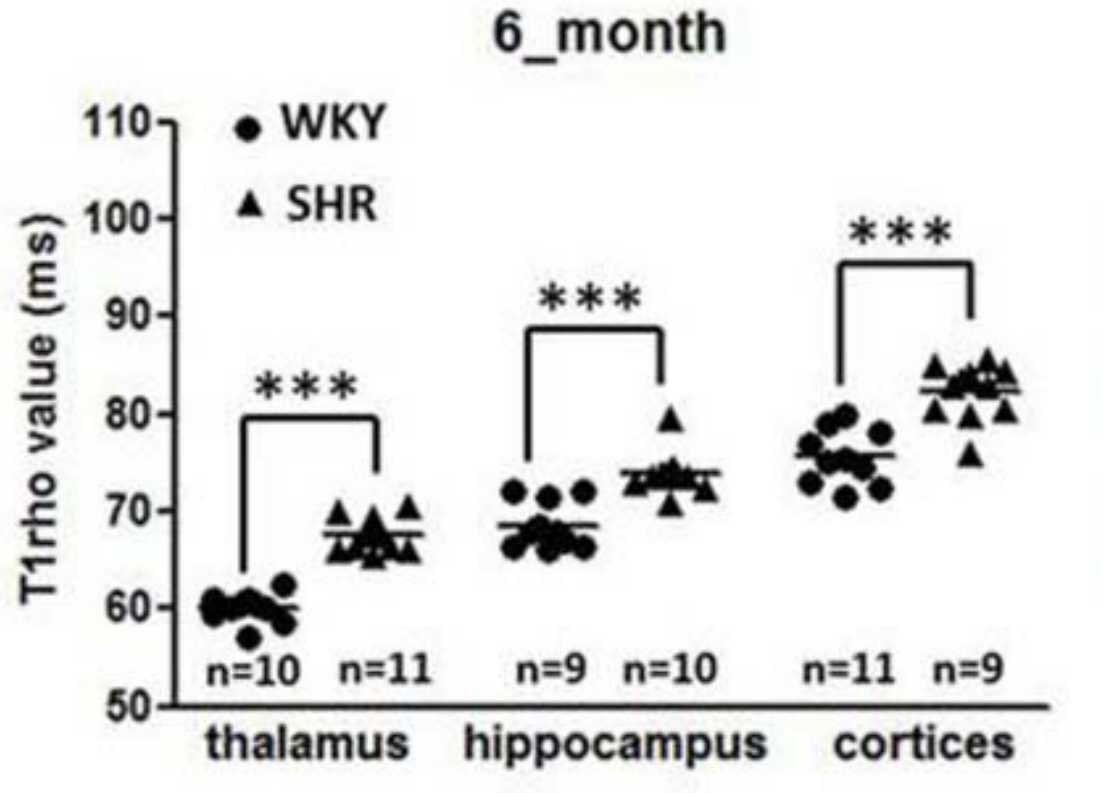

*Figure 2.12: T1rho values in the thalamus, hippocampus, and cortices of WKY and SHR at the age of 6-month. ***: p<0.001.*

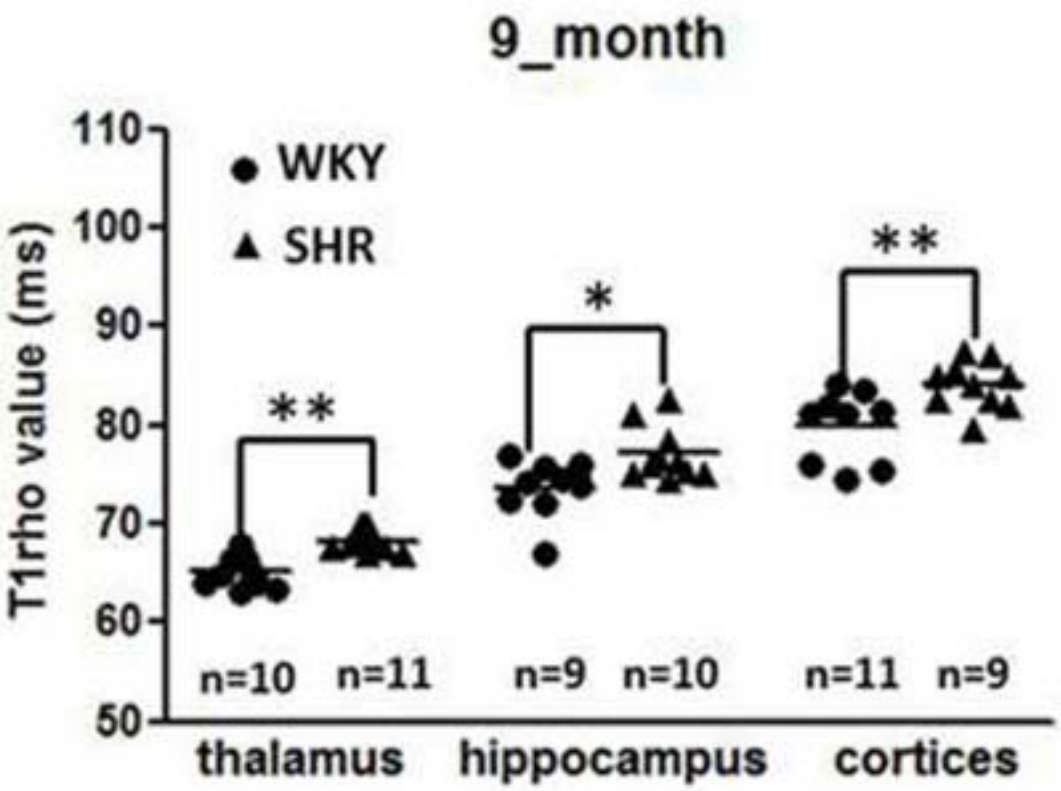

*Figure 2.13: T1rho values in the thalamus, hippocampus, and cortices of WKY and SHR at the age of 9-month. **: $p<0.01$,*: $p<0.05$.*

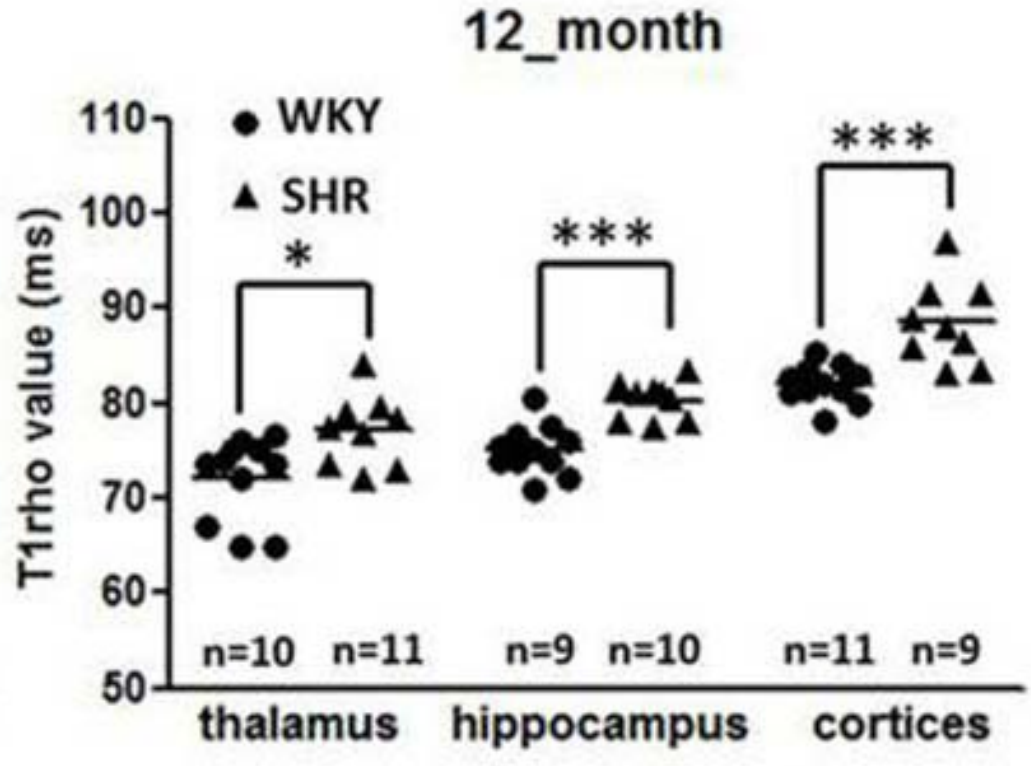

*Figure 2.14: T1rho values in the thalamus, hippocampus, and cortices of WKY and SHR at the age of 12-month. ***: $p<0.001$, *: $p<0.05$.*

2.4 Discussion

Discovering the association between age/hypertension-related changes and T1rho relaxation may help us better realize the T1rho relaxation for neurodegenerative disease. In the current study, we found significantly increased T1rho relaxation in the rat brain during the normal age processing period; this phenomenon was current in rats without hypertension (SD, WKY rats) and rats with hypertension (SHR). Furthermore, we found significantly higher T1rho relaxation in the hypertensive rat (SHR) brain than the normotensive rat (WKY) brain in all three time points of

6-month, 9-month, and 12-month.

The feasibility of T1rho relaxation in measuring plaques burden in the mice model of Alzheimer's disease (AD) has been reported by Borthakur and colleagues (Borthakur et al., 2006). Then they have shown increased T1rho relaxation in medial temporal lobe (MTL) of Alzheimer's disease (AD) patients compared to controls (Borthakur et al., 2008). Furthermore, Haris and colleagues showed the significantly increased T1rho relaxation in the hippocampus of mild cognitive impairment (MCI) and Alzheimer's disease (AD) patients compared to controls (Haris et al., 2009a); the significantly increased T1rho relaxation in the hippocampus of Alzheimer's disease (AD) and Parkinson's disease with dementia (PDD) patients compared to controls and Parkinson's disease (PD) (Haris et al., 2011a); the significantly increased T1rho relaxation in the medial temporal lobe (MTL) of Alzheimer's disease (AD) patients compared to controls (Haris et al., 2011b). All these studies suggested that the presence of Alzheimer's disease (AD) pathology may contribute to the increased T1rho relaxation.

Amyloid plaques also can appear in the cortex and hippocampus, neurofibrillary tangles can predominately locate in the entorhinal cortex of normal aging individuals, and generally more widespread in Alzheimer's disease (AD) patients (Haris et al., 2011b). Therefore, the gradually deposit of amyloid plaques and neurofibrillary

tangles in brain with normal aging process might contribute to the increase of T1rho values in rat brain.

Brain atrophy, which is assumed to reflect underlying neuronal loss of brain, has been reported might be associated with increased T1rho values in hippocampus and medial temporal lobe (MTL) of Alzheimer's disease (AD). Occurrence of brain atrophy and loss of nerve cells in whole brain are commonly exhibited in aged rats; therefore the brain atrophy and loss of nerve cells might also contribute to the increase of T1rho values of brain with normal age process.

Hypertension is a prevalent comorbid medical condition of aging, and may also predispose to neurodegenerative disorders (Yankner et al., 2008). Spontaneously hypertensive rats (SHR), which are normotensive at birth and develop sustained hypertension between 3 and 6 months of age, can represent a reasonable model of hypertensive-related brain damage (Amenta et al., 2010).

In our current study, spontaneously hypertensive rats (SHR) and WKY rats were underwent T1rho MR imaging comparatively; the T1rho values in SHR brain were significantly higher than these of WKY rats in all three different time points. The hypertensive rats exhibit similar brain changes with aging rats, such as the occurrence of brain atrophy and loss of nerve cells (Amenta et al., 2010; Bendel and Eilam, 1992; Knox et al., 1980; Tomassoni et al., 2010), but they can be more advanced than the

age-matched normative rats. Therefore, the higher degree of brain atrophy and loss of nerve cells might contribute to the higher T1rho values in SHR brain than these of WKY rats.

However, aging and hypertension have not been well understood at a molecular level. The age-related and hypertension-related changes are complicated in brain. There should be some other age-related changes and hypertension-related changes in brain might co-contribute to the increase of T1rho values in brain with aging process and hypertension.

In our study, the T1rho measurement in thalamus was the lowest in brain of SD, SHR and WKY rats. For SD rats group, the T1rho value of hippocampus was higher than that of cortex. For SHR and WKY rats group, the T1rho value of hippocampus was lower than that of cortex. It might because of different scanning parameters were used for them. For SD rats group, they were underwent T1rho MR imaging with an inversion TFE prepulse inserted before T1rho pulse in order to remove the contribution from CSF to the T1rho maps. For SHR and WKY rats, no inversion TFE prepulse was inserted before T1rho pulse. In addition, three spin-lock times (SLT=1, 20, 50ms) and NSA=3 were used for SD rats; four spin-lock times (SLT=1, 20, 50, 80ms) and NSA=4 were used for SHR and WKY rats. Therefore, the SNR of SD rats T1rho images was slightly lower than that of SHR and WKY rats.

The findings from the current study are preliminary, given the limited sample sizes. Statistical power could be further increased with access to larger sample sizes in future studies. This study did not investigate the exact mechanism of T1rho increase in the normal aging and chronic hypertensive rat model. Histological correlation study may be help to further understand the mechanism underlying the rat brain T1rho increase.

2.5 Summary

In summary, T1rho values increased in rat brain might be associated with the age-related and hypertension-related changes of brain tissue composition. T1rho MR imaging might be a potential technique to monitor brain changes due to age process and chronic hypertension. The age-related changes in T1rho values shown in our study should also be taken into account in other kinds of longitudinal studies in rats using T1rho MRI, particularly with the aim of also distinguishing neurodegenerative changes in T1rho relaxation from normal aging processes.

CHAPTER 3 T1RHO MRI IN LUMBAR DISC DEGENERATION OF HUMAN SUBJECTS

3.1 Introduction

Intervertebral disc degeneration is a process that begins early in life and is the consequence of a variety of genetic, mechanical, traumatic and nutritional factors, as well as normal ageing (Adams and Roughley, 2006). Early signs of disc degeneration are manifested by biochemical changes, including a loss of proteoglycans, a loss of osmotic pressure and hydration (Adams and Roughley, 2006). In the later stages of disc degeneration, morphological changes occur, including a loss of disc height, disc herniation, annular tears and radial bulging (Modic and Ross, 2007).

Magnetic resonance imaging is commonly used for assessment of symptomatic disc degeneration. On T2-weighted MR images, disc degeneration is seen as a reduction in signal of the nucleus pulposus (NP) and inner fibres of the annulus. With more severe disc degeneration, disc height decreases. Pfirrmann et al. (Pfirrmann et al., 2001) devised a five-level grading system for disc degeneration based on MR signal intensity, disc structure, distinction between nucleus and annulus, and disc height. Recently, it has been suggested that Pfirrmann's five-level grading system does not show discriminatory power to assess severe disc degeneration, and an eight level

grading system has been proposed and successfully applied in a number of clinical studies (Griffith et al., 2007; Wang et al., 2011b; Wang et al., 2011c).

Noninvasive quantitative assessments for early degenerative changes are needed and will become more important because of emerging alternative treatments for earlier stages of disc degeneration (e.g. cell therapy, growth factor therapy) (Carl et al., 2004; Phillips et al., 2003; Vadala et al., 2007).

Five-level and eight-level grading systems provide semi-quantitative evaluation of disc degeneration, particularly for later stages of degeneration (Griffith et al., 2007; Pfirrmann et al., 2001). T2 and T1rho value reflect the intrinsic material properties of disc tissues, therefore the T2 and T1rho measurement are being widely explored (Auerbach et al., 2006; Blumenkrantz et al., 2006; Blumenkrantz et al., 2010; Chiu et al., 2001; Johannessen et al., 2006; Kerttula et al., 2001; Perry et al., 2006; Weidenbaum et al., 1992). These measurements are theoretically device-and reader-independent, and may have the potential to detect subtle differences in tissue composition that may not be apparent with T2-weighted image-based qualitative or semi-quantitative assessment; therefore they would likely be more useful for early disc changes.

T2 measurement has been reported to be sensitive to changes in collagen and water content in the intervertebral discs, and T2 value decreases with disc degeneration

(Chiu et al., 2001; Kerttula et al., 2001; Perry et al., 2006; Weidenbaum et al., 1992).

T1rho measurement, which probes the interaction between water molecules and their macromolecular environment, is suggested to have the potential to identify early biochemical changes in the intervertebral disc. In cadaveric human discs it was shown that in the nucleus pulposus (NP) T1rho value strongly correlates with proteoglycan content (Johannessen et al., 2006). In vivo studies have demonstrated differences in mean T1rho values between the nucleus and the annulus, and have shown a correlation between T1rho values and degenerative grades at 1.5T (Auerbach et al., 2006; Blumenkrantz et al., 2006). More recently, in an in-vivo study using 3.0T, Blumenkrantz et al. (Blumenkrantz et al., 2010) reported that the values of T1rho and T2 were significantly correlated. However, whether and how T1rho specifically offer better evaluation of disc degeneration compared with T2 remains unknown.

The purpose of study described in this Chapter is to determine the relative performance of T1rho value and T2 value in their assessment of disc degeneration with reference to the five-level and eight-level semi-quantitative disc degeneration grading systems.

3.2 Methods

3.2.1 Subjects

Fifty-two subjects were recruited: 12 subjects without low-back pain (nine men and three women; mean age 32.1 years, age range 23–42 years), and 40 subjects who had low-back pain (17 men and 23 women; mean age 54.1 years, age range 28–76 years). All subjects were confirmed to have no other spine diseases except disc degeneration. The study was approved by the local human research ethics committee. Written informed consent was obtained from all subjects.

3.2.2 MR Image Acquisition

To remove the potential confounding role of diurnal disc hydration changes, all subjects underwent imaging in the morning. MRI acquisition was performed on a 3.0T clinical system (Achieva, Philips Healthcare, Best, The Netherlands). A 12-channel receive-only spine coil was used as the signal receiver to cover the lumbar spine, and the built-in body coil was used as the signal transmitter.

3.2.2.1 T2-weighted MRI

The sagittal T2-weighted turbo spin echo (TSE) was included with the following parameters: FOV=200mm, voxel size =1.0×1.0×4.0mm^3, slice thickness=4 mm, TR=3302ms, TE=120ms. The number of signal averages (NSA) was one. A sensitivity-encoding (SENSE) factor of 2 was applied for parallel imaging to reduce the phase encoding steps. The scan time of conventional T2 weighted image was 4

minutes and 11 seconds.

3.2.2.2 T2 Mapping Imaging

A multi-echo turbo spin echo (TSE) pulse sequence was used for T2 mapping. Seven sagittal TSE images were acquired at identical locations as T1rho images. TSE imaging parameters included: FOV=200 mm, voxel size=1.0×1.0×4.0mm^3, slice thickness=4 mm, echo train length (ETL) =7, TEs=16, 32, 48, 64, 80, 96 and 112ms, TR=2300ms. The number of signal averages (NSA) was one. A sensitivity-encoding (SENSE) factor of 2 was applied for parallel imaging to reduce the phase encoding steps. The scan time of conventional T2 mapping imaging was 4 minutes and 34 seconds.

3.2.2.3 T1rho MRI

The diagram of sequence for T1rho MRI is given in Figure 3.1. The T1rho preparation pulse cluster was implemented in a 3D balanced fast field echo (b-FFE) sequence with centric phase-encoding acquisition for T1rho measurement. Spin-lock frequency was set as 500 Hz and the spin-lock times (SLTs) of 1ms, 10ms, 20ms, 40ms and 60ms were used for acquisition and T1rho mapping. Volume shimming was employed to minimize B_0 heterogeneity.

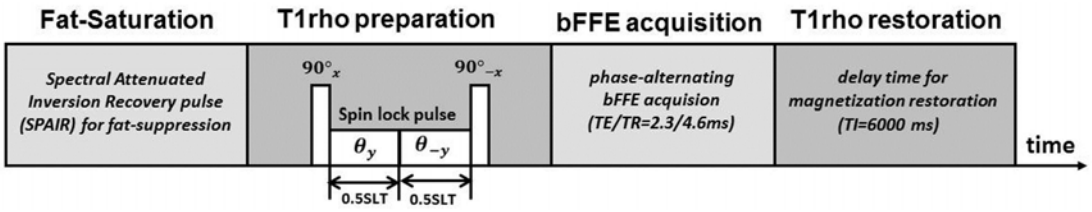

Figure 3.1: Diagram of the sequence for T1rho MRI, which is the spin-lock balanced fast field echo (b-FFE) imaging sequence for T1rho MRI, the rotary echo spin-lock pulse cluster is used for T1rho preparation. SLT= spin-lock time.

Segmented phase alternating b-FFE readout with centric phase encoding order was used for acquisition. T1rho-weighted images were acquired during the transient status towards the steady state but with T1rho weighted magnetization maintained (Li et al., 2008). A rotary echo spin-lock pulse was applied once for every segment length of 80 readouts. A delay time of 6,000ms was inserted after each segment acquisition to fully restore the equilibrium magnetization before the next T1rho preparation. TE and TR for b-FFE acquisition were 2.3ms and 4.6ms respectively. The field of view (FOV) was 200 mm and the voxel size was 1.0×1.0×4.0 mm^3. Seven sagittal slices were acquired and the slice thickness was 4 mm. The flip angle was 40° and the number of signal averages (NSA) was one. A sensitivity-encoding (SENSE) factor of 2 was applied for parallel imaging to reduce the phase encoding steps. The whole body specific absorption rate (SAR) was < 0.4W/kg for this sequence as demonstrated on the scanner's console. The scan time was 80 seconds per spin-lock time point.

3.2.3 Data Processing

Image analysis T2 and T1rho maps were computed on a pixel-by-pixel basis using a mono-exponential decay model with a homemade Matlab program (Mathworks, Natick, MA, USA):

$$M(TE) = M_0 \cdot \exp^{(-TE/T2)} \quad \text{Equation [3.1]}$$

$$M(SLT) = M_0 \cdot \exp^{(-SLT/T1rho)} \quad \text{Equation [1.4]}$$

Where M0 and M(TE) denote the equilibrium magnetization and magnetization acquired with the echo time TE, respectively. M(SLT) denotes the T1rho-prepared magnetization with the spin-lock time of SLT.

These two mono-exponential equations were linearized by logarithm. T1rho and T2 maps were generated by fitting each pixel's intensity as a function of SLT and TE using a non-negative least-square fitting algorithm, respectively. T1rho and T2 values were calculated as the inverse of the slope of the corresponding straight-line fit.

3.2.4 Data Measurement and Statistical Analysis

Five intervertebral discs (L1/L2–L5/S1) per subject were examined, with four discs excluded because of previous vertebral fusion operation, leading to 256 discs in total for analysis. As the purpose of this current study was to study the correlation of T1rho/T2 values with disc degeneration of a wide spectrum of grading, subjects with

or without low-back pain were analyzed together.

Images were analyzed in the mid-sagittal section of the lumbar spine. With T2-weighted images as reference, regions of interest (ROIs) were manually drawn over the T2 map and T1rho map of the discs by a Radiology trainee (ZF) with 3 years' experience reading MRI images. ROIs included nucleus pulposus (NP), anterior annulus fibrosus (AF) and posterior AF (Figure 3.2). Values of anterior AF and posterior AF were averaged as the value for AF. When an apparent tear was noted in the annulus, the abnormal signal areas were excluded in the ROIs. The ROI size for NP ranged 15−45mm^2, while the ROI size for AF (anterior + posterior) ranged from 8mm^2 to 45mm^2.

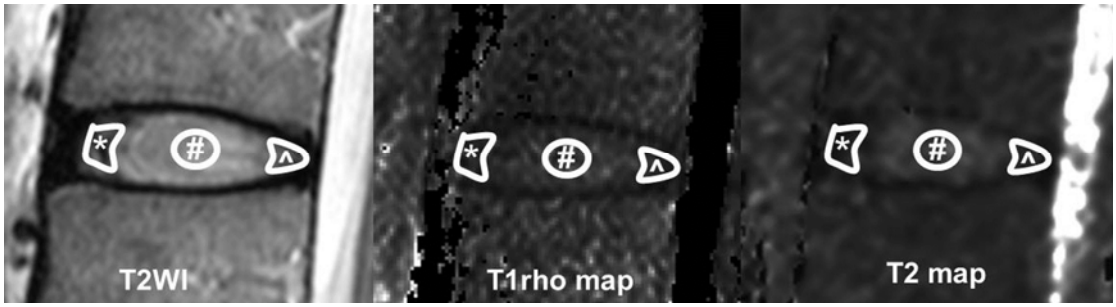

Figure 3.2: An example of placement of regions-of-interest (ROIs) over nucleus pulposus (#), anterior annulus fibrosus (*), and posterior annulus fibrosus (^) in one disc of T2-weighted image (left), T1rho map (middle), and T2 map (right).

The Pfirrmann five-level grading system is widely used for disc degeneration evaluation (Li et al., 2008, Pfirrmann et al., 2001). To increase the discriminatory power, a modification of the Pfirrmann system by increasing the number of grades

from 5 to 8 has been devised (Griffith et al., 2007). Broadly speaking, Pfirrmann Grade C (3/5) was expanded to two grades (Grades 3/8 and 4/8), while Pfirrmann Grade D (4/5) was expanded to three grades (Grades 5/8, 6/8 and 7/8). The degree of disc height narrowing was incorporated into this grading system, with grades≥6 involving disc height narrowing (Phillips et al., 2003). Five-level and eight-level disc degeneration evaluations were carried out by a radiologist experienced in reading these two disc degeneration grading systems.

All statistical analyses were done using SPSS v. 14.0 (SPSS, Chicago, IL). The difference in T1rho and T2 values of various disc degeneration grades was tested using the Mann–Whitney test or one-way ANOVA. When relaxation time was plotted against degeneration grading, NP showed a quadratic trend so a quadratic regression was fitted, and R^2 and quadratic coefficients are reported. R^2, the coefficient of determination, is the percentage of variance which can be explained by independent variables. AF had a linear trend so a linear regression was fitted, and R^2 and slope are reported. Quadratic coefficient and slope were tested in T1rho and T2 values by including an interaction term in the model. All statistical tests were two-sided. A P value of <0.05 was considered statistically significant.

3.3 Results

3.3.1 Range of T1rho/T2 Values for Discs

In this study, T1rho value for nucleus pulposus (NP) and annulus fibrosus (AF) ranged from 41.8 to 147.9ms and from 36.5 to 74.3ms, respectively. T2 value ranged from 24.8 to 148.1ms for NP, and from 23.7 to 64.4ms for AF.

3.3.2 The Relationship between NP T1rho/T2 Values and 8-level Degeneration Grading of Discs

The relationship between NP T1rho/T2 values and 8-level degeneration grading of the 256 discs is given in Figure 3.3. As the degeneration grading increased from grade 1/8 to grade 5/8, both T1rho and T2 values decreased, while there was no apparent difference between grades 5/8 to 8/8. The trend line for NP T1rho/T2 values against 8-level degeneration grading fitted by quadratic regression is shown in Figure 3.4. The quadratic coefficient (±SE) was 3.19±0.40 ($P<0.0001$, $R^2=0.62$) for T1rho value of NP, and 3.68±0.41 ($P<0.0001$, $R^2=0.69$) for T2 value of NP. There was no significant trend difference for the decrease in T1rho and T2 values over the increase in degeneration grade ($P=0.40$).

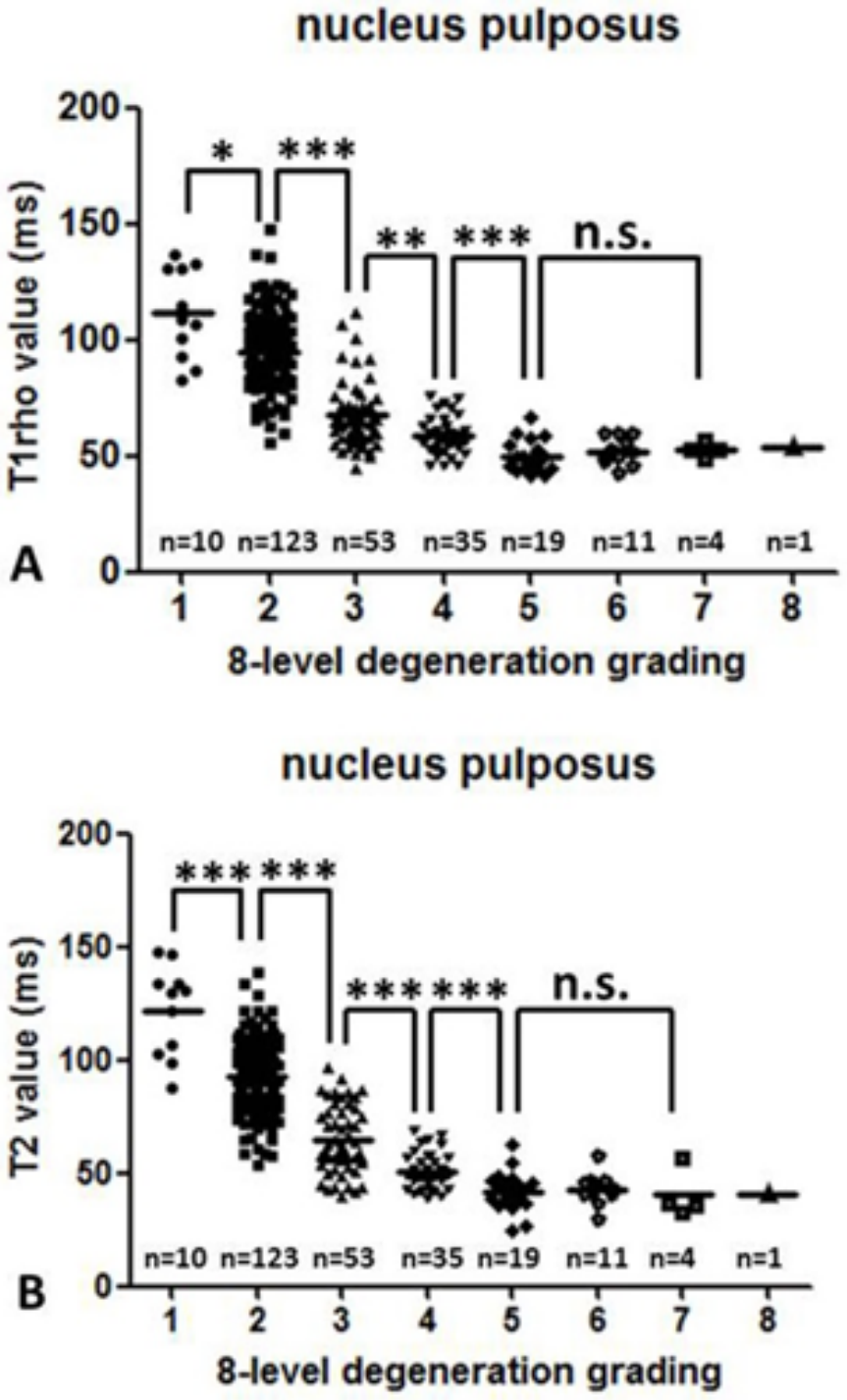

*Figure 3.3: A: The relationship between T1rho value of nucleus pulposus (NP) and 8-level degeneration grading. B: The relationship between T2 value of nucleus pulposus (NP) and 8-level degeneration grading. *:p<0.05; **:p<0.01; ***:p<0.001; n.s.: not significant.*

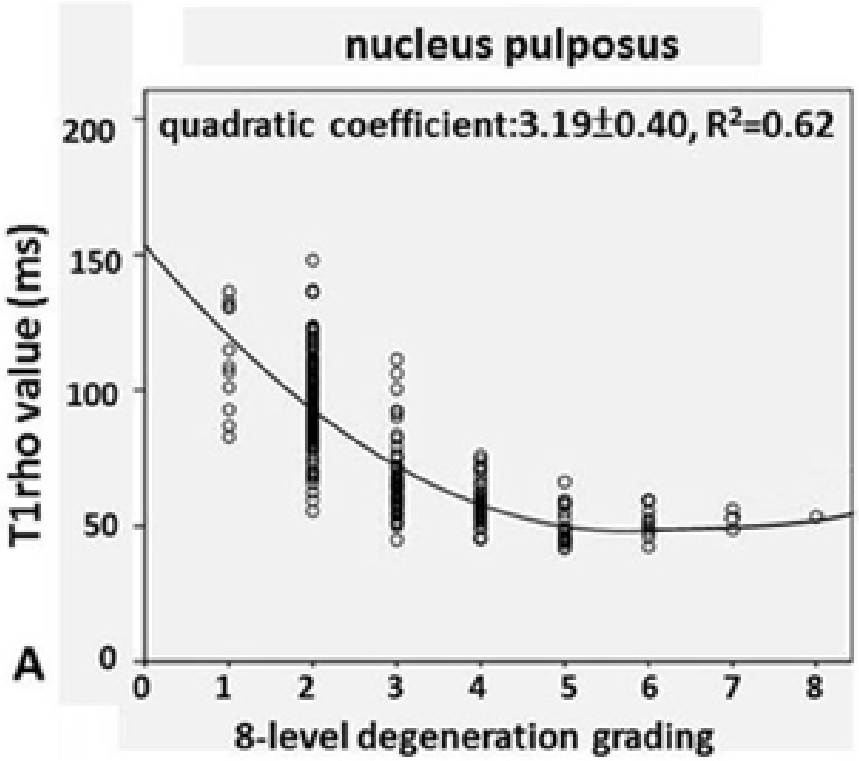

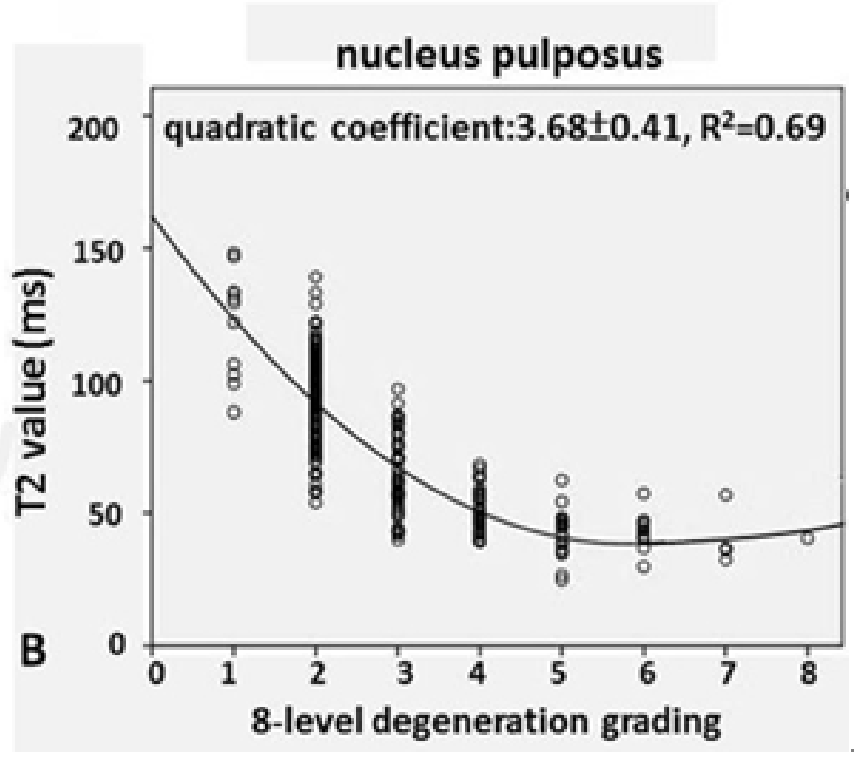

Figure 3.4: A: The quadratic regression of T1rho value of nucleus pulposus (NP) against 8-level degeneration grading. B: The quadratic regression of T2 of nucleus pulposus (NP) against 8-level degeneration grading.

3.3.3 The Relationship between NP T1rho/T2 Values and 5-level Degeneration Grading of Discs

The relationship between NP T1rho/T2 values and 5-level degeneration grading of the 256 discs is given in Figure 3.5. As the degeneration grading increased from grade 1/5 to grade 5/5, T1rho and T2 value decreased. The trend line for NP T1rho/T2 values against 5-level degeneration grading fitted by quadratic regression is shown in Figure 3.6. The quadratic coefficient (±SE) was 3.35±1.03 ($P<0.0013$, $R^2=0.64$) for T1rho value, and 5.35±1.04 ($P<0.0001$, $R^2=0.71$) for T2 value. There was no significant trend difference for the T1rho and T2 values decrease over degeneration grade increase ($P=0.17$).

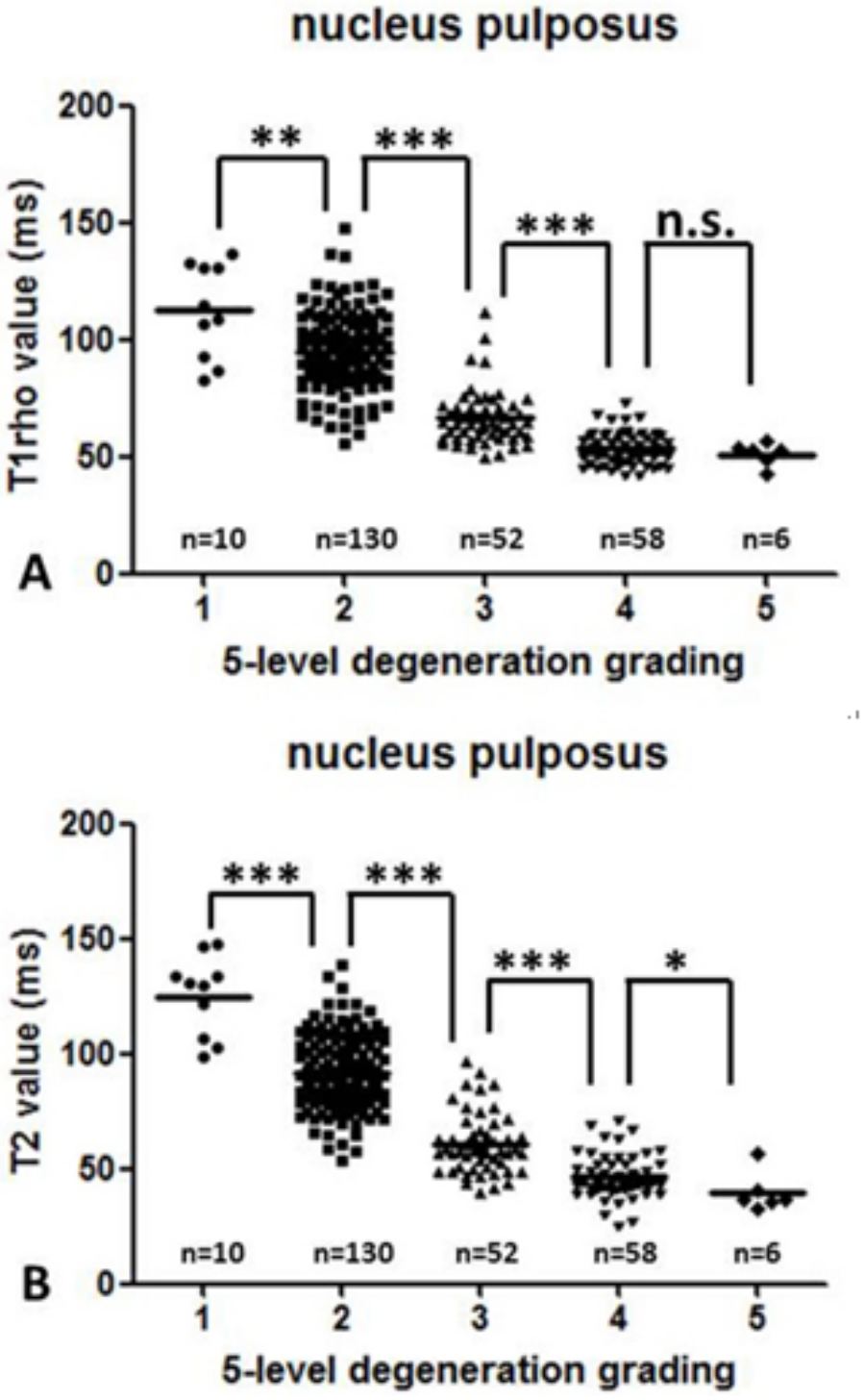

*Figure 3.5: A: The relationship between T1rho value of nucleus pulposus (NP) and 5-level degeneration grading. B: The relationship between T2 value of nucleus pulposus (NP) and 5-level degeneration grading. *:p<0.05; **:p<0.01; ***:p<0.001; n.s.: not significant.*

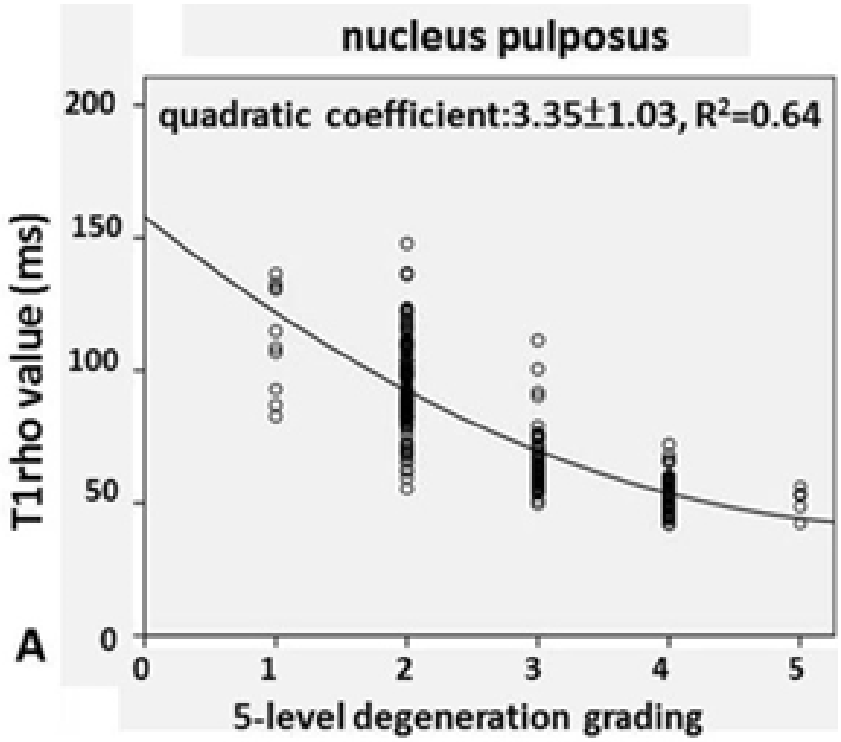

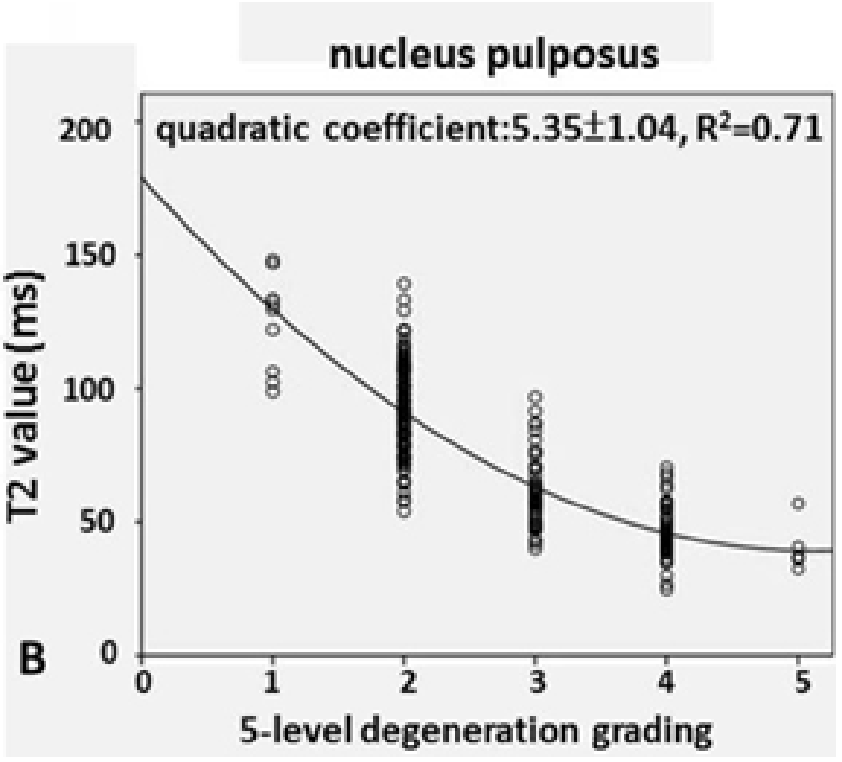

Figure 3.6: A: The quadratic regression of T1rho value of nucleus pulposus (NP) against 5-level degeneration grading. B: The quadratic regression of T2 of nucleus pulposus (NP) against 5-level degeneration grading.

3.3.4 The Relationship between AF T1rho/T2 Values and 8-level Degeneration Grading of Discs

The relationship between AF T1rho/T2 values and the eight-level grading of the 256 discs is shown in Figure 3.7. As the degeneration grade increased from 1/8 to 5/8, T1rho value decreased. On the other hand, the trend of the decrease in T2 relaxation time was much flatter. The trend line for AF T1rho/T2 values against 8-level degeneration grading fitted with linear regression is shown in Figure 3.8. The slope (± SE) was −3.02±0.32 ($P<0.0001$, $R^2=0.26$) for T1rho value, and −1.43±0.30 ($P<0.0001$, $R^2=0.08$) for T2 value. There was a significant difference in the slopes of the decrease in T1rho and T2 values over disc degeneration ($P=0.0004$).

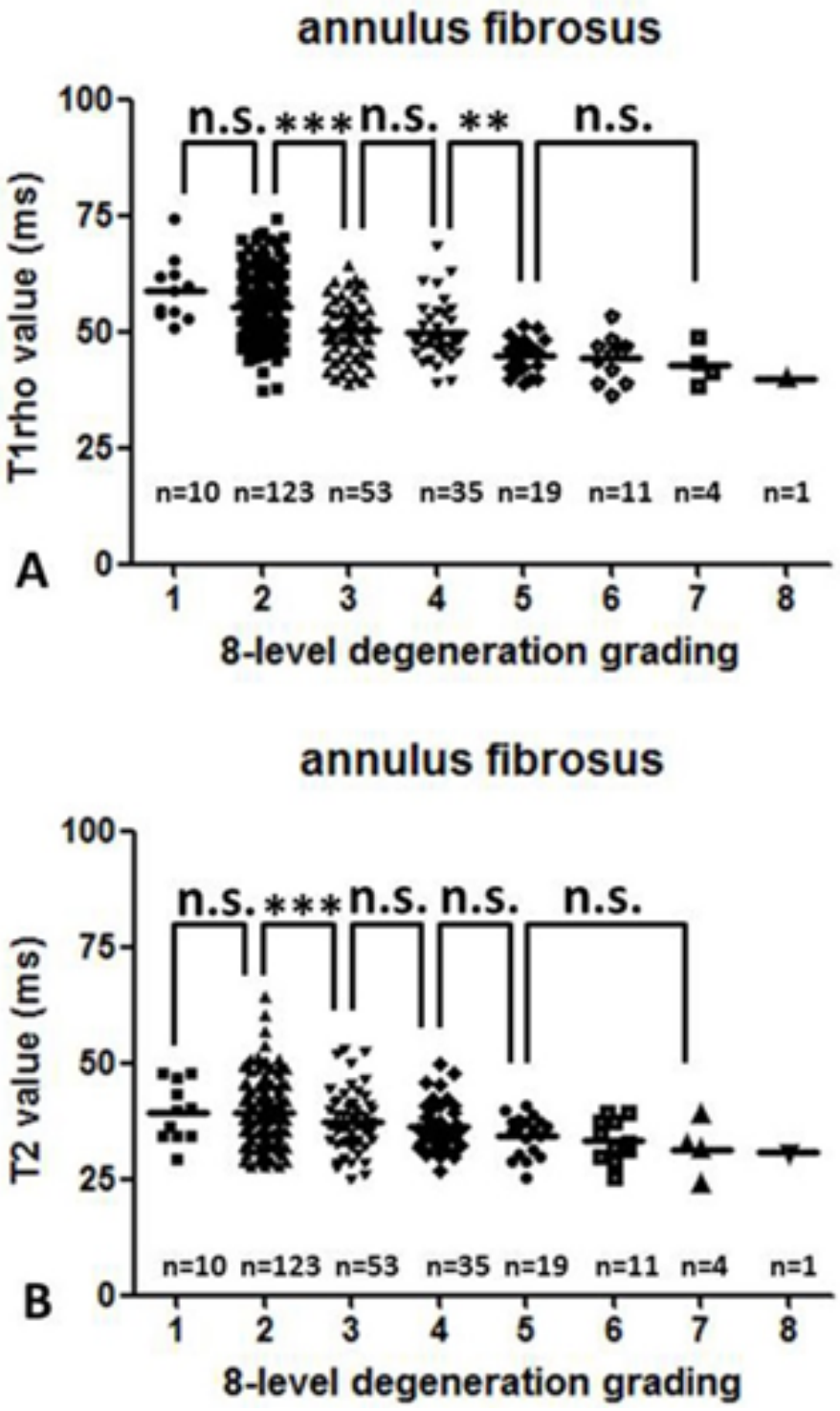

*Figure 3.7: A: The relationship between T1rho value of annulus fibrosus (AF) and 8-level degeneration grading. B: The relationship between T2 value of annulus fibrosus (AF) and 8-level degeneration grading. *:p<0.05; **:p<0.01; ***:p<0.001; n.s.: not significant.*

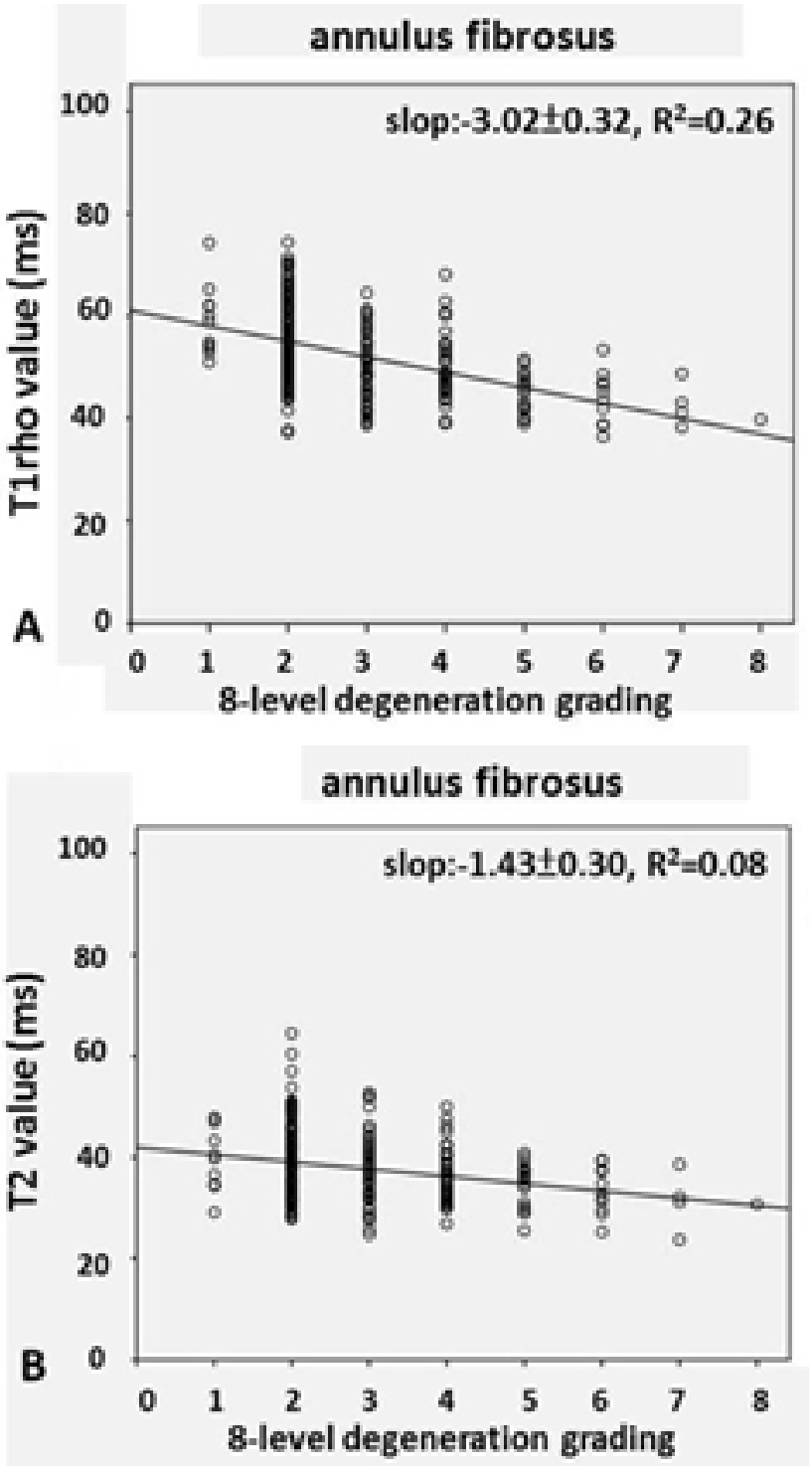

Figure 3.8: A: The linear regression of T1rho value of annulus fibrosus (AF) against 8-level degeneration grading. B: The linear regression of T2 of annulus fibrosus (AF) against 8-level degeneration grading.

3.3.5 The Relationship between AF T1rho/T2 Values and 8-level Degeneration Grading of Discs

The relationship between AF T1rho/T2 values and the five-level grading of the 256 discs is shown in Figure 3.9. As the degeneration grade increased, T1rho value decreased. On the other hand, the trend of the decrease in T2 value over the increase in disc degeneration was much flatter. The trend line for AF T1rho/T2 values against 5-level degeneration grading fitted with linear regression is shown in Figure 3.10. The slope (± SE) was −4.56±0.45 ($P<0.0001$, $R^2=0.29$) for T1rho relaxation time, and −1.84±0.44 ($P<0.0001$, $R^2=0.07$) for T2 relaxation time. There was a significant difference in the slopes of T1rho and T2 values ($P=0.002$).

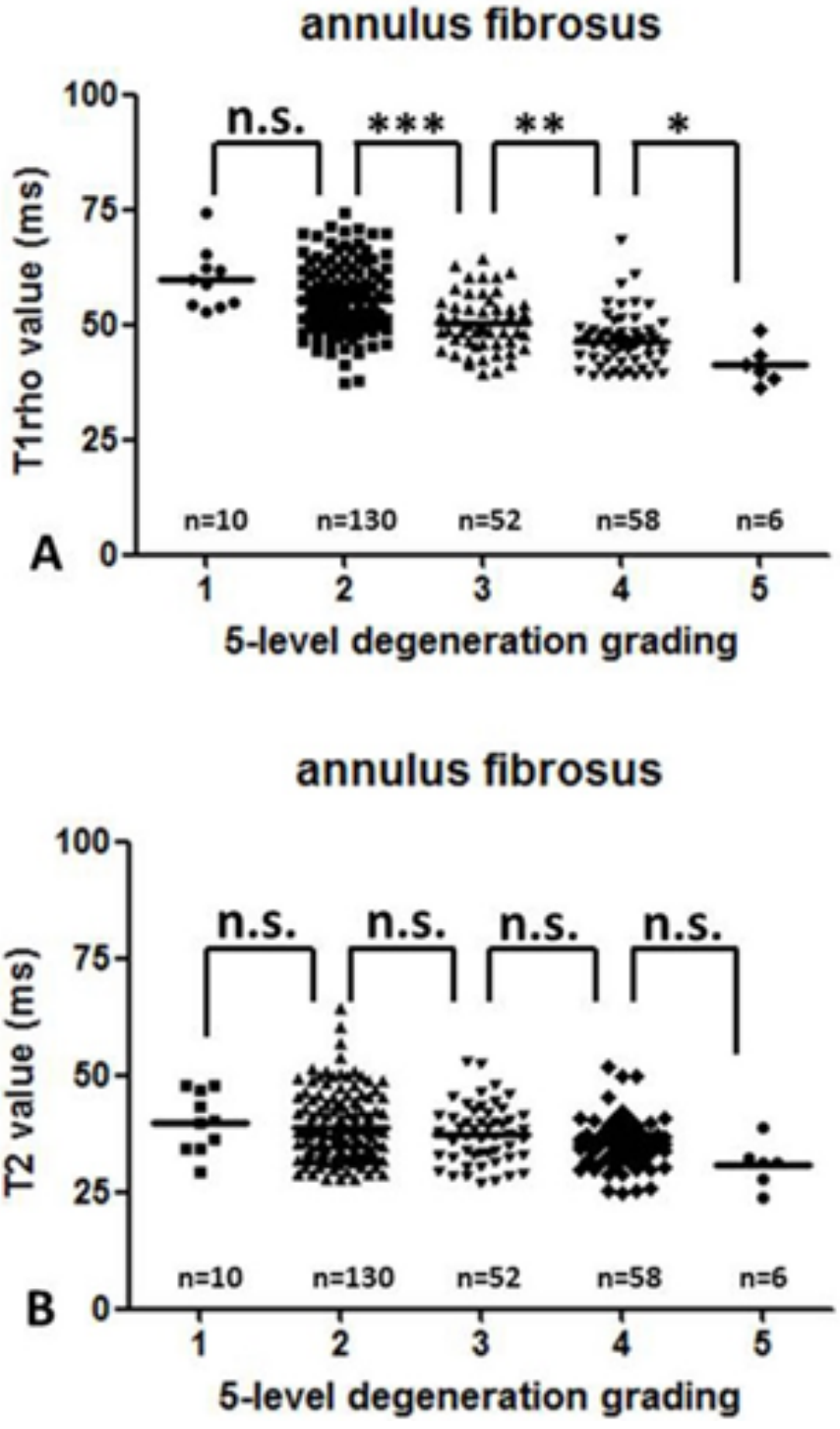

*Figure 3.9: A: The relationship between T1rho value of annulus fibrosus (AF) and 5-level degeneration grading. B: The relationship between T2 value of annulus fibrosus (AF) and 5-level degeneration grading. *:p<0.05; **:p<0.01; ***:p<0.001; n.s.: not significant.*

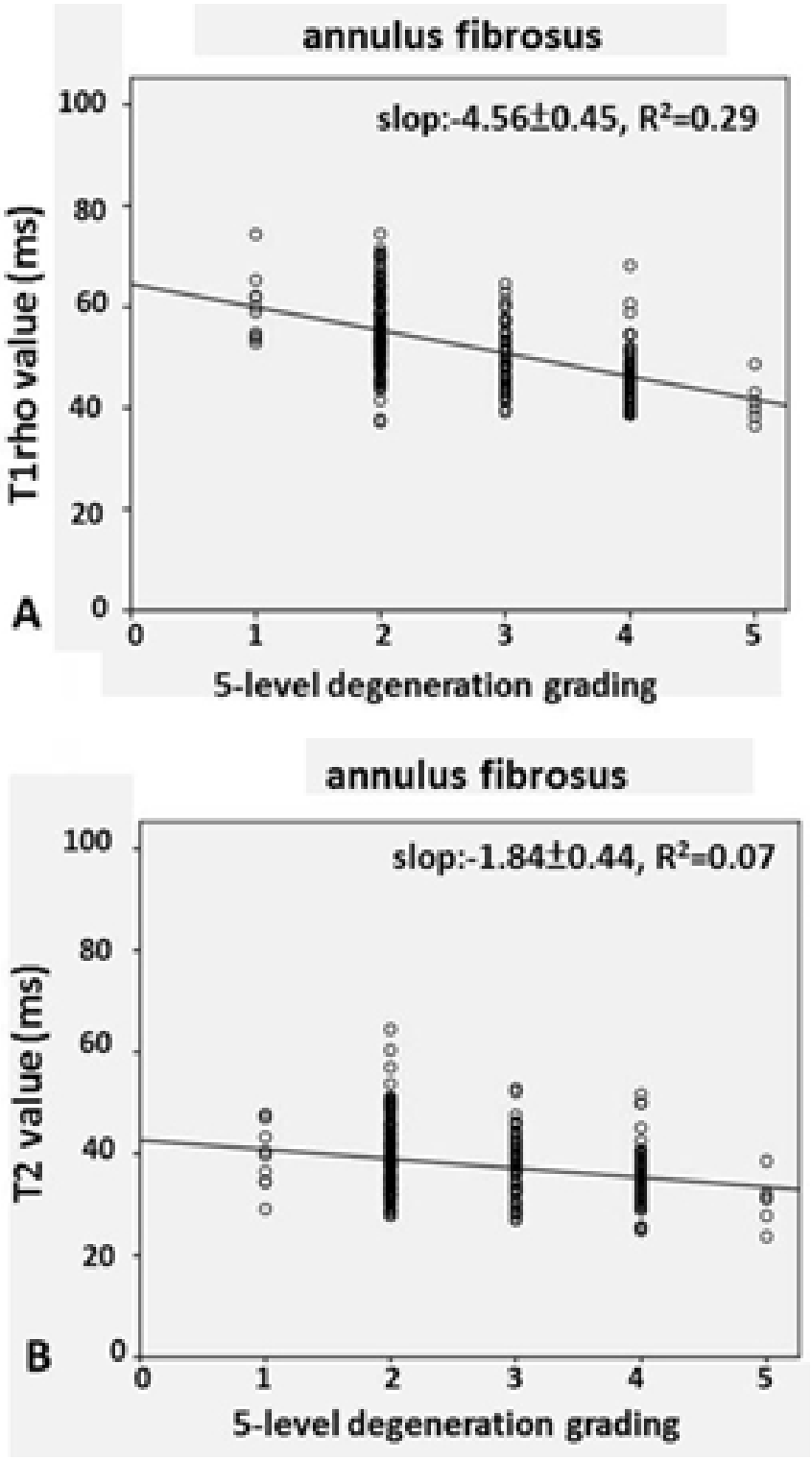

Figure 3.10: A: The linear regression of T1rho value of annulus fibrosus (AF) against 5-level degeneration grading. B: The linear regression of T2 of annulus fibrosus (AF) against 5-level degeneration grading.

3.4 Discussion

Compared with previous studies (Auerbach et al., 2006; Blumenkrantz et al., 2006; Blumenkrantz et al., 2010), much larger number of subjects were included in this study, including non-symptomatic volunteers as well as patients with low-back pain. We evaluated 23- to 76-year-old subjects, an age range in which a broad spectrum of disc degeneration, including early degeneration, is expected.

Both T1rho mapping and T2 mapping were acquired, and NP and FA were analyzed separately. MR images were acquired sagittally so that all the five lumbar discs can be analyzed in a single plane. Additionally, both semi-quantitative five-level and eight-level grading systems were applied in this study. The disc T1rho/T2 values from the current study were consistent with studies reported by other groups (Auerbach et al., 2006; Blumenkrantz et al., 2010; Krueger et al., 2007; Marinelli et al., 2009; Nguyen et al., 2008).

This study confirmed the previously reported negative relationship between T1rho /T2 value and disc degenerative grade (Auerbach et al., 2006; Blumenkrantz et al., 2010; Chiu et al., 2001; Kerttula et al., 2001; Nguyen et al., 2008). As in previous reports, there were overlaps in T2 and T1rho values among different semi-quantitative grades. This needs to be viewed in the context that disc degeneration is a continuum

rather than a discrete process. As a result, any discrete grading system will by design contain ambiguity with respect to the grading categories. A semi-quantitative grade system also suffers from subjectivity during grading by the radiologist.

For NP, our study showed that T1rho/T2 values followed the same trend with their correlations with semi-quantitative gradings. T1rho value did not seem to offer any additional advantage over T2 relaxation time in differentiating different severities of disc degeneration. While progression from grade 1 to grade 2 is likely related to normal ageing, it is possible that early treatment before disc space narrowing takes place (i.e. < grade 6/8) will be more beneficial for the discs. It is noted that when using the five-level grading as reference, the quadratic coefficient was higher for NP T2 value than for NP T1rho value, although the difference was not statistically significant (P=0.17). This is likely because there was a higher difference between grade 1/5 and 2/5 discs for T2 relaxation time than for T1rho relaxation time (Figure 3.5, Figure 3.6), while this in turn could be due to the grading being based on T2-weighted images, i.e. higher T2 value rendered the discs to be graded as grade 1/5.

On the other hand, very interestingly, T1rho value offered a distinct advantage over T2 value in the evaluation of AF degeneration. While there were almost no changes in T2 values as the disc degeneration grades increased, T1rho value decreased apparently as disc degeneration grades increased. It is well known that AF

degeneration is a critical factor in disc stability (Modic and Ross, 2007). We also carried out separate analysis for anterior AF and posterior AF, and no difference was seen in their changes related to disc degeneration.

The role of specific biochemical changes in the altered MR signal intensity is still not well understood in the reported literature. In the articular cartilage study, the loss of proteoglycan results in an increase in T1rho relaxation time (Akella et al., 2001). On the other hand, T1rho is reported to increase with sulphated glycosaminoglycan content in degenerative discs (Johannessen et al., 2006). NP is composed of abundant sulphated glycosaminoglycans in a loose network of Type II collagen. It is a hydrated gel containing approximately 25% (dry weight) collagen and 50% (dry weight) proteoglycan (Cassinelli et al., 2001). The proteoglycans of the nucleus osmotically exert a "swelling pressure", which enables it to support spinal compressive loads. In comparison, AF is made up of coarse Type I collagen fibers, and contains 67% (dry weight) collagen and a low concentration of proteoglycans (Cassinelli et al., 2001; Weidenbaum et al., 1992). During the initial phase of disc degeneration, loss of proteoglycans and collagen Type II is observed (Antoniou et al., 1996). Proteoglycan loss reduces the capacity to bind water and leads to a loss of hydration. Later, Type I collagen fibres replace the Type II collagen fibres in the annulus (Adams and Roughley, 2006), thus altering the tensile properties of the tissue. While the reduced

water content is a contributing factor of the reduction of T1rho and T2 with degenerated discs (Johannessen et al., 2006), T1rho and T2 relaxations represent different contrast mechanisms and may provide complementary information about the integrity of the disc, and the differences in relaxation times may be linked to the varying tissue compositions and material properties. The T1rho reduction in AF during disc degeneration may represent some macromolecular changes that occur during the process. To better understand the difference in T1rho/T2 values reduction during the course of NP and AF degeneration, and to translate these relaxation times into reliable and specific biomarkers for early disc degeneration (Wang, 2005), additional in vitro studies are warranted to further evaluate the role of MR relaxometry in disc evaluation.

It is noted in this study that, for both NP and AF, discs of grade 5/8 to 8/8 degenerations had similar T1rho/T2 values. The eight-level grading system offers information on disc space narrowing, i.e. <30% reduction in disc height for grade 6/8, 30–60% reduction in disc height for grade 7/8 and >60% reduction in disc height for grade 8/8 (Griffith et al., 2007).

By using the eight-level grading system to study elderly men and elderly women, it was found that elderly female subjects had more severe disc degeneration than male subjects at all lumbar levels, and elderly women were more likely to have a narrowed

lumbar disc space than elderly men (Griffith et al., 2007; Wang and Griffith, 2010; Wang et al., 2011b). As disc space narrowing is more likely to cause low-back pain (Hassett et al., 2003; Videman et al., 2003), our results suggest that even when T1rho /T2 value are routinely measured for disc degeneration assessment in the future, the eight-level grading system will still be useful for clinical evaluation, particularly for those with severe disc degeneration and disc space narrowing.

There are a few limitations with the current study. The placement of ROIs on disc regions was carried out manually. It is possible that there would be differences in ROIs on T1rho maps and T2 maps. However, such differences would be rather small and unlikely to affect the conclusion of this study. The correlation between T1rho and T2 relaxation times and clinical symptoms, particularly the duration of low-back pain, of the patients was not investigated. In fact, neither could we be certain that the back pain of our patients was solely disc related. It was previously reported that only a weak correlation exists between the level of disc degeneration and clinical symptoms (Peterson et al., 2000), and imaging findings of degenerative disc disease do not predict subsequent symptom development (Borenstein et al., 2001). The effect of ageing on disc component relaxation time was not investigated, as the primary focus of this study was to compare the relative performance of T1rho and T2 for disc degeneration evaluation.

3.5 Summary

Both T1rho value and T2 value decrease following disc degeneration. For NP, T1rho value and T2 value decrease in a similar pattern following disc degeneration. For AF, T1rho value decrease progressively faster than T2 value. Therefore, T1rho value is better suited for evaluating AF in degenerated disc than T2 value. Both T1rho and T2 value does not reduce further by disc-space narrowing, therefore, the eight-level grading system will still be useful for clinical evaluation, particularly for those with severe disc degeneration and disc space narrowing.

CHAPTER 4 T1RHO MRI IN RAT LIVER FIBROSIS MODEL INDUCED BY CCL4 INSULT

4.1 Introduction

Chronic liver disease is a major public health problem worldwide (Charlton, 2004; Davis et al., 2003; Zhou and Lu, 2009). Liver fibrosis is a common feature of almost all chronic liver diseases, involving the accumulation of collagen, proteoglycans, and other macromolecules in the extracellular matrix. Ultimately, progressive hepatic fibrosis leads to cirrhosis, which is a characteristic of all end-stage liver disease (Wallace et al., 2008).

Clinically, liver fibrosis usually has an insidious onset and progresses slowly over decades. Patients remain asymptomatic or have only mild, nonspecific symptoms until the development of cirrhosis. Cirrhotic patients may have various sequelae of hepatic decompensation, including variceal hemorrhage, ascites, hepatic encephalopathy, and hepatic and renal failure. Cirrhosis is also a risk factor for the development of hepatocellular carcinoma.

Originally, liver fibrosis was considered to be irreversible; however there is increasing evidence that liver fibrosis is a dynamic process with potential for regression (Arthur, 2002; Veldhuijzen et al., 2010; Wallace et al., 2008; Wanless et al.,

2000). To date, noninvasive diagnostic tests available from clinical practice are not sensitive or specific enough to be used to detect occult liver injury at early or intermediate stages. Liver biopsy is the standard of reference for the diagnosis and staging of liver fibrosis. However, liver biopsy is an invasive procedure with possible complications (Janes and Lindor, 1993). In addition, the histologic assessment of fibrosis is also an inherently subjective process, and it is subject to sampling variability (Poniachik et al., 1996).

To better treat individuals with progressive fibrosis, especially those who might benefit from early intervention, a reproducible and reliable noninvasive method is needed to evaluate disease progression, to monitor responses to drug treatment, and to benefit epidemiologic research. T1rho MRI is sensitive to both low frequency motional processes and static processes, so it can be used to investigate macromolecular composition and proton exchange in tissues. Wang et al (Wang et al., 2011a) showed that T1rho value became prolonged after bile duct ligation (BDL) induced liver injury of rat model and that the T1rho value increased with the severity of liver fibrosis. These results suggest that liver T1rho MRI may play an important role for the early detection and grading of liver fibrosis.

However, a few important questions remain to be answered. (1) Is MR T1rho sensitive to liver fibrosis with an aetiology other than biliary fibrosis? (2) How does

liver inflammation and edema affect liver T1rho values? (3) Can MR T1rho be used to monitor liver fibrosis regression?

The purpose of study described in this Chapter is to answer these questions by carrying out the T1rho MRI on the rat liver fibrosis model induced with chronic carbon tetrachloride (CCl4) insult.

4.2 Materials and Methods

4.2.1 Animal Preparation

Eight male Sprague-Dawley rats with initial weights between 200 and 250 g were used in the pilot study to assess the MRI measurement reproducibility, and 27 male Sprague-Dawley rats of similar body weight were used for the experimental study. The animals were housed on a 12-h light/12-h dark cycle in an air conditioned room at 25°C. Food and water were available ad libitum.

Liver fibrosis in rats was induced by intraperitoneal injection of 2ml/kg body weight CCl4 twice weekly, up to 6 weeks, with a 1:1 volume mixture of CCl4 (99.8%; BDH Laboratory, Poole, UK) in olive oil. All rats were weighed twice a week in order to adjust the CCl4 dosage according to their body weight. At the end of week 6, CCl4 administration was withdrawn, and the rats were allowed to recover for 4 weeks.

4.2.2 MR Image Acquisition

Data acquisition was performed using a commercially available 3-T clinical MR system (Achieva, Philips Healthcare, Best, The Netherlands). The Ketamine/Xylazine combination anesthetic was used for MR scanning; the dose of Ketamine/Xylazine for rat in this study was 100 mg/kg and 10 mg/kg body weight. After anesthesia, animals were positioned supine and an eight-channel human wrist radiofrequency (RF) coil was used as the signal receiver, and the in-built body coil was used as the signal transmitter. Five axial slices were selected to cut through liver.

For the reproducibility study, eight rats without CCl4 insult were MR imaged twice with an interval of 10 days. Experimental animals were MR imaged at baseline before CCl4 injection (n=12), 2 days (i.e. 48 h) post initial CCl4 injection (n=12), and 2 weeks (n=12), 4 weeks (n=10), 6 weeks (n=7) post the initiation of CCl4 injection, and also MR imaged at 1week (n=4) and 4 weeks post the cessation of CCl4 injection (n=7). The experiment set-up is described in Figure 4.1.

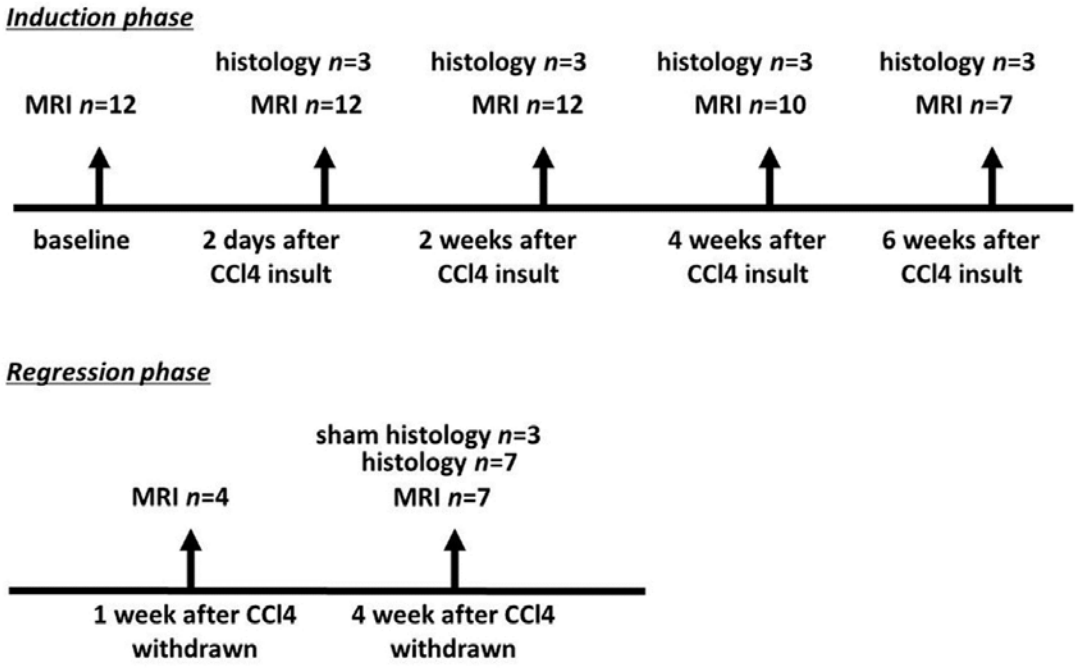

Figure 4.1: Schedule of CCl4 administration for the induction of liver fibrosis in adult Sprague-Dawley rats, MRI data acquisition and liver histology.

4.2.2.1 T2-weighted MRI

Conventional T2-weighted images of rat liver were acquired by 2D multiple slice turbo spin echo (TSE) sequences (repetition time, TR=2000ms; echo time, TE=80ms; FOV=80×66×10 mm^3; voxel size = 0.5×0.5×2.0mm^3; 5 slices; section thickness 2 mm; intersection gap 0 mm; number of signal averages, NSA=4). The scan time of conventional T2 weighted image was 84 s.

4.2.2.2 T1rho MRI

The diagram sequence for T1rho MRI is given in Figure 4.2. For T1rho measurement, a rotary-echo spin-lock pulse was implemented in a three-dimensional

balanced fast field echo sequence. Spin-lock frequency was set as 500 Hz, and the spin-lock times of 1, 10, 20, 30, 40, and 50ms were used for T1rho mapping. The subsequent normal-phase alternating balanced fast field-echo readout was used for acquisition. Inversion time (delay time) after acquisition was set as 6000ms to restore equilibrium magnetization prior to the next T1rho preparation. Volume shimming was employed to minimize B_0 inhomogeneities. TE and TR for b-FFE acquisition were 2.6ms and 5.3ms, respectively. The voxel size was 0.5×0.5×2.00 mm^3. The flip angle was 40 degree and the number of signal averages (NSA) was 4. No sensitivity-encoding (SENSE) factor was applied for parallel imaging to reduce the phase-encoding steps. The scan time was about 3 minutes per spin-lock time point.

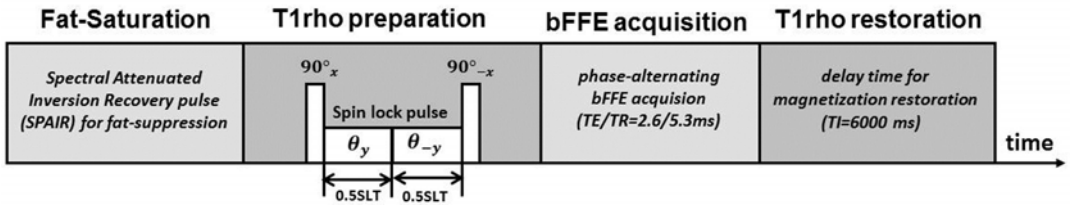

Figure 4.2: Diagram of the sequence for T1rho MRI, which is the spin-lock balanced fast field echo (b-FFE) imaging sequence for T1rho MRI, the rotary echo spin-lock pulse cluster is used for T1rho preparation. SLT= spin-lock time.

4.2.3 Data Processing

T1rho maps were computed on a pixel-by-pixel basis by using a mono-exponential decay model with a homemade Matlab program (Mathworks, Natick, MA):

$$M(SLT) = M_0 \cdot \exp^{(-SLT/T1rho)}$$ Equation [1.4]

Where M_0 and M(SLT) denote the equilibrium magnetization and T1rho-prepared magnetization with the spin-lock time of SLT, respectively. This mono-exponential equation was linearized by logarithm and T1rho maps were generated by fitting all pixel intensity data as a function of SLT using linear regression. T1rho was calculated as -1/slope of the straight line fit. T1rho maps were constructed using all 6 SLT points (1, 10, 20, 30, 40, and 50ms). Maps of coefficient of determination (R^2) were also generated for the evaluation of goodness of fit. Only T1rho values for pixels associated with R^2>0.80 were included in the subsequent region of interest (ROI) placement and T1rho analysis to eliminate the unreliable poorly fitted T1rho values due to the blood vessel contamination with fresh blood inflow, as well as respiration-induced artifacts. One typical rat's T1rho-weighted image acquired with different times of spin-lock (SLT) ranging from 1 to 50ms, coefficient of determination (R^2) map, and T1rho map without R^2 evaluation are shown in Figure 4.3.

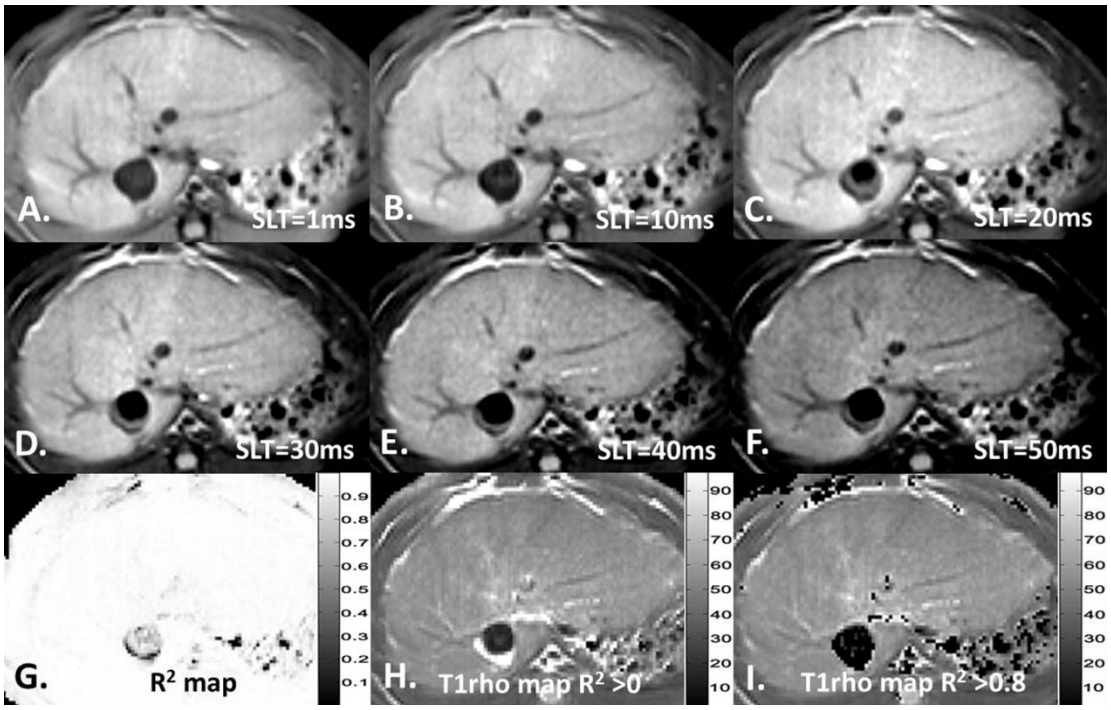

Figure 4.3: One typical rat's T1rho-weighted image acquired with different spin-lock time (SLT) ranging from 1 to 50ms (A-F). One typical rat's coefficient of determination (R^2) map (G), T1rho map without R^2 evaluation (H), and T1rho map with R^2>0.8 evaluation (I).

4.2.4 Data Measurement and Statistical Analysis

To quantify T1rho values on T1rho maps and liver signal intensities on T2-weighted images, five regions-of-interest (ROIs) of approximately 3-4 mm^2 (12-16 pixels) were placed on liver parenchyma region of each slice's T1rho maps with R^2>0.80, excluding observable artifacts and blood vessels, leading to a total of 25 ROIs from each liver for each technique. For T2-weighted images, the mean signal intensity of liver parenchyma was normalized by the signal intensity of the back

muscle on the same image, i.e. the ratio of the liver signal intensity and back muscle intensity was obtained. The mean value of these 25 ROIs was regarded as the liver T1rho value or the relative liver signal intensity of the rat.

Data are presented as mean ± standard deviation. For the reproducibility study, scan-rescan intraclass correlation coefficient (ICC) and Bland and Altman plot were evaluated. According to Fleiss (Fleiss, 1986), an ICC value of <0.4 represents poor agreement, a value >0.75 represents good agreement and a value between 0.4 and 0.75 represents fair to moderate agreement. In addition, to assess the homogeneity of 25 ROIs' MR measurement in each rat, coefficient of variation (CoV) was calculated for each of the eight rats for the pilot study. All statistical analyses were done using SPSS 14.0 (SPSS, Chicago, IL). The Mann-Whitney U test was used for non-paired comparison. A P value <0.05 was considered statistically significant.

4.2.5 Histology Analysis

For histopathological examination, animals were killed on day 2 (n=3), week 2 (n=3), week 4 (n=3) and week 6 (n=3), and 4 weeks post the cessation of CCl4 injection (n=7), respectively. Three control rats, which were age-matched but without any CCl4 insult, were also killed for histology at the end of the study. Liver specimens were fixed in 4% phosphate-buffered formaldehyde and embedded in

paraffin. Sections 5-μm thick were de-waxed in xylene and rehydrated in ethanol. In addition to standard haematoxylin and eosin (H & E) staining, sections were also processed with 0.1% picrosirius red for collagen visualization.

4.3 Results

4.3.1 T1rho Measurement Reproducibility

The liver T1rho value and normalized liver signal intensity on T2-weighted images of eight rats without CCl4 insult in two MR scans with an interval of 10 days is given in Table 4.1. This pilot study showed the ICC of scan-rescan reproducibility for liver T1rho measurement was 0.83. The Bland and Altman analysis showed a mean difference of 0.33 (95% limits of agreement: -0.74, 1.39) for liver T1rho measurement. The ICC of scan-rescan reproducibility for normalized liver signal intensity on T2-weighted images measurement was 0.77. The Bland and Altman analysis showed a mean difference of 0.004 (95% limits of agreement: -0.26, 0.27) for normalized liver signal intensity on T2-weighted images measurement. These results suggest both the liver T1rho measurement and normalized liver signal intensity on T2-weighted images measurement had a good agreement in repeat MR examinations.

The CoV (coefficient of variation) of the 25 ROIs in each rat was 3.61±0.56% for

liver T1rho measurement and 7.27±1.07% for measurement of normalized liver signal intensity.

Table 4.1: Liver T1rho values and normalized liver signal intensity on T2-weighted images of eight rats without CCl4 insult in two MR scans with an interval of 10 days.

Rat No.	Liver T1rho values (ms)		Normalized liver signal intensity on T2-weighted images	
	Scan 1	Scan 2	Scan 1	Scan 2
1	45.38	45.8	1.68	1.57
2	43.62	43.9	1.73	1.73
3	44.88	44.43	1.77	1.69
4	43.04	42.96	1.79	1.65
5	45.3	44.65	1.61	1.62
6	44.2	43.78	1.61	1.56
7	43.62	42.32	1.39	1.68
8	43.5	43.1	1.49	1.54
mean	**44.19**	**43.87**	**1.63**	**1.63**
SD	0.89	1.10	0.14	0.07

4.3.2 Rat Liver T1rho Values at Different Time Phase

The normal rat liver T1rho value was 44.1±1.0ms at baseline measurement. Two days post the initiation of CCl4 insult, the liver T1rho value was 46.1±1.3ms, which represents an increase of 4.4%. At weeks 2, 4, and 6, the liver T1rho values were 49.4±3.7ms, 51.4±3.8 ms and 54.3±2.9ms, respectively; corresponding to increases over the baseline values of 12.0%, 16.5% and 23.0%, respectively (Figure 4.4). At weeks 1 and 4 after the withdrawal of CCl4 insult, liver T1rho values were 46.8±2.0ms and 45.1±0.6ms, respectively, with an increase over the baseline values of

6.1% and 2.3%, respectively (Figure 4.4). Typical T1rho maps of rat liver at different time phases are shown in Figure 4.5.

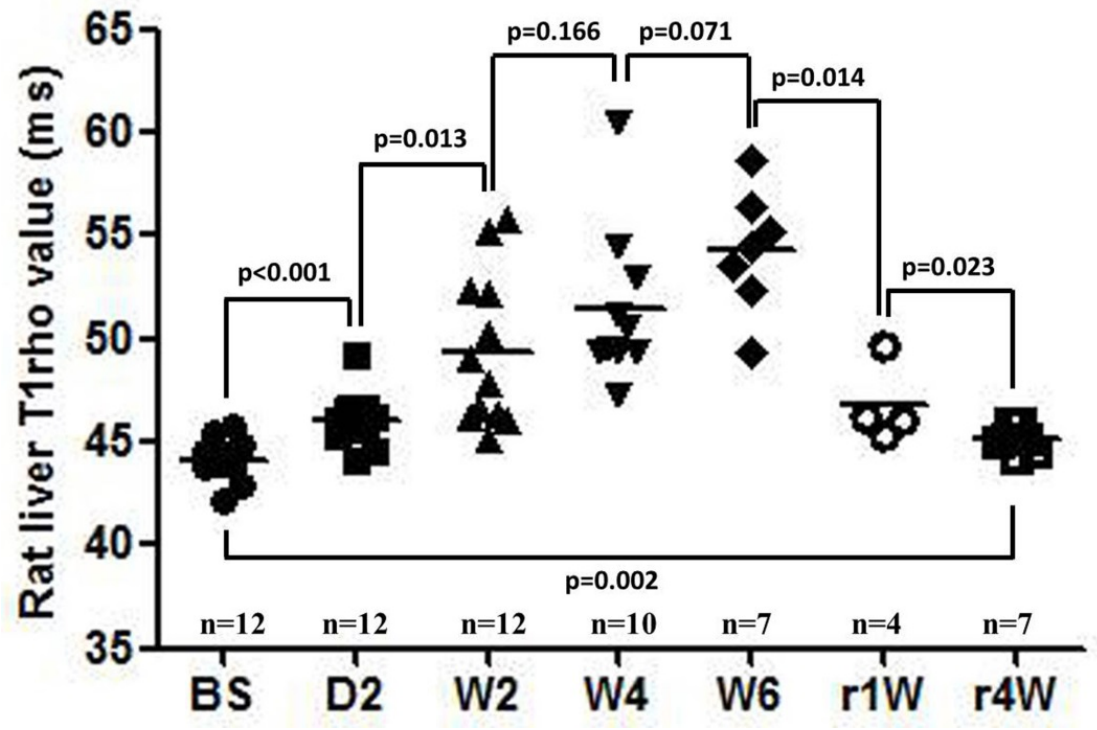

Figure 4.4: Longitudinal follow-up MRI measurements of rat liver T1rho values.

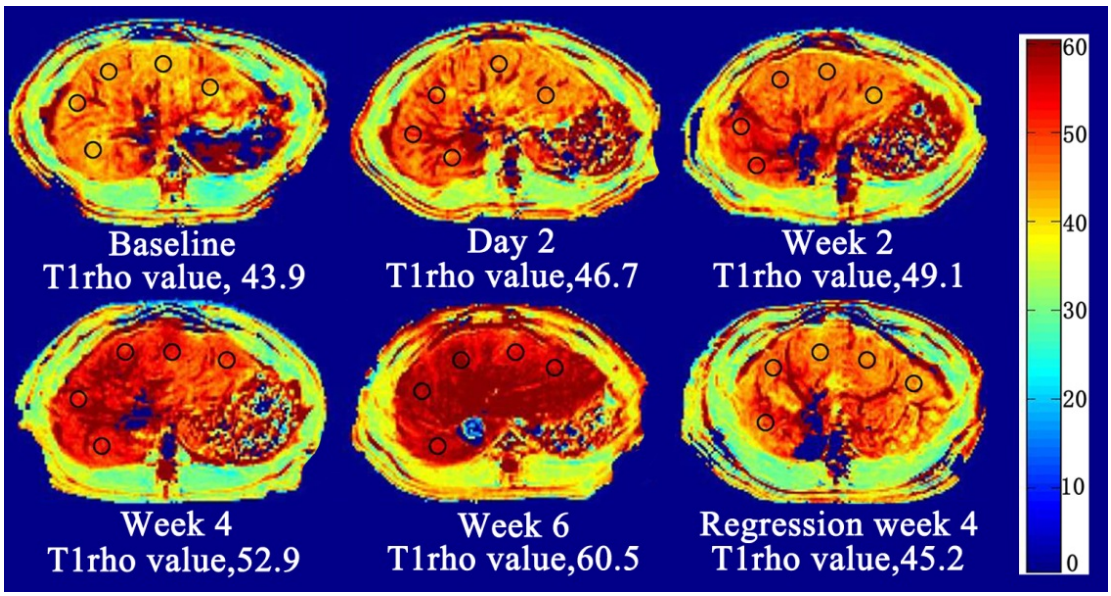

Figure 4.5: Typical T1rho maps of rat liver at different time phases.

4.3.3 Relative Rat Liver Signal Intensity on T2WI at Different Time Phase

The normalized liver signal intensity on the T2-weighted image was 0.94±0.15 at baseline. Two days post the initiation of CCl4 insult, this value was 1.30±0.20, representing an increase of 38.3%. At weeks 2, 4 and 6, normalized liver signal intensities on T2-weighted images were 1.34±0.15, 1.38±0.11 and 1.33±0.14, respectively, corresponding to an increase over the baseline value of 41.8%, 46.4%, and 41.5%, respectively (Figure 4.6). There were no significant differences of the normalized T2-weighted liver signal intensities between weeks 2, 4 and 6. At weeks 1 and 4 after the withdrawal of CCl4 insults, the normalized liver signal intensities on the T2-weighted images were 1.14±0.16 and 0.96±0.10, respectively, corresponding to baseline value increases of 21.3% and 1.8% respectively (Figure 4.6).

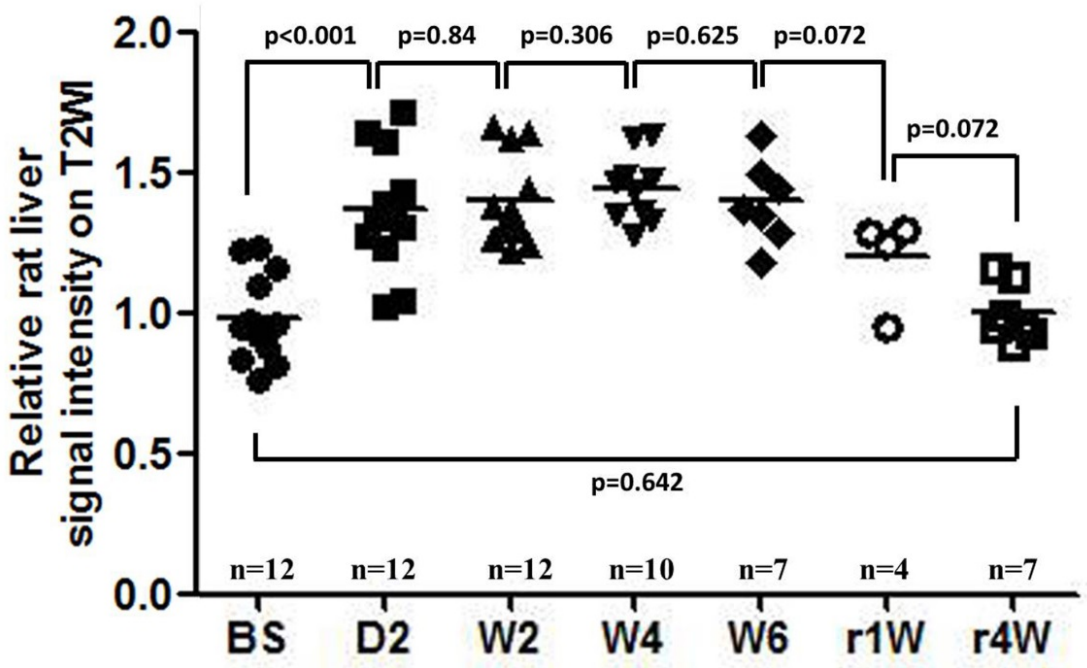

Figure 4.6: Longitudinal follow-up MRI measurements of relative rat liver signal intensity on T2WI .

4.3.4 Histology Results

H & E and picrosirius-red staining were performed for histological and collagen assessments. No abnormality in parenchymal architecture was observed among control rats (Figure 4.7A, Figure 4.8A). Extensive infiltration of inflammatory cells, intracellular deposition of fat vacuoles and hepatocellular swelling, as well as mild peri-central lobular liver necrosis were observed in the liver 2 days after CCl4 insult, while no apparent collagen deposition was observed at this time point (Figure 4.7B, Figure 4.8B). At week 2 of CCl4 insult, early fibrosis was seen, with scattered collagen deposition in the sinusoids of the peri-central lobular area without septa (Figure 4.7C, Figure 4.8C). At week 4 (Figure 4.7D, Figure 4.8D) and week 6 (Figure 4.7E, Figure 4.8E) of CCl4 insult, further fibrosis development was noted. Collagen deposition was more pronounced in the liver at 6 weeks of CCl4 insult. The specimens collected at 6 weeks exhibited septa formation with collagen deposition forming portal–portal and portal–central bridges. Infiltration of inflammation cells, intracellular deposition of fat vacuoles, as well as degeneration and necrosis of hepatocytes were consistently observed in livers after 2, 4 and 6 weeks of CCl4 insult.

Four weeks after the withdrawal of CCl4, active inflammation, fatty infiltration and necrotic cells disappeared, while mild residual fibrous band was still observed (Figure 4.7F, Figure 4.8F).

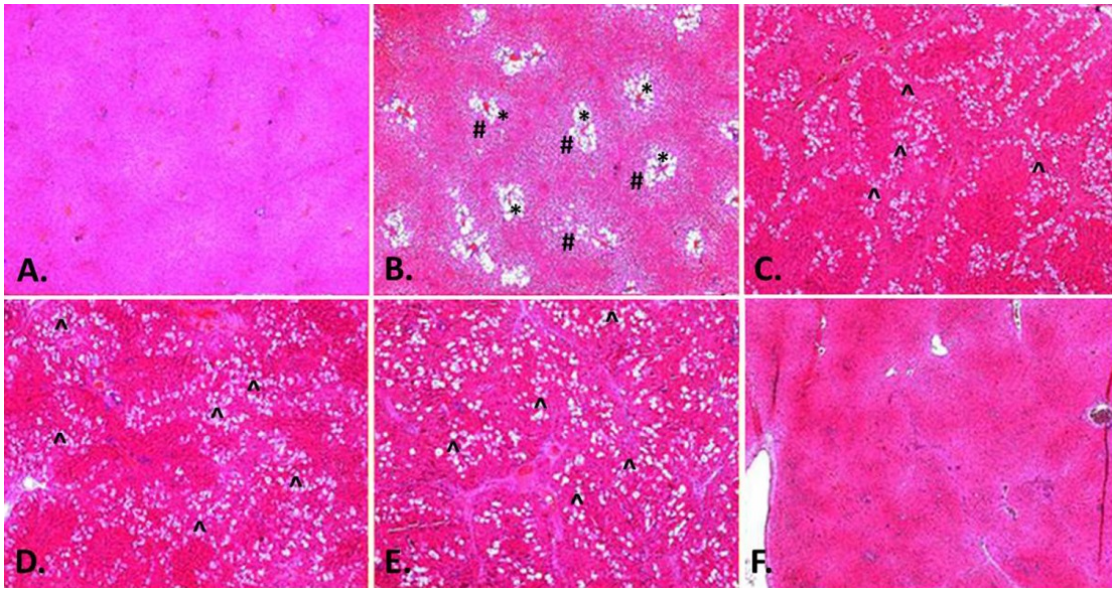

*Figure 4.7: H&E staining of rat liver tissue at different time phase. A: control rats, no abnormality in parenchymal architecture; B: At day two after CCl4 insult, infiltration of inflammatory cells, intracellular deposition of fat vacuoles and hepatocellular swelling; C: At week 2 of CCl4 insult, presence of necrotic cells; D & E: At week 4 & 6 of CCl4 insult, necrotic cells progressed with the time of CCl4 insult; F: At 4 weeks after the withdrawal of CCl4, active inflammation, fatty infiltration and necrotic cells were no longer observed. Note: * fatty inclusion, # inflammation, ^ necrosis.*

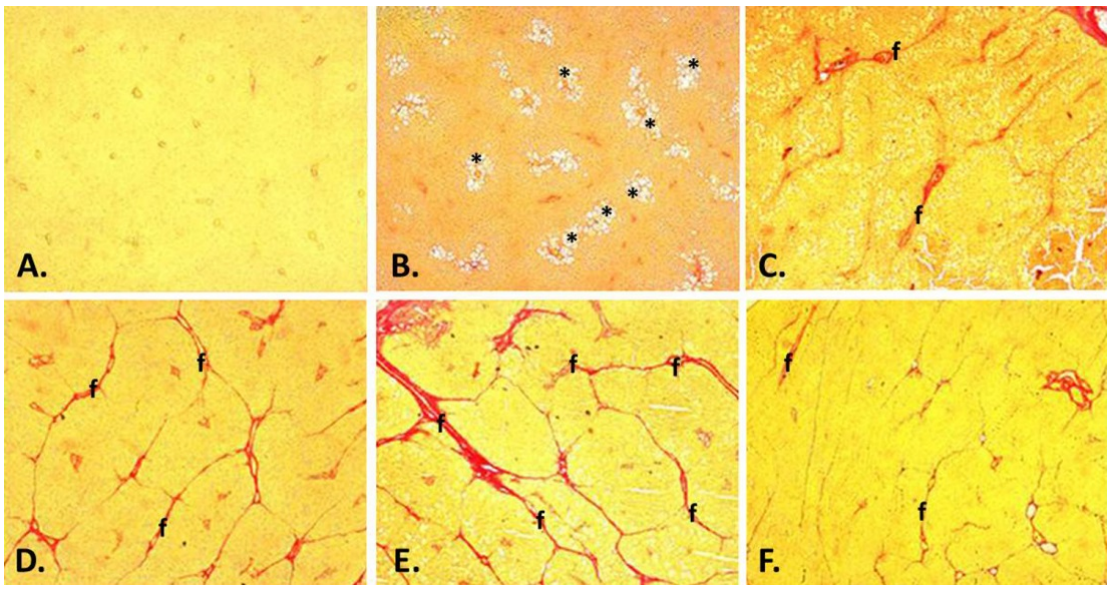

*Figure 4.8: Picrosirius-red staining of rat liver tissue at different time phase. A: control rats, no abnormality in parenchymal architecture; B: At day two after CCl4 insult, intracellular deposition of fat vacuoles, no apparent collagen deposition was observed for this time point; C: At week 2 of CCl4 insult, early fibrosis was observed, with scattered collagen deposition in the sinusoids of the peri-central lobular area without septa; D & E: At week 4 & 6 of CCl4 insult, fibrosis progressed with the time of CCl4 insult; F: At 4 weeks after the withdrawal of CCl4, mild residual fibrous bands were still present. Note: f: fibrosis, * fatty inclusion*

4.4 Discussion

A noninvasive imaging technique for detecting liver fibrosis at early stages and monitoring the disease progression or regression in response to treatment is highly desirable. Recently, a number of novel MR imaging techniques are being investigated

to identify or grade liver cirrhosis. These include double contrast-enhanced MR imaging (Aguirre et al., 2006), MR elastography (Salameh et al., 2009; Talwalkar et al., 2008), diffusion-weighted imaging (Bonekamp et al., 2009; Talwalkar et al., 2008) and diffusion tensor imaging (Cheung et al., 2010). The sensitivity of these techniques for early liver fibrosis, reproducibility and inter-site variability has not been well established (Sirlin, 2011). Other imaging methods, including ultrasonography and nuclear imaging techniques, have limited value in detecting early liver fibrosis.

T1rho MRI is sensitive to both low-frequency motional processes and static processes, and has been proposed to investigate macromolecular composition and proton exchange within tissues (Duvvuri et al., 2001; Haris et al., 2009b; Nestrasil et al., 2010b; Nguyen et al., 2008; Szyperski et al., 1993). Liver fibrosis involves the accumulation of collagen, proteoglycans and other macromolecules within the extracellular matrix; therefore it can likely be probed with MR T1rho relaxation. Using the rat liver fibrosis model induced by bile duct ligation, Wang et al. (Wang et al., 2011a) showed that T1rho MRI can be used to detect the rat liver fibrosis; the T1rho value became prolonged after bile duct ligation, and was correlated with degree of fibrosis.

In the current study, the reproducibility of repeat MR examinations was good for measurements of liver T1rho measurement and normalized liver signal intensity on

T2-weighted images.

Our histology results largely mirror the previous reports of the development of liver inflammation and fibrogenesis of this animal model (Cheung et al., 2010; Constandinou et al., 2005; Hazle et al., 1990). Compared with baseline values, 48 h after CCl4 insults there were significant increases (mean, 37%) of the relative signal intensities on T2-weighted images, likely reflecting the edema and cellular swelling associated with acute liver inflammation. While the rat liver T1rho values at baseline were similar to those previously reported (Wang et al., 2011a), the mild yet significant T1rho increase (mean, 4%) at 48 h may reflect a combination of liver tissue edema, cellular swelling and inflammatory cell infiltration. Later, as degeneration and necrosis of hepatocytes and fibrosis appeared and progressed, T1rho values further increased, and were the highest at 6 weeks post insults (Figure 4.4). On the other hand, the signal intensity on T2-weighted images reached a high value 48 h post CCl4 insult, and then did not show any further significant increase (Figure 4.6). Therefore, changes in the relative liver signal intensities on T2-weighted images and changes in the T1rho values follow different time courses during CCl4 liver fibrosis induction. The process of hepatic fibrosis is driven primarily by the development of inflammation in response to parenchymal injury (Iredale, 2007). It is possible that liver injuries such as degeneration and necrosis of hepatocytes during the experiments

might also contribute to the T1rho value increase. Four weeks post the cessation of CCl4 insult, liver T1rho was 2% (mean value) higher than the baseline and it was still statistically significant (Figure 4.4); while, with the inflammation, degeneration and necrosis of hepatocytes subdued, a mild degree of liver fibrosis was still easily visible in the rat livers (Figure 4.7F, Figure 4.8F). This slightly elevated liver T1rho at 4 weeks post the withdrawal of CCl4 accords with the residual fibrosis in the liver. The relative liver signal intensity on T2-weighted images returned to baseline values at this time point (Figure 4.6). The liver T1rho values decreased upon the withdrawal of CCl4 insult, indicating MR T1rho may be used to monitor liver injury/fibrosis regression as well as progression.

Our results also showed that the liver T1rho values of individual experimental rats dispersed at weeks 2, 4 and 6 after CCl4 insult (Figure 4.4); while liver T1rho values were more narrowly distributed at baseline and at 4 weeks post withdrawal of CCl4 insults (Figure 4.4). It has been well-documented that liver histology can vary widely in the rat fibrosis model induced by multiple CCl4 doses. This is due to an unpredictable variation in the response of the rat liver to CCl4 (Proctor and Chatamra, 1983). Our observations from week 2 to week 6 may reflect these response variations. There is a lack of reliable methods for monitoring the rapidly changing liver damage with each dose and, therefore, it is difficult to maintain a constant critical level of

liver damage. With further studies, it may be possible that MR T1rho could be used to monitor the level of liver damage for individual rats; and CCl4 liver injury rodent models may be applied when homogeneous severity is required for testing expensive premarketing drugs. In those pre-clinical settings where the killing of experimental animals is highly undesirable, liver T1rho can serve as a biomarker for liver injury (Wang and Yan, 2008). In addition to the application for liver fibrosis evaluation, T1rho imaging can also form part of multi-parametric MRI techniques as imaging biomarkers in pre-clinical animal studies for evaluation of other intra-hepatic lesions and therapeutic efficacy (Chen et al., 2006; Wang et al., 2010).

There are several limitations in this study. The findings from the current study are preliminary, given the limited sample sizes. Statistical power could be further increased with access to larger sample sizes in future studies. Though liver intoxication with CCl4 is considered a classical animal model for hepatic fibrosis, the fibrogenesis process is intertwined with edema, inflammation and hepatocyte necrosis. However, in clinical patients, liver injury and fibrogenesis are mostly intertwined. This study did not investigate the exact mechanism of T1rho increase in this CCl4 liver fibrosis model. A one-to-one correlation study of T1rho increase versus liver collagen content, by analyzing individual rats, may help to further understand the mechanism underlying the liver T1rho increase. Normalized liver signal intensities on

T2-weighted images were obtained in this study. This method could be improved by quantitative T2 mapping. Other experimental models of hepatic fibrosis, such as those associated with immunological damage and alcoholic liver disease (Constandinou et al., 2005; Tsukamoto et al., 1990), should also be tested in further studies.

4.5 Summary

In summary, this Chapter demonstrated that MR T1rho is a valuable imaging biomarker for liver injury and fibrosis induced with CCl4 chronic administration. Liver T1rho was only mildly affected by edema and acute inflammation when there was no apparent fibrosis. Liver MR T1rho values decreased when liver fibrosis and injury regressed. When there is mild residual liver fibrosis but with inflammation and hepatocytes necrosis subdued, liver T1rho remained slightly elevated, while the relative liver signal intensity on T2-weighted image returned to baseline values.

CHAPTER 5 T1RHO MRI IN LIVER OF HEALTHY HUMAN SUBJECTS

5.1 Introduction

Chronic liver disease is a major worldwide public health problem (Charlton, 2004; Davis et al., 2003; Zhou and Lu, 2009). More than 570 million individuals worldwide are chronically infected with hepatitis B virus (HBV) or hepatitis C virus (HCV) (Zhou and Lu, 2009). The trend is expected to increase due to an ageing population, the growing epidemic of obesity and nonalcoholic steatohepatitis, and the continued emergence of clinical manifestations among individuals with longstanding chronic viral hepatitis infections. Regardless of causes, chronic liver injury is generally associated with the accumulation of collagen and other macromolecules within the extracellular matrix, a process referred to as fibrosis (Wallace et al., 2008).

Liver fibrosis was considered to be irreversible originally; however there is increasing evidence that liver fibrosis is a dynamic process with potential for regression (Arthur, 2002; Veldhuijzen et al., 2010; Wallace et al., 2008; Wanless et al., 2000). Promising new treatments for liver fibrosis are currently under intensive investigation (Asadullah et al., 2003; Friedman, 2008; Hammel et al., 2001; Huang et al., 2006; Oh et al., 2008). Therefore, early detection of liver fibrosis may be helpful

in the management of chronic liver disease.

While the majority of complications from chronic liver disease results from progressive hepatic fibrosis, the available diagnostic tests used in clinical practice are not sensitive or specific enough to detect occult liver injury at early or intermediate stages (Afdhal and Nunes, 2004; Talwalkar et al., 2008). The conventional standard for the diagnosing and staging liver fibrosis is percutaneous liver biopsy. However, liver biopsy is an invasive and expensive procedure with possible side complications (Janes and Lindor, 1993). Histological assessment of fibrosis is also an inherently subjective process and is subject to sampling variability. A study that compared laparoscopic versus histological diagnosis of cirrhosis found that 32% of cases were underdiagnosed with histological examination of a single liver biopsy specimen (Poniachik et al., 1996). And a number of studies have demonstrated that excessive rates of sampling error (25–40%) result in poor reproducibility regardless of the underlying liver disease origin (Ratziu et al., 2005). In addition, the extent of variation from observer interpretation by expert histopathologists may be as high as 20% (Bravo et al., 2001). These limitations make liver biopsy unsuitable for diagnosis and longitudinal monitoring in the general population.

As reported, T1rho MRI is able to detect liver fibrosis in rat model induced by biliary duct ligation, and the degree of fibrosis is correlated with the degree of

elevation of the T1rho measurement (Wang et al., 2011a). In Chapter 4, we also reported T1rho MRI can be used to assess liver fibrosis in rat model induced by CCl4 intoxication of 1ml/kg twice weekly. The rat T1rho value increased over the baseline value by 12%, 16.5%, and 23.0% at week 2, week 4, and week 6 after first injection of CCl4. While at week 4 after the withdrawal of CCl4 insult, liver T1rho value decreased to close to the baseline value.

These results suggest liver T1rho MRI may play an important role for liver fibrosis early detection and grading. For translating liver T1rho MRI to a clinically applicable imaging biomarker, the technical feasibility of T1rho MRI for human liver needs to be evaluated.

The purpose of study described in this Chapter is four fold: 1) to evaluate the measurement reproducibility of T1rho values for healthy human liver; 2) to evaluate the T1rho value agreement of the fasting status with the post meal status; 3) to evaluate the feasibility of using less T1rho-weighted images at different spin-lock time points for human liver T1rho map; 4) to get normal liver T1rho value range of healthy human subjects

5.2 Methods

5.2.1 Subjects

All volunteers were recruited from an advertisement in our university. All subjects were clinically healthy, with no liver disease history or alcoholism. After the MRI examination, the subjects were followed up by telephone for 3 months and confirmed they remained healthy. In total, 20 subjects took part in this study, comprising 12 males and 8 females, with a mean age of 29.8 years (range: 20–44 years). Subjects were asked to undergo MRI 2 h after their standard evening meal, and/or early in the morning before taking breakfast (fasting status), depending on their availability.

5.2.2 MR Image Acquisition

MRI data acquisition was performed on a 3 T clinical scanner (Achieva; Philips Healthcare, Best, Netherlands). An 8-channel cardiac coil was used as the signal receiver to cover the liver, and the built-in body coil was used as the signal transmitter. Subjects were examined supine.

5.2.2.1 T2-weighted MRI

Anatomical imaging protocol was axial breath-hold T2 weighted spectral adiabatic inversion recovery (SPAIR) sequence (repetition time, TR=1236ms; echo time, TE=70ms; matrix=300×170; voxel size= 1×1.4×7mm^3; 20 slices; section thickness= 7 mm; intersection gap=2mm; number of signal averages, NSA=2). The scan time of conventional T2 weighted image was 24 seconds.

5.2.2.2 T1rho MRI

After inspection of the anatomical images revealed no imaging abnormalities, with scout scans in the coronal plane and sagittal plane, three representative axial slices were selected to cut through the upper, middle and lower liver for T1rho imaging (Figure 5.1). Volume shimming was employed to minimize B_0 inhomogeneities.

The diagram of sequence for T1rho MRI is given in Figure 5.2. The rotary echo spin-lock pulse was implemented in a single shot 2D balanced fast field echo (b-FFE) sequence. Spin-lock frequency was set as 500Hz and spin-lock times of 1, 10, 20, 30, 40 and 50ms were used for T1rho mapping. Segmented normal phase alternating FFE readout was used for acquisition. T1rho weighted images were acquired during the transient status towards the steady state, but with T1rho weighted magnetisation maintained. A rotary echo spin-lock pulse was applied once for every segment length of 60 readouts. A delay time of 6000ms was inserted after each segment acquisition to fully restore the equilibrium magnetization prior to the next T1rho preparation. TE and TR for b-FFE acquisition were 1.16 and 2.3ms, respectively. The voxel size was $1.5\times1.5\times7.00mm^3$. The flip angle was 40 degree and the number of signal averages (NSA) was 2. A sensitivity-encoding (SENSE) factor of 1.5 was applied for parallel imaging to reduce the phase-encoding steps, and hence the acquisition time. The whole body specific absorption rate (SAR) was < 0.4W/kg for this sequence as

demonstrated on the scanner's console.

The images were acquired with a breath-hold technique. Volunteers were trained to breath-hold during shallow breathing, and maintain breath-holding at a similar breathing depth. At each slice level, T1rho images of each spin-lock time were inspected immediately after acquisition, images with artifacts or a breath-holding position shift were discarded and these images were reacquired. The scan time was 38 s per spin-lock time point, including 30 seconds preparation time, primarily for the spin-lock pulse calibration, in which the period of time the subjects were allowed for free-breathing; and the subsequent 8 seconds for data acquisition, in which the period of time the breath was held. Including the time for rescanning, the whole examination lasted about 15 minutes.

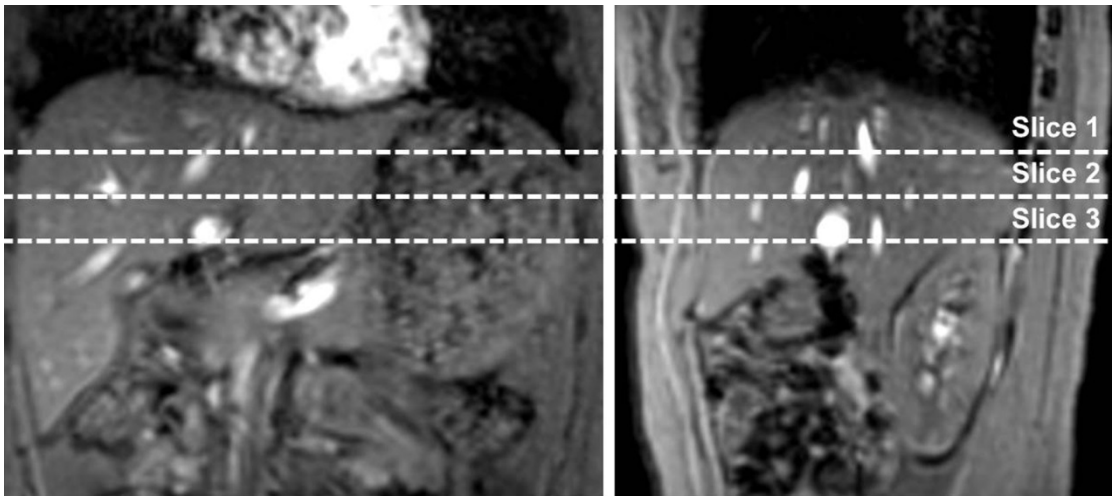

Figure 5.1: Coronal (left) and sagittal (right) scout images. Three axial slices are selected to cut though the upper (slice 1), middle (slice 2) and lower (slice 3) liver.

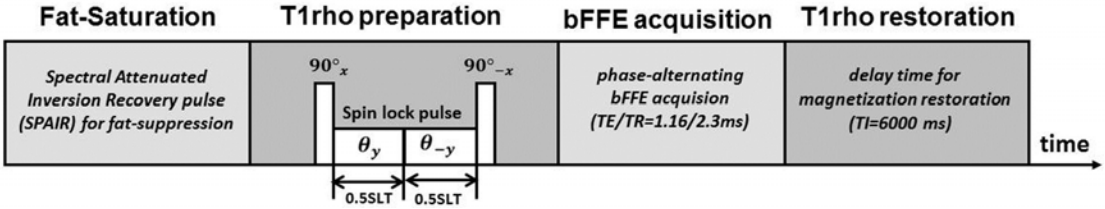

Figure 5.2: Diagram of the sequence for T1rho MRI, which is the spin-lock balanced fast field echo (b-FFE) imaging sequence for T1rho MRI, the rotary echo spin-lock pulse cluster is used for T1rho preparation. SLT= time of spin-lock.

5.2.3 T1rho Data Processing

T1rho maps were computed on a pixel-by-pixel basis using a mono-exponential decay model with a homemade Matlab program (Mathworks, Natick, MA):

$$\mathrm{M(SLT)} = \mathrm{M_0} \cdot \exp^{(-\mathrm{SLT/T1rho})} \quad \text{Equation [1.4]}$$

Where M_0 and M (SLT) denote the equilibrium magnetisation and T1rho-prepared magnetisation with the spin-lock time of SLT, respectively. This mono-exponential equation was linearised by logarithm and T1rho maps were generated by fitting all pixel intensity data as a function of SLT using linear regression. T1rho was calculated as -1/slope of the straight line fit.

T1rho maps were constructed using all 6 SLT points (1, 10, 20, 30, 40, and 50ms), 3 SLT points (1, 20, and 50ms), and 2 SLT points (1 and 50ms). Maps of coefficient of determination (R^2) were also generated for the evaluation of goodness of fit. Only T1rho values for pixels associated with R^2>0.80 were included in the subsequent

region of interest (ROI) placement and T1rho analysis to eliminate the unreliable poorly fitted T1rho values due to the blood vessel contamination with fresh blood inflow, as well as respiration-induced artifacts.

5.2.4 T1rho Measurement

The data were measured by two radiology trainees (ZF, DM) with more than 3 years of experience of reading abdominal MRIs. To quantify liver T1rho value, five ROIs of approximately 100–200mm^2 were manually placed on the liver parenchyma region of each slice's T1rho maps with R^2>0.80, excluding observable artifacts and blood vessels (Figure 5.3), leading to a total of 15 ROIs from each liver examination. The mean value of these 15 ROIs was regarded as the liver T1rho value for the subject.

Ten data sets (five from fasting status and another five from post-meal status) were used to assess inter-reader reproducibility. For this, the data were assessed by two readers independently. After the confirmation of satisfactory inter-reader reproducibility, the remaining data were measured by one trainee only (ZF), and the results by this trainee were used for further analysis and processing.

Data are presented as mean ± standard deviation. Reproducibility was assessed using intraclass correlation coefficient (ICC) on absolute agreement. According to

Fleiss (Fleiss, 1986), an ICC value of <0.4 represents poor agreement, a value >0.75 represents good agreement and a value between 0.4 and 0.75 represents fair to moderate agreement. Comparison of liver T1rho value at fasting status and post-meal status was carried out with Mann–Whitney U-test. All statistical analyses were done using SPSS v. 14.0 (SPSS, Chicago, IL). A p-value <0.05 was considered statistically significant.

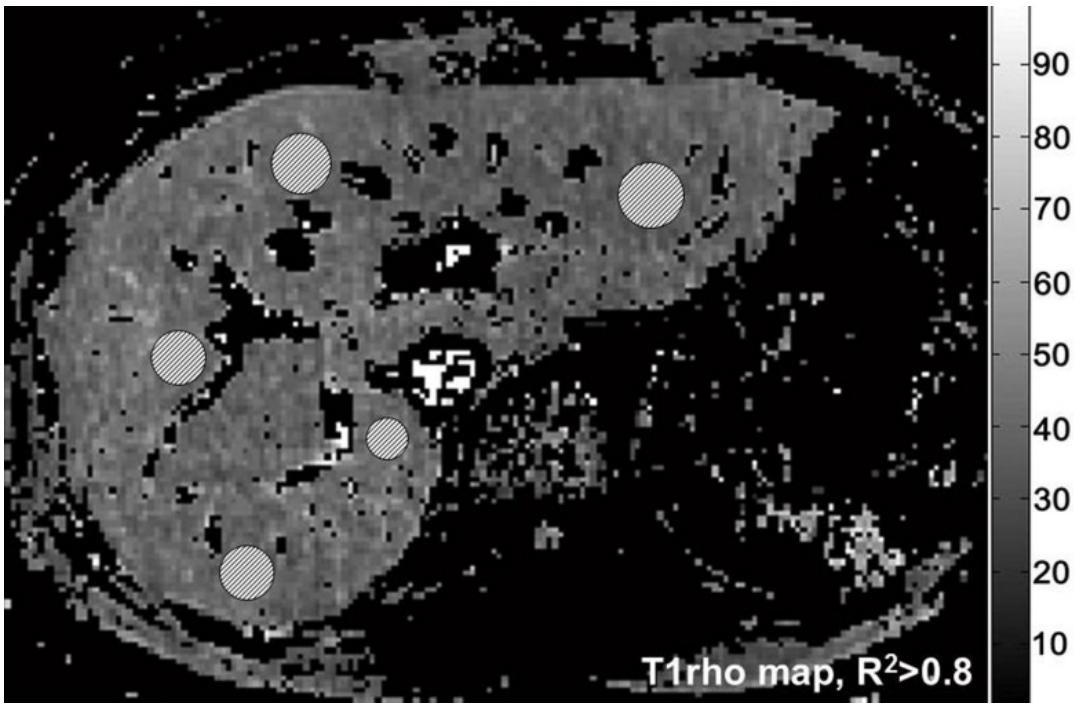

Figure 5.3: One healthy volunteer's T1rho map constructed with 6-SLT, with coefficient of determination R^2>0.8 evaluation. Five regions of interest (ROIs) are placed on the liver parenchyma region, excluding observable artifacts and blood vessels.

5.3 Results

The liver T1rho values of these 38 examinations measured from T1rho maps constructed using 6-SLT, 3-SLT, and 2-SLT points are listed in Table 5.1. The T1rho-weighted images acquired at different SLT, and T1rho maps constructed using 6-SLT, 3-SLT, and 2-SLT points are shown in Figure 5.4, and Figure 5.5, respectively.

Table 5.1: Liver T1rho values of healthy volunteer measured with 6, 3, and 2 spin-lock time (SLT) points.

Case No.	Liver T1rho values (Millisecond)											
	Scan1-fasting (n=11)			Scan 2-fasting (n=3)			Scan 1- post meal (n=15)			Scan 2- post meal (n=9)		
	SLT=6	SLT =3	SLT =2	SLT=6	SLT=3	SLT=2	SLT=6	SLT=3	SLT=2	SLT=6	SLT=3	SLT=2
1	44.8	45.1	46.9	45.8	46.3	47.4	42.8	43.5	43.8	43.4	42.6	43.7
2	41.3	41.1	43.4	41.2	41.7	43.8	39.7	39.8	40.5	38.8	38.6	39.2
3	43.6	44.2	45.2				42.5	43.2	43.9			
4							45.1	45.9	46.7	44.8	45.1	42.8
5	42.1	42.7	44.1				41.9	41.7	42.1	41.8	41.7	42.7
6	42.5	42.7	43.3				39.9	40.6	41.5			
7	43.5	44.1	45.2									
8							41.2	41.3	41.4	41	42	43.8
9							44.8	44.8	46.5	42.7	42.5	43.9
10	41.8	41.5	41.5									
11							42.9	44.1	45.7			
12	42.2	42.5	43.8				43.5	43.8	46.1	46.5	46.6	47.2
13							44.1	43.3	44.5			
14							44.3	44.8	46.8			
15							42.8	42.8	43.5			
16							41.8	42.7	43.7	41.3	42.3	42.3
17							42	42.8	43.4	42.9	43.1	43.4
18	42.3	42.8	44.1	42.1	42.5	43.9						
19	40.7	40.9	43.5									
20	39.8	40.6	42.9									
Mean	**42.2**	**42.6**	**44.0**	**43.0**	**43.5**	**45.0**	**42.6**	**43.0**	**44.0**	**42.6**	**42.7**	**43.2**
SD	**1.4**	**1.5**	**1.4**	**2.4**	**2.5**	**2.1**	**1.6**	**1.6**	**2.0**	**2.2**	**2.2**	**2.1**

Note: SLT =spin-lock time; SD= standard deviation;

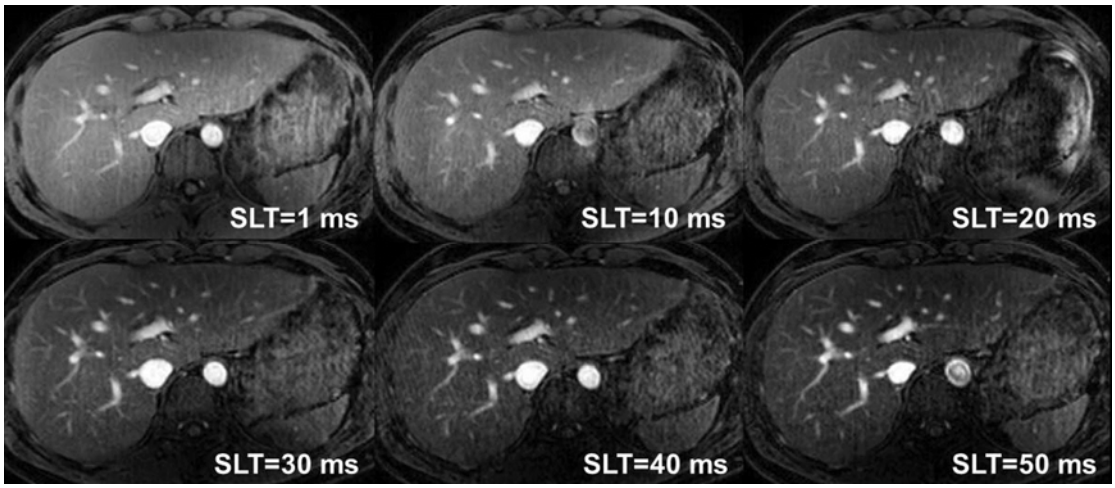

Figure 5.4: The T1rho-weighted images acquired with different spin-lock time (SLT) ranging from 1 to 50ms.

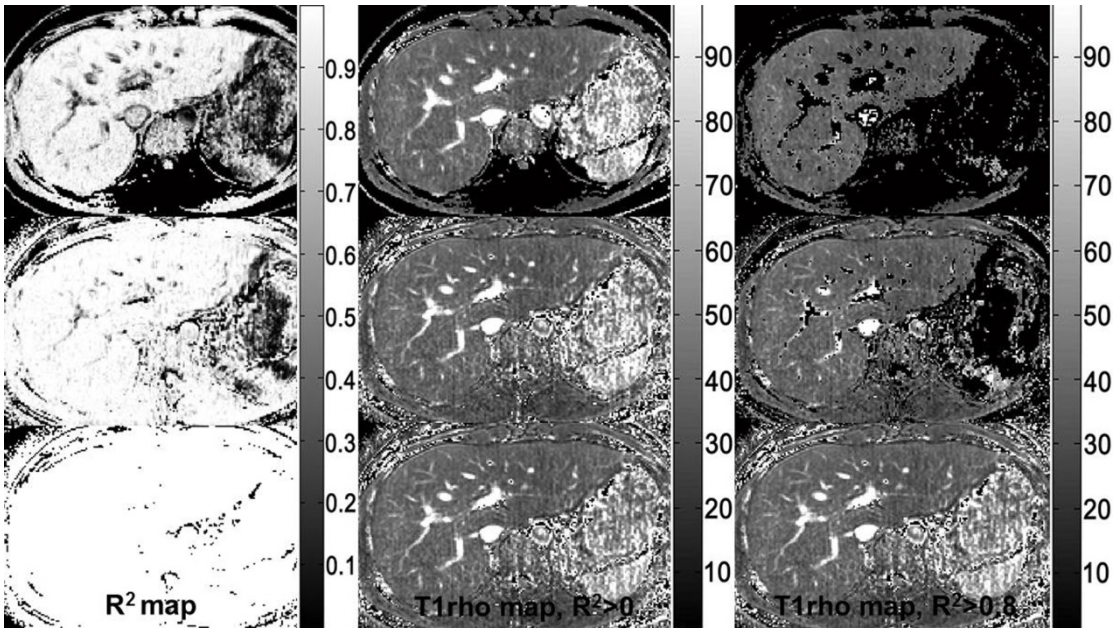

Figure 5.5: One healthy volunteer's T1rho maps constructed using 6-SLT (upper row), 3-SLT (middle row), and 2-SLT (lower row). Left column: coefficient of determination (R^2) maps, middle column: T1rho maps without R^2 evaluation, right column: T1rho maps with R^2>0.8 evaluation. When SLT point decrease, R^2 evaluation is less efficient to remove blood vessel contamination and artifact. When SLT point is 2, the R^2 is

always equal to one, so no pixels are excluded by criteria of R^2>0.8.

5.3.1 T1rho Measurement Reproducibility

The first 10 scans data set (5 from fasting status, 5 from post-meal status) were used to assess inter-reader measurement reproducibility. The ICCs for inter-reader measurement reproducibility were 0.930, 0.981, and 0.969 for T1rho maps constructed by 6-SLT, 3-SLT and 2-SLT, respectively, indicating the T1rho measurement had good reproducibility between the two readers.

12 subjects were scanned twice (3 at fasting status and 9 at post-meal status); the ICCs for scan-rescan reproducibility were 0.811, 0.804, and 0.69 for 6-SLT, 3-SLT and 2-SLT used for T1rho mapping, respectively; it indicated T1rho MRI using 6 or 3 SLT points had good scan-rescan reproducibility, while T1rho MRI using only 2 SLT points had moderate scan-rescan reproducibility.

5.3.2 T1rho Value Agreement of the Fasting Status with Post Meal Status

A comparison was made to see whether there was a difference in the liver T1rho value at fasting status and at post meal status. For those scanned twice, only the data from the first scan were used, resulting 11 values from fasting status and 15 post meal status. Liver T1rho values measured from the T1rho maps constructed by 6-SLT, 3-SLT, and 2-SLT is given in the Table 5.2. There was no significant difference in the

liver T1rho value at fasting status and at post meal status.

Table 5.2: Comparison of liver T1rho values at fasting status and at post meal status.

SLT points for T1rho Mapping	Liver T1rho Values (Millisecond)		p-value#
	fasting status (n=11)	post meal status (n=15)	
6-SLT points	42.2±1.4	42.6±1.6	p=0.483
3-SLT points	42.6±1.5	43.0±1.6	p=0.363
2-SLT points	44.0±1.4	44.0±2.0	p=0.938

Note: 6-SLT points: 1, 10, 20, 30, 40 and 50ms; 3-SLT point: 1, 20 and 50ms; 2-SLT points: 1 and 50ms. #: Mann–Whitney U-test.

5.3.3 T1rho Value Agreement for T1rho Maps Constructed by Different Spin-lock Time Points

Polled all 38 examinations together, the ICC for 3-SLT T1rho measurement v.s. 6-SLT T1rho measurement was 0.949, while ICC for 2-SLT T1rho measurement v.s. 6-SLT T1rho measurement was only 0.652. The Bland and Altman plots for the comparison are given in Figure 5.6, with the mean difference of 0.32 (95% limits of agreement:-0.6, 1.23) for 3-SLT v.s. 6-SLT T1rho measurement, and the mean difference of 1.37 (95% limits of agreement: -0.64, 3.37) for 2-SLT v.s. 6-SLT T1rho measurement. These results suggest the T1rho measurement from the T1rho map constructed by 3 SLT points had a good agreement with 6 SLT points. These results indicate that using 3-SLT of 1, 20 and 50ms can be acceptable alternative for the liver

T1rho measurement, while 2-SLT of 1 and 50ms do not provide reliable measurement.

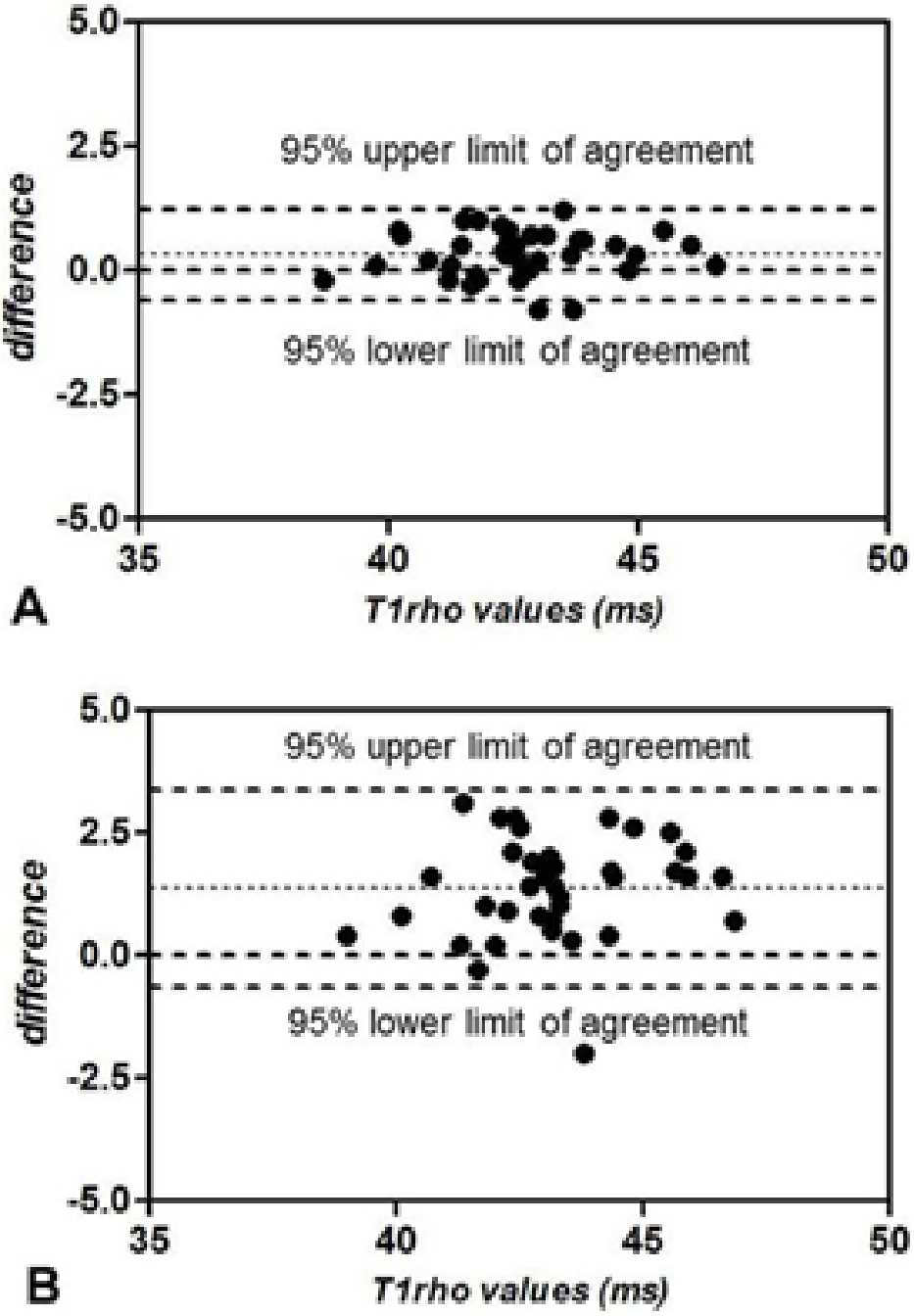

Figure 5.6: Bland and Altman plots for comparison of 3-SLT v.s. 6-SLT liver T1rho measurement (A) and 2-SLT v.s. 6-SLT liver T1rho measurement (B). 3-SLT measurement demonstrates good agreement with 6-SLT measurement. SLT= spin-lock time.

5.3.4 T1rho Value Range of Healthy Human Subjects

Polled all 38 examinations together, the measured liver T1rho value was 42.5±1.7ms (range: 38.8-46.5ms) for 6-SLT, 42.9±1.8ms (range: 38.6-46.6ms) for 3-SLT, and 43.9±1.9ms (range: 39.2-47.4ms) for 2-SLT. There was no significant difference between the measured liver T1rho values using 6-SLT and 3-SLT for T1rho mapping ($p=0.442$), while the T1rho value difference between 6-SLT and 2-SLT used for T1rho mapping was significant ($p<0.001$)

5.4 Discussion

In patients with pre-cirrhotic stages of liver fibrosis, as well as patients with early cirrhosis, the liver parenchyma usually has a normal appearance, or may exhibit only subtle, non-specific heterogeneity on conventional MRI. Recently, a number of novel MRI techniques have been investigated to identify or grade liver cirrhosis. These include double contrast-enhanced MRI (Aguirre et al., 2006), MR elastography (Salameh et al., 2009; Talwalkar et al., 2008) and diffusion-weighted imaging (Bonekamp et al., 2009; Talwalkar et al., 2008). These techniques' sensitivity for early liver fibrosis, reproducibility and intersite variability have not been well

established (Sirlin, 2011). Other imaging methods, including ultrasound and nuclear imaging techniques, have limited value in detecting early liver fibrosis.

T1rho MRI, as a new mechanism for MR tissue contrast, has been investigated in biomedical applications. Liver fibrosis involves the accumulation of collagen, proteoglycans and other macromolecules. T1rho MRI is able to detect liver fibrosis in rat model induced by biliary duct ligation (Wang et al., 2011a) and CCl4 insult (in Chapter). It is plausible that T1rho MRI may be sensitive for evaluation of liver fibrosis in patients.

Clinically, the technical difficulties of T1rho MRI include its relatively slow acquisition speed, sensitivity to B_0 and B_1 field inhomogeneities and high SAR. A rotary echo pulse was applied in this study to compensate the B_1 inhomogeneities (Charagundla et al., 2003). Volume shimming was also employed to minimize the B_0 inhomogeneities. In all T1rho scans in this study, SAR deposition was under the allowable Food and Drug Administration limits of 0.4W/kg averaged over the whole body (Collins et al., 1998). Owing to respiratory motion, liver imaging represents a particular challenge for this technique. In our initial pilot studies, three-dimensional (3D) b-FFE sequence and respiratory gating was used to increase liver coverage; however, the upper and lower sections of the scan block tended to have poor image quality, probably due to B_1 field inhomogeneity. Importantly, it was observed that

even the use of respiratory gating might not completely eliminate the respiration-induced displacement of images acquired at each spin-lock time. Meanwhile, liver vessels displayed high signal intensities with the use of b-FFE sequence (Figure 5.4). Thus, even mild spatial misregistration due to respiratory motion could lead to an artificially high T1rho value for liver parenchyma. As such, the criterion of R^2>0.80 was applied to eliminate the unreliable artificially high T1rho values induced by the vessel contamination, as well as respiration-induced artifacts.

In this study, T1rho measurement had good reproducibility between the two readers and two scans. It is known that the liver would have a higher level of glycogen post meal than at fast status. Our current study suggests that this glycogen level fluctuation does not affect liver T1rho level measurement.

Accurate and precise T1rho mapping is challenging under the scan time constraint because multiple SLTs are usually required, and a long delay time (6000ms in this study) is also often necessary in the spin-lock pulse sequence for the longitudinal magnetization restoration. The reduction of the applied SLT numbers is an apparent strategy to enhance T1rho imaging efficiency, as long as the accuracy and reliability of T1rho mapping could be maintained. In clinical practice, it will be always advantageous if accurate liver T1rho value measurement can be obtained with fewer SLTs, particularly for patients who experience difficulties in holding their breath. In

addition, a high frequency spin-lock pulse is usually associated with high SAR and total RF energy deposition, which may be a safety concern for T1rho MR imaging, particularly at high fields, such as 3T (Santyr et al., 1994). Examinations with fewer SLTs are also helpful to reduce the total RF energy deposition into the patient bodies, and mitigating the safety concern.

When fewer SLTs are used for T1rho imaging, careful selection of the applied SLTs is important to optimize the accuracy of the T1rho maps. If the applied SLTs are all much shorter than the true T1rho value of the target tissue, big fitting deviation of T1rho values can be introduced. On the other hand, much longer SLTs than the true T1rho value would result in images with very low SNRs, and hence reduce the fitting accuracy. The SLT of 1ms was selected, in this study, as the T1rho-weighted image acquired at this SLT has the highest SNR. Theoretical analysis has shown that the highest precision of exponential decay constant fitting could be achieved if the second data point is measured around the true value of the exponential decay constant (Fleysher et al., 2008). Therefore, The SLT of 50ms was selected because it was close to and slightly larger than the true T1rho value of human livers at 3T. Actually, by using two SLTs, T1rho and M_0 could be explicitly solved from the mono-exponential equation with the R^2 always equal to one. An additional SLT of 20ms was included in the 3-SLT fitting to increase the degree of freedom for fitting, and thus, improve the

robustness of T1rho mapping. Note that the selection of the third data point, 20ms in this study, for fitting will be relatively robust, i.e. T1rho fitting accuracy and uncertainty, would not change much if the third data point is selected, as the other values like 30ms or 40ms. In the current study, with three slices acquired with 6 SLTs, 3 SLTs, or 2 SLTs, 11.4 minutes, 5.7 minutes or 3.8 minutes were required, respectively. In addition, some resting time is allowed after each breath-holding. By using 3-SLT approach, the T1rho imaging scan time for the liver could be reduced approximately by a factor of two, compared to an acquisition using six SLTs.

After comparing the agreement of 3-SLT vs. 6-SLT measurement, and 2-SLT vs. 6-SLT measurement, all the MRI data, including fasting status and post-meal status, were used for comparison. The ICC for 3-SLT v.s. 6-SLT measurement and 2-SLT v.s. 6-SLT measurement were satisfactory, according to Fleiss (Fleiss, 1986), though as expected, the ICC for 3-SLT v.s. 6-SLT agreement (0.949) was better than 2-SLT v.s. 6-SLT agreement (0.652). In addition, the ICC for scan-rescan reproducibility was comparable with 6-SLT and 3-SLT measurements (0.811 and 0.804 respectively), while it was less optimal for 2-SLT measurement (0.69). The measured healthy human liver T1rho value in this study is similar with the control rat liver T1rho values reported in Chapter 4 and reported article (Wang et al., 2011d).

One limitation of the current study is that only healthy volunteers were studied, and

whether the results from this study can directly be translated to application in patients with liver diseases remain to be further investigated.

5.5 Summary

In summary, it is feasible to obtain consistent liver T1rho measurement for human subjects at 3 T. Our study demonstrated that the ICCs for inter-reader measurement reproducibility and scan-rescan reproducibility were good for human liver T1rho measurement; the liver T1rho value did not affected by glycogen level fluctuation; adopting 3-SLT of 1, 20, and 50ms for T1rho measurement could provide reliable measurement and reduce the scanning time approximately by a factor of two, compared to an acquisition using 6-SLT of 1, 10, 20, 30, 40, and 50ms, it might be an acceptable alternative when fast acquisition is desired for the liver T1rho imaging. These preliminary results will be relevant for translating liver MRI T1rho to a clinically applicable imaging biomarker for liver fibrosis.

CHAPTER 6 GENERAL DISCUSSION AND FURTHER WORK

T1rho MRI provides us a new contrast mechanism that is different from T1- and T2-weighted contrast. T1rho MRI can be performed in the forms of T1rho-weighted image, T1rho mapping and T1rho dispersion. T1rho MRI is useful to study low-frequency motional processes and chemical exchange in biological tissues.

In this dissertation, several applications of quantitative T1rho mapping were investigated; including T1rho mapping in neuro-degeneration induced by normal aging processing and chronic hypertension in rats, T1rho mapping in disc degeneration in human subjects, T1rho mapping in liver injury and fibrosis model induced by CCl4 insult, and T1rho mapping in normal liver in healthy human subjects.

In our study described in Chapter 2, the exact mechanism of T1rho value increase in rats with aging processing and chronic hypertension was not yet well investigated. Further histological and biochemical correlation study should be conducted to further understand the mechanism underlying the rat brain T1rho value increase. In our study described in Chapter 3, the relative performance of T1rho and T2 for disc

degeneration evaluation was compared. The correlation between T1rho and T2 values and clinical symptoms, particularly the duration of low-back pain, of the patients should be further investigated. In our study described in Chapter 4, the exact mechanism of T1rho increase in this CCl4 liver fibrosis model was not well investigated. Further one-to-one correlation study of T1rho increase versus liver collagen content, by analyzing individual rats, may help to further understand the mechanism underlying the liver T1rho value increase. Additionally, in order to further understand the T1rho MRI in liver fibrosis, other experimental models of hepatic fibrosis, such as those associated with immunological damage and alcoholic liver disease should also be tested in further studies. In our study described in Chapter 5, clinical potential of T1rho MRI in the management of human liver have been demonstrated. Further studies are encouraged to realize the ultimate clinical application of T1rho MRI in the patients with liver fibrosis or cirrhosis.

In our studies described in this thesis, we quantified the T1rho values by setting ROIs in rat brain, intervertebral disc, and liver parenchyma region of each slice's T1rho maps. Manual ROI analysis of T1rho map is a relatively time-consuming method. An efficient and reliable T1rho measurement method, such as histogram analysis method, should be further investigated.

T1rho MRI, particularly at low spin-lock frequency, is sensitive to B_0 and B_1

inhomogeneities. In our studies described in this thesis, volume shimming was employed to minimize B_0 inhomogeneities. The rotary echo spin-lock pulse ("self-compensating" spin-lock pulse) is introduced to reduce the potential image artifacts arising from B_1 inhomogeneity. However, in our study described in Chapter 5, the human liver T1rho images still tend to present the banding-like spin-lock artifacts induced by B_0 inhomogeneities; the percentage of satisfactory images per acquisition was about 60%. The method described by Dixon et al. (Dixon et al., 1996) has been proposed to reduce sensitivity to B_0 field inhomogeneity in T1rho imaging. Therefore, the pulse modified according to Dixon method should be further evaluated.

Chemical exchange (CE), usually represented by proton exchange, is thought to play a crucial role in T1rho dispersion. It is worth noting that chemical exchange has been recently exploited as a novel and powerful contrast mechanism for MRI, usually performed in the forms of either T1rho dispersion imaging or chemical exchange saturation transfer (CEST) imaging (Ward et al., 2000; van Zijl and Yadav, 2011). Therefore, T1rho dispersion and the combination with CEST imaging are worth to be conducted in the further to better characterize and understand the underlying chemical exchange processes associated with physiology and pathology.

REFERENCES:

Adams, M.A., Roughley, P.J., 2006. What is intervertebral disc degeneration, and what causes it? Spine (Phila Pa 1976) 31, 2151-2161.

Afdhal, N.H., Nunes, D., 2004. Evaluation of liver fibrosis: a concise review. American Journal Of Gastroenterology 99, 1160-1174.

Aguirre, D.A., Behling, C.A., Alpert, E., Hassanein, T.I., Sirlin, C.B., 2006. Liver fibrosis: noninvasive diagnosis with double contrast material-enhanced MR imaging. Radiology 239, 425-437.

Akella, S.V., Regatte, R.R., Gougoutas, A.J., Borthakur, A., Shapiro, E.M., Kneeland, J.B., Leigh, J.S., Reddy, R., 2001. Proteoglycan-induced changes in T1rho-relaxation of articular cartilage at 4T. Magn Reson Med 46, 419-423.

Amenta, F., Tayebati, S.K., Tomassoni, D., 2010. Spontaneously hypertensive rat neuroanatomy: applications to pharmacological research. Ital J Anat Embryol 115, 13-17.

Antoniou, J., Steffen, T., Nelson, F., Winterbottom, N., Hollander, A.P., Poole, R.A., Aebi, M., Alini, M., 1996. The human lumbar intervertebral disc: evidence for changes in the biosynthesis and denaturation of the extracellular matrix with growth, maturation, ageing, and degeneration. Journal Of Clinical

Investigation 98, 996-1003.

Aronen, H.J., Ramadan, U.A., Peltonen, T.K., Markkola, A.T., Tanttu, J.I., Jaaskelainen, J., Hakkinen, A.M., Sepponen, R., 1999. 3D spin-lock imaging of human gliomas. Magnetic Resonance Imaging 17, 1001-1010.

Arthur, M.J., 2002. Reversibility of liver fibrosis and cirrhosis following treatment for hepatitis C. Gastroenterology 122, 1525-1528.

Asadullah, K., Sterry, W., Volk, H.D., 2003. Interleukin-10 therapy--review of a new approach. Pharmacological Reviews 55, 241-269.

Auerbach, J.D., Johannessen, W., Borthakur, A., Wheaton, A.J., Dolinskas, C.A., Balderston, R.A., Reddy, R., Elliott, D.M., 2006. In vivo quantification of human lumbar disc degeneration using T(1rho)-weighted magnetic resonance imaging. European Spine Journal 15 Suppl 3, S338-S344.

Bendel, P., Eilam, R., 1992. Quantitation of ventricular size in normal and spontaneously hypertensive rats by magnetic resonance imaging. Brain Research 574, 224-228.

Blumenkrantz, G., Li, X., Han, E.T., Newitt, D.C., Crane, J.C., Link, T.M., Majumdar, S., 2006. A feasibility study of in vivo T1rho imaging of the intervertebral disc. Magnetic Resonance Imaging 24, 1001-1007.

Blumenkrantz, G., Zuo, J., Li, X., Kornak, J., Link, T.M., Majumdar, S., 2010. In vivo

3.0-tesla magnetic resonance T1rho and T2 relaxation mapping in subjects with intervertebral disc degeneration and clinical symptoms. Magn Reson Med 63, 1193-1200.

Bonekamp, S., Kamel, I., Solga, S., Clark, J., 2009. Can imaging modalities diagnose and stage hepatic fibrosis and cirrhosis accurately? Journal Of Hepatology 50, 17-35.

Borenstein, D.G., O'Mara, J.J., Boden, S.D., Lauerman, W.C., Jacobson, A., Platenberg, C., Schellinger, D., Wiesel, S.W., 2001. The value of magnetic resonance imaging of the lumbar spine to predict low-back pain in asymptomatic subjects : a seven-year follow-up study. Journal Of Bone And Joint Surgery-American Volume 83-A, 1306-1311.

Borthakur, A., Gur, T., Wheaton, A.J., Corbo, M., Trojanowski, J.Q., Lee, V.M., Reddy, R., 2006. In vivo measurement of plaque burden in a mouse model of Alzheimer's disease. Journal Of Magnetic Resonance Imaging 24, 1011-1017.

Borthakur, A., Maurer, P.M., Fenty, M., Wang, C., Berger, R., Yoder, J., Balderston, R.A., Elliott, D.M., 2011. T1rho magnetic resonance imaging and discography pressure as novel biomarkers for disc degeneration and low back pain. Spine (Phila Pa 1976) 36, 2190-2196.

Borthakur, A., Sochor, M., Davatzikos, C., Trojanowski, J.Q., Clark, C.M., 2008. T1rho MRI of Alzheimer's disease. Neuroimage 41, 1199-1205.

Borthakur, A., Wheaton, A.J., Gougoutas, A.J., Akella, S.V., Regatte, R.R., Charagundla, S.R., Reddy, R., 2004. In vivo measurement of T1rho dispersion in the human brain at 1.5 tesla. Journal Of Magnetic Resonance Imaging 19, 403-409.

Bravo, A.A., Sheth, S.G., Chopra, S., 2001. Liver biopsy. N Engl J Med 344, 495-500.

Carl, A., Ledet, E., Yuan, H., Sharan, A., 2004. New developments in nucleus pulposus replacement technology. Spine J 4, 325S-329S.

Cassinelli, E.H., Hall, R.A., Kang, J.D., 2001. Biochemistry of intervertebral disc degeneration and the potential for gene therapy applications. Spine J 1, 205-214.

Charagundla, S.R., Borthakur, A., Leigh, J.S., Reddy, R., 2003. Artifacts in T(1rho)-weighted imaging: correction with a self-compensating spin-locking pulse. Journal Of Magnetic Resonance 162, 113-121.

Charagundla, S.R., Stolpen, A.H., Leigh, J.S., Reddy, R., 1998. Off-resonance proton T1rho dispersion imaging of 17O-enriched tissue phantoms. Magn Reson Med 39, 588-595.

Charlton, M., 2004. Nonalcoholic fatty liver disease: a review of current understanding and future impact. Clin Gastroenterol Hepatol 2, 1048-1058.

Chen, F., Sun, X., De Keyzer, F., Yu, J., Peeters, R., Coudyzer, W., Vandecaveye, V., Landuyt, W., Bosmans, H., Van Hecke, P., Marchal, G., Ni, Y., 2006. Liver tumor model with implanted rhabdomyosarcoma in rats: MR imaging, microangiography, and histopathologic analysis. Radiology 239, 554-562.

Cheung, J.S., Fan, S.J., Gao, D.S., Chow, A.M., Man, K., Wu, E.X., 2010. Diffusion tensor imaging of liver fibrosis in an experimental model. Journal Of Magnetic Resonance Imaging 32, 1141-1148.

Chiu, E.J., Newitt, D.C., Segal, M.R., Hu, S.S., Lotz, J.C., Majumdar, S., 2001. Magnetic resonance imaging measurement of relaxation and water diffusion in the human lumbar intervertebral disc under compression in vitro. Spine (Phila Pa 1976) 26, E437-E444.

Collins, C.M., Li, S., Smith, M.B., 1998. SAR and B1 field distributions in a heterogeneous human head model within a birdcage coil. Specific energy absorption rate. Magn Reson Med 40, 847-856.

Constandinou, C., Henderson, N., Iredale, J.P., 2005. Modeling liver fibrosis in rodents. Methods Mol Med 117, 237-250.

Davis, G.L., Albright, J.E., Cook, S.F., Rosenberg, D.M., 2003. Projecting future

complications of chronic hepatitis C in the United States. Liver Transpl 9, 331-338.

Dixon, W.T., Oshinski, J.N., Trudeau, J.D., Arnold, B.C., Pettigrew, R.I., 1996. Myocardial suppression in vivo by spin locking with composite pulses. Magn Reson Med 36, 90-94.

Duvvuri, U., Goldberg, A.D., Kranz, J.K., Hoang, L., Reddy, R., Wehrli, F.W., Wand, A.J., Englander, S.W., Leigh, J.S., 2001. Water magnetic relaxation dispersion in biological systems: the contribution of proton exchange and implications for the noninvasive detection of cartilage degradation. Proc Natl Acad Sci U S A 98, 12479-12484.

Fleiss, J., 1986. Reliability of measurement: the design and analysis of clinical experiments. John Wiley & Sons, New York, NY.

Fleysher, R., Fleysher, L., Gonen, O., 2008. The optimal MR acquisition strategy for exponential decay constants estimation. Magnetic Resonance Imaging 26, 433-435.

Friedman, S.L., 2008. Hepatic fibrosis -- overview. Toxicology 254, 120-129.

Griffith, J.F., Wang, Y.X., Antonio, G.E., Choi, K.C., Yu, A., Ahuja, A.T., Leung, P.C., 2007. Modified Pfirrmann grading system for lumbar intervertebral disc degeneration. Spine (Phila Pa 1976) 32, E708-E712.

Halavaara, J.T., Sepponen, R.E., Lamminen, A.E., Vehmas, T., Bondestam, S., 1998. Spin lock and magnetization transfer MR imaging of local liver lesions. Magnetic Resonance Imaging 16, 359-364.

Hammel, P., Couvelard, A., O'Toole, D., Ratouis, A., Sauvanet, A., Flejou, J.F., Degott, C., Belghiti, J., Bernades, P., Valla, D., Ruszniewski, P., Levy, P., 2001. Regression of liver fibrosis after biliary drainage in patients with chronic pancreatitis and stenosis of the common bile duct. N Engl J Med 344, 418-423.

Haris, M., McArdle, E., Fenty, M., Singh, A., Davatzikos, C., Trojanowski, J.Q., Melhem, E.R., Clark, C.M., Borthakur, A., 2009a. Early marker for Alzheimer's disease: hippocampus T1rho (T(1rho)) estimation. Journal Of Magnetic Resonance Imaging 29, 1008-1012.

Haris, M., McArdle, E., Fenty, M., Singh, A., Davatzikos, C., Trojanowski, J.Q., Melhem, E.R., Clark, C.M., Borthakur, A., 2009b. Early marker for Alzheimer's disease: hippocampus T1rho (T(1rho)) estimation. Journal Of Magnetic Resonance Imaging 29, 1008-1012.

Haris, M., Singh, A., Cai, K., Davatzikos, C., Trojanowski, J.Q., Melhem, E.R., Clark, C.M., Borthakur, A., 2011a. T1rho (T1rho) MR imaging in Alzheimer's disease and Parkinson's disease with and without dementia. Journal Of

Neurology 258, 380-385.

Haris, M., Singh, A., Cai, K., McArdle, E., Fenty, M., Davatzikos, C., Trojanowski, J.Q., Melhem, E.R., Clark, C.M., Borthakur, A., 2011b. T(1rho) MRI in Alzheimer's disease: detection of pathological changes in medial temporal lobe. Journal Of Neuroimaging 21, e86-e90.

Hassett, G., Hart, D.J., Manek, N.J., Doyle, D.V., Spector, T.D., 2003. Risk factors for progression of lumbar spine disc degeneration: the Chingford Study. Arthritis Rheum 48, 3112-3117.

Hazle, J.D., Narayana, P.A., Dunsford, H.A., 1990. Chronic carbon tetrachloride and phospholipase D hepatotoxicity in rat: in vivo 1H magnetic resonance, total lipid analysis, and histology. Magn Reson Med 15, 211-228.

Heiland, S., Sartor, K., Martin, E., Bardenheuer, H.J., Plaschke, K., 2002. In vivo monitoring of age-related changes in rat brain using quantitative diffusion magnetic resonance imaging and magnetic resonance relaxometry. Neuroscience Letters 334, 157-160.

Huang, Y.H., Shi, M.N., Zheng, W.D., Zhang, L.J., Chen, Z.X., Wang, X.Z., 2006. Therapeutic effect of interleukin-10 on CCl4-induced hepatic fibrosis in rats. World J Gastroenterol 12, 1386-1391.

Hughes, E.J., Bond, J., Svrckova, P., Makropoulos, A., Ball, G., Sharp, D.J., Edwards,

A.D., Hajnal, J.V., Counsell, S.J., 2012. Regional changes in thalamic shape and volume with increasing age. Neuroimage 63, 1134-1142.

Hulvershorn, J., Borthakur, A., Bloy, L., Gualtieri, E.E., Reddy, R., Leigh, J.S., Elliott, M.A., 2005. T1rho contrast in functional magnetic resonance imaging. Magn Reson Med 54, 1155-1162.

Iredale, J.P., 2007. Models of liver fibrosis: exploring the dynamic nature of inflammation and repair in a solid organ. Journal Of Clinical Investigation 117, 539-548.

Janes, C.H., Lindor, K.D., 1993. Outcome of patients hospitalized for complications after outpatient liver biopsy. Annals Of Internal Medicine 118, 96-98.

Johannessen, W., Auerbach, J.D., Wheaton, A.J., Kurji, A., Borthakur, A., Reddy, R., Elliott, D.M., 2006. Assessment of human disc degeneration and proteoglycan content using T1rho-weighted magnetic resonance imaging. Spine (Phila Pa 1976) 31, 1253-1257.

Jokivarsi, K.T., Hiltunen, Y., Grohn, H., Tuunanen, P., Grohn, O.H., Kauppinen, R.A., 2010. Estimation of the onset time of cerebral ischemia using T1rho and T2 MRI in rats. Stroke 41, 2335-2340.

Kerttula, L., Kurunlahti, M., Jauhiainen, J., Koivula, A., Oikarinen, J., Tervonen, O., 2001. Apparent diffusion coefficients and T2 relaxation time measurements

to evaluate disc degeneration. A quantitative MR study of young patients with previous vertebral fracture. Acta Radiologica 42, 585-591.

Knox, C.A., Yates, R.D., Chen, I., Klara, P.M., 1980. Effects of aging on the structural and permeability characteristics of cerebrovasculature in normotensive and hypertensive strains of rats. Acta Neuropathologica 51, 1-13.

Krueger, E.C., Perry, J.O., Wu, Y., Haughton, V.M., 2007. Changes in T2 relaxation times associated with maturation of the human intervertebral disk. AJNR Am J Neuroradiol 28, 1237-1241.

Lee, T.H., Liu, H.L., Yang, S.T., Yang, J.T., Yeh, M.Y., Lin, J.R., 2011. Effects of aging and hypertension on cerebral ischemic susceptibility: evidenced by MR diffusion-perfusion study in rat. Experimental Neurology 227, 314-321.

Li, X., Han, E.T., Busse, R.F., Majumdar, S., 2008. In vivo T(1rho) mapping in cartilage using 3D magnetization-prepared angle-modulated partitioned k-space spoiled gradient echo snapshots (3D MAPSS). Magn Reson Med 59, 298-307.

Makela, H.I., Grohn, O.H., Kettunen, M.I., Kauppinen, R.A., 2001. Proton exchange as a relaxation mechanism for T1 in the rotating frame in native and immobilized protein solutions. Biochem Biophys Res Commun 289,

813-818.

Marinelli, N.L., Haughton, V.M., Munoz, A., Anderson, P.A., 2009. T2 relaxation times of intervertebral disc tissue correlated with water content and proteoglycan content. Spine (Phila Pa 1976) 34, 520-524.

Markkola, A.T., Aronen, H.J., Paavonen, T., Hopsu, E., Sipila, L.M., Tanttu, J.I., Sepponen, R.E., 1996. Spin lock and magnetization transfer imaging of head and neck tumors. Radiology 200, 369-375.

McCommis, K.S., He, X., Abendschein, D.R., Gupte, P.M., Gropler, R.J., Zheng, J., 2010. Cardiac 17O MRI: toward direct quantification of myocardial oxygen consumption. Magn Reson Med 63, 1442-1447.

Modic, M.T., Ross, J.S., 2007. Lumbar degenerative disk disease. Radiology 245, 43-61.

Muthupillai, R., Flamm, S.D., Wilson, J.M., Pettigrew, R.I., Dixon, W.T., 2004. Acute myocardial infarction: tissue characterization with T1rho-weighted MR imaging--initial experience. Radiology 232, 606-610.

Napoleone, P., Ferrante, F., Ghirardi, O., Ramacci, M.T., Amenta, F., 1990. Age-dependent nerve cell loss in the brain of Sprague-Dawley rats: effect of long term acetyl-L-carnitine treatment. Arch Gerontol Geriatr 10, 173-185.

Nestrasil, I., Michaeli, S., Liimatainen, T., Rydeen, C.E., Kotz, C.M., Nixon, J.P.,

Hanson, T., Tuite, P.J., 2010a. T1rho and T2rho MRI in the evaluation of Parkinson's disease. Journal Of Neurology 257, 964-968.

Nestrasil, I., Michaeli, S., Liimatainen, T., Rydeen, C.E., Kotz, C.M., Nixon, J.P., Hanson, T., Tuite, P.J., 2010b. T1rho and T2rho MRI in the evaluation of Parkinson's disease. Journal Of Neurology 257, 964-968.

Nguyen, A.M., Johannessen, W., Yoder, J.H., Wheaton, A.J., Vresilovic, E.J., Borthakur, A., Elliott, D.M., 2008. Noninvasive quantification of human nucleus pulposus pressure with use of T1rho-weighted magnetic resonance imaging. Journal Of Bone And Joint Surgery-American Volume 90, 796-802.

Nishioka, H., Hirose, J., Nakamura, E., Oniki, Y., Takada, K., Yamashita, Y., Mizuta, H., 2012. T1rho and T2 mapping reveal the in vivo extracellular matrix of articular cartilage. Journal Of Magnetic Resonance Imaging 35, 147-155.

Oh, M.K., Winn, J., Poordad, F., 2008. Review article: diagnosis and treatment of non-alcoholic fatty liver disease. Aliment Pharmacol Ther 28, 503-522.

Perry, J., Haughton, V., Anderson, P.A., Wu, Y., Fine, J., Mistretta, C., 2006. The value of T2 relaxation times to characterize lumbar intervertebral disks: preliminary results. AJNR Am J Neuroradiol 27, 337-342.

Peterson, C.K., Bolton, J.E., Wood, A.R., 2000. A cross-sectional study correlating lumbar spine degeneration with disability and pain. Spine (Phila Pa 1976) 25,

218-223.

Pfirrmann, C.W., Metzdorf, A., Zanetti, M., Hodler, J., Boos, N., 2001. Magnetic resonance classification of lumbar intervertebral disc degeneration. Spine (Phila Pa 1976) 26, 1873-1878.

Phillips, F.M., An, H., Kang, J.D., Boden, S.D., Weinstein, J., 2003. Biologic treatment for intervertebral disc degeneration: summary statement. Spine (Phila Pa 1976) 28, S99.

Poniachik, J., Bernstein, D.E., Reddy, K.R., Jeffers, L.J., Coelho-Little, M.E., Civantos, F., Schiff, E.R., 1996. The role of laparoscopy in the diagnosis of cirrhosis. Gastrointestinal Endoscopy 43, 568-571.

Poptani, H., Duvvuri, U., Miller, C.G., Mancuso, A., Charagundla, S., Fraser, N.W., Glickson, J.D., Leigh, J.S., Reddy, R., 2001. T1rho imaging of murine brain tumors at 4 T. Academic Radiology 8, 42-47.

Proctor, E., Chatamra, K., 1983. Controlled induction of cirrhosis in the rat. Br J Exp Pathol 64, 320-330.

Ratziu, V., Charlotte, F., Heurtier, A., Gombert, S., Giral, P., Bruckert, E., Grimaldi, A., Capron, F., Poynard, T., 2005. Sampling variability of liver biopsy in nonalcoholic fatty liver disease. Gastroenterology 128, 1898-1906.

Regatte, R.R., Akella, S.V., Lonner, J.H., Kneeland, J.B., Reddy, R., 2006. T1rho

relaxation mapping in human osteoarthritis (OA) cartilage: comparison of T1rho with T2. Journal Of Magnetic Resonance Imaging 23, 547-553.

Salameh, N., Larrat, B., Abarca-Quinones, J., Pallu, S., Dorvillius, M., Leclercq, I., Fink, M., Sinkus, R., Van Beers, B.E., 2009. Early detection of steatohepatitis in fatty rat liver by using MR elastography. Radiology 253, 90-97.

Santyr, G.E., Fairbanks, E.J., Kelcz, F., Sorenson, J.A., 1994. Off-resonance spin locking for MR imaging. Magn Reson Med 32, 43-51.

Santyr, G.E., Henkelman, R.M., Bronskill, M.J., 1989. Spin locking for magnetic resonance imaging with application to human breast. Magn Reson Med 12, 25-37.

Sirlin, C.B., 2011. Science to practice: Can T1rho imaging be used to diagnose and assess the severity of hepatic fibrosis? Radiology 259, 619-620.

Solomon, I., 1959. Rotary spin echoes. Physical Review Letters, 301-302.

Szyperski, T., Luginbuhl, P., Otting, G., Guntert, P., Wuthrich, K., 1993. Protein dynamics studied by rotating frame 15N spin relaxation times. Journal Of Biomolecular Nmr 3, 151-164.

Tailor, D.R., Baumgardner, J.E., Regatte, R.R., Leigh, J.S., Reddy, R., 2004. Proton MRI of metabolically produced H2 17O using an efficient 17O2 delivery

system. Neuroimage 22, 611-618.

Tailor, D.R., Roy, A., Regatte, R.R., Charagundla, S.R., McLaughlin, A.C., Leigh, J.S., Reddy, R., 2003. Indirect 17(O)-magnetic resonance imaging of cerebral blood flow in the rat. Magn Reson Med 49, 479-487.

Talwalkar, J.A., Yin, M., Fidler, J.L., Sanderson, S.O., Kamath, P.S., Ehman, R.L., 2008. Magnetic resonance imaging of hepatic fibrosis: emerging clinical applications. Hepatology 47, 332-342.

Tomassoni, D., Bramanti, V., Amenta, F., 2010. Expression of aquaporins 1 and 4 in the brain of spontaneously hypertensive rats. Brain Research 1325, 155-163.

Tsukamoto, H., Matsuoka, M., French, S.W., 1990. Experimental models of hepatic fibrosis: a review. Seminars In Liver Disease 10, 56-65.

Tsushima, H., Okazaki, K., Takayama, Y., Hatakenaka, M., Honda, H., Izawa, T., Nakashima, Y., Yamada, H., Iwamoto, Y., 2011. Evaluation of cartilage degradation in arthritis using T1rho magnetic resonance imaging mapping. Rheumatology International.

Vadala, G., Sowa, G.A., Kang, J.D., 2007. Gene therapy for disc degeneration. Expert Opin Biol Ther 7, 185-196.

van Zijl, P.C., Yadav, N.N., 2011. Chemical exchange saturation transfer (CEST): what is in a name and what isn't? Magn Reson Med 65, 927-948.

Veldhuijzen, I.K., Toy, M., Hahne, S.J., De Wit, G.A., Schalm, S.W., de Man, R.A., Richardus, J.H., 2010. Screening and early treatment of migrants for chronic hepatitis B virus infection is cost-effective. Gastroenterology 138, 522-530.

Videman, T., Battie, M.C., Gibbons, L.E., Maravilla, K., Manninen, H., Kaprio, J., 2003. Associations between back pain history and lumbar MRI findings. Spine (Phila Pa 1976) 28, 582-588.

Wallace, K., Burt, A.D., Wright, M.C., 2008. Liver fibrosis. Biochemical Journal 411, 1-18.

Wang, H., Li, J., Chen, F., De Keyzer, F., Yu, J., Feng, Y., Nuyts, J., Marchal, G., Ni, Y., 2010. Morphological, functional and metabolic imaging biomarkers: assessment of vascular-disrupting effect on rodent liver tumours. European Radiology 20, 2013-2026.

Wang, Y.X., 2005. Medical imaging in pharmaceutical clinical trials: what radiologists should know. Clinical Radiology 60, 1051-1057.

Wang, Y.X., Griffith, J.F., 2010. Effect of menopause on lumbar disk degeneration: potential etiology. Radiology 257, 318-320.

Wang, Y.X., Griffith, J.F., Ma, H.T., Kwok, A.W., Leung, J.C., Yeung, D.K., Ahuja, A.T., Leung, P.C., 2011b. Relationship between gender, bone mineral density, and disc degeneration in the lumbar spine: a study in elderly subjects

using an eight-level MRI-based disc degeneration grading system. Osteoporos Int 22, 91-96.

Wang, Y.X., Kwok, A.W., Griffith, J.F., Leung, J.C., Ma, H.T., Ahuja, A.T., Leung, P.C., 2011c. Relationship between hip bone mineral density and lumbar disc degeneration: a study in elderly subjects using an eight-level MRI-based disc degeneration grading system. Journal Of Magnetic Resonance Imaging 33, 916-920.

Wang, Y.X., Yan, S.X., 2008. Biomedical imaging in the safety evaluation of new drugs. Lab Anim 42, 433-441.

Wang, Y.X., Yuan, J., Chu, E.S., Go, M.Y., Huang, H., Ahuja, A.T., Sung, J.J., Yu, J., 2011a. T1rho MR imaging is sensitive to evaluate liver fibrosis: an experimental study in a rat biliary duct ligation model. Radiology 259, 712-719.

Wang, Y.X., Yuan, J., Chu, E.S., Go, M.Y., Huang, H., Ahuja, A.T., Sung, J.J., Yu, J., 2011d. T1rho MR imaging is sensitive to evaluate liver fibrosis: an experimental study in a rat biliary duct ligation model. Radiology 259, 712-719.

Wang, Y.X., Zhao, F., Griffith, J.F., Mok, G.S., Leung, J.C., Ahuja, A.T., Yuan, J., 2013a. T1rho and T2 relaxation times for lumbar disc degeneration: an in

vivo comparative study at 3.0-Tesla MRI. European Radiology 23, 228-234.

Wang, Y.X., Zhao, F., Yuan, J., Mok, G.S., Ahuja, A.T., Griffith, J.F., 2013b. Accelerated T1rho relaxation quantification in intervertebral disc using limited spin-lock times. Quant Imaging Med Surg 3, 54-58.

Wanless, I.R., Nakashima, E., Sherman, M., 2000. Regression of human cirrhosis. Morphologic features and the genesis of incomplete septal cirrhosis. Archives Of Pathology & Laboratory Medicine 124, 1599-1607.

Ward, K.M., Aletras, A.H., Balaban, R.S., 2000. A new class of contrast agents for MRI based on proton chemical exchange dependent saturation transfer (CEST). Journal Of Magnetic Resonance 143, 79-87.

Weidenbaum, M., Foster, R.J., Best, B.A., Saed-Nejad, F., Nickoloff, E., Newhouse, J., Ratcliffe, A., Mow, V.C., 1992. Correlating magnetic resonance imaging with the biochemical content of the normal human intervertebral disc. Journal Of Orthopaedic Research 10, 552-561.

Witschey, W.R., Zsido, G.A., Koomalsingh, K., Kondo, N., Minakawa, M., Shuto, T., McGarvey, J.R., Levack, M.A., Contijoch, F., Pilla, J.J., Gorman, J.H., Gorman, R.C., 2012. In vivo chronic myocardial infarction characterization by spin locked cardiovascular magnetic resonance. J Cardiovasc Magn Reson 14, 37.

Yankner, B.A., Lu, T., Loerch, P., 2008. The aging brain. Annu Rev Pathol 3, 41-66.

Yuan, J., Zhao, F., Griffith, J.F., Chan, Q., Wang, Y.X., 2012. Optimized efficient liver T(1rho) mapping using limited spin lock times. Physics In Medicine And Biology 57, 1631-1640.

Zhou, K., Lu, L.G., 2009. Assessment of fibrosis in chronic liver diseases. J Dig Dis 10, 7-14.

LIST OF PUBLICATIONS

Journal Publications

1. **Zhao F**, Wang YX, Yuan J, Deng M, Wong HL, Chu ES, Go MY, Teng GJ, Ahuja AT, Yu J. MR T1ρ as an imaging biomarker for monitoring liver injury progression and regression: an experimental study in rats with carbon tetrachloride intoxication. Eur Radiol. 2012; 22(8):1709-16.
2. **Zhao F**, Deng M, Yuan J, Teng GJ, Ahuja AT, Wang YX. Experimental evaluation of accelerated t1rho relaxation quantification in human liver using limited spin-lock times. Korean J Radiol. 2012;13(6):736-42.
3. Deng M, **Zhao F^**, Yuan J, Ahuja AT, Wang YX. Liver T1ρ MRI measurement in healthy human subjects at 3 T: a preliminary study with a two-dimensional fast-field echo sequence. Br J Radiol. 2012;85(1017): e590-5. (^:Co-first author).
4. **Zhao F,** Yan SX, Wang GF, Wang J, Lu PX, Chen B, Yuan J, Zhang SZ, Wang YX. CT features of focal organizing pneumonia: An analysis of consecutive histopathologically confirmed 45 cases. Euro J Radiol. 2013, http://dx.doi.org/10.1016/j.ejrad.2013.04.017
5. **Zhao F,** Lu PX, Yan SX, Wang GF, Yuan J, Zhang SZ, Wang YX. CT and MR features of xanthogranulomatous cholecystitis: An analysis of consecutive 49 cases.

Euro J Radiol. 2013, http://dx.doi.org/10.1016/j.ejrad.2013.04.026

6. Wang YX, **Zhao F**, Griffith JF, Mok GS, Leung JC, Ahuja AT, Yuan J. T1rho and T2 relaxation times for lumbar disc degeneration: an in vivo comparative study at 3.0-Tesla MRI. Eur Radiol. 2013;23(1):228-34.

7. Yuan J, **Zhao F**, Griffith JF, Chan Q, Wang YX. Optimized efficient liver T(1ρ) mapping using limited spin lock times. Phys Med Biol. 2012;57(6):1631-40.

8. Yuan J, **Zhao F**, Chan Q, Wang YX. Observation of bi-exponential T1ρ relaxation of in-vivo rat muscles at 3T. Acta Radiol. 2012;53(6):675-81.

9. Yuan J, Li Y, **Zhao F**, Chan Q, Ahuja AT, Wang YX. Quantification of T(1ρ) relaxation by using rotary echo spin-lock pulses in the presence of B(0) inhomogeneity. Phys Med Biol. 2012;57(15):5003-5016.

10. Shi L, Wang YX, Yu C, **Zhao F**, Kuang PD, Shao GL. CT and ultrasound features of basal cell adenoma of the parotid gland: a report of 22 cases with pathologic correlation. AJNR Am J Neuroradiol. 2012;33(3):434-8.

11. Zhu XM, Wang YX, Leung KCF, Lee SF, **Zhao F**, Wang DW, Lai JMY, Wan C, Cheng CHK, Ahuja AT Enhanced cellular uptake of aminosilane-coated superparamagnetic iron oxide nanoparticles in mammalian cell lines. International Journal of Nanomedicine 2012:7 953–964.

12. Wang Y, Li L, Wang YX, Feng XL, **Zhao F**, Zou SM, Hao YZ, Ying JM, Zhou

CW. Ultrasound Findings of Papillary Thyroid Microcarcinoma: A Review of 113 Consecutive Cases with Histopathologic Correlation. Ultrasound Med Biol. 2012;38(10):1681-8.

13. Zhang L, Yu WH, Wang YX, Wang C, **Zhao F**, Qi W, Chan WM, Huang Y, Wai MS, Dong J, Yew DT. DL-3-N-Butylphthalide, an Anti-Oxidant Agent, Prevents Neurological Deficits and Cerebral Injury Following Stroke per Functional Analysis, Magnetic Resonance Imaging and Histological Assessment. Curr Neurovasc Res. 2012;9(3):167-75.

14. Dai XJ, Gong HH, Wang YX, Zhou FQ, Min YJ, **Zhao F**, Wang SY, Liu BX, Xiao XZ. Gender differences in brain regional homogeneity of healthy subjects after normal sleep and after sleep deprivation: a resting-state fMRI study. Sleep Med. 2012;13(6):720-7.

Conference Proceedings

1. Feng Zhao, Li-Hong Zhang, Jing Yuan, Queenie Chan, David Yew, and Yi-Xiang Wang. T1rho measurement in rat brain tissue changes associated with aging and chronic hypertension, 21st ISMRM, 2013. 2875.

2.Feng Zhao, Jing Yuan, Min Deng, and Yi-Xiang Wang. Further exploration of MRI techniques for liver T1rho quantification. 21st ISMRM, 2013. 4092.

3. Feng Zhao, Jing Yuan, Domily Ting Yi Lau, David Ka Kwai Yeung, Yi-Xiang J

Wang, Anil T Ahuja, James F Griffith. Small field-of-view high-resolution MR imaging of talar dome at 3T: A comparison of 2D TSE and SSFP sequences, 1st ICMRI & 18th KSMRM,2013.

4.Feng Zhao, Jing Yuan, Jiu Tian, Gang Lu, and Wai Sang Poon , Yi-Xiang Wang. A longitudinal study on age-related changes of T1rho relaxation in rat brain, 20th ISMRM, 2012. 0453. (MAGA)

5.Feng Zhao, Min Deng, Jing Yuan, Jun Yu, Yi-Xiang Wang.T1rho MR imaging for rat liver with carbon tetrachloride intoxication: a time course study, 20th ISMRM, 2012. 0690.

6.Feng Zhao, Li-Hong Zhang, Jing Yuan, Queenie Chan, David Yew, Yi-Xiang Wang. A comparative study of brain regional T1rho values of spontaneously hypertensive rat and Wistar Kyoto rat, 20th ISMRM, 2012. 0347.

7.Feng Zhao, Hong-Jian He, Xiao-jing Yu, Yi-Xiang Wang, Shi-Zheng Zhang. Imaginary toe-tapping causes classic motor hand area activation in bilateral upper limb amputees,19th ISMRM, 2011. 3647.

8. Li Y, **Zhao F**, Wang YX, Ahuja AT, Yuan J. Study of magnetization evolution by using composite spin-lock pulses for T(1ρ) imaging. Conf Proc IEEE Eng Med Biol Soc. 2012 Aug;2012:408-11. doi: 10.1109/EMBC.2012.6345954.

9. Wang Yi-Xiang, **Zhao Feng**, Griffith James F., Mok Greta SP, Chan Queenie, Yuan

Jing. An In Vivo Comparative Study of T1rho and T2 Relaxation Times for Evaluation of Lumber Disc Degeneration at 3.0 Tesla MRI, 20th ISMRM, 2012. 0354.

10. Wang, Yi-Xiang; **Zhao, Feng**; Wong, Vincent Wai Sun; Yuan, Jing; Kwong, Kin Ming; Chan, Henry Lik Yuen. Liver MR T1rho Measurement in Liver Cirrhosis Patients: A Preliminary Study with a 2D Fast Field Echo Sequence at 3T. 20th ISMRM, 2012. 0213.

11. Pu-Xuan Lu, **Feng Zhao**, Jing Yuan, Greta SP Mok, James F Griffith, and Yi-Xiang Wang. Accelerated T1rho relaxation quantification in intervertebral disc using limited spin-lock times, 21st ISMRM, 2013. 3476.

12. Yuan Jing, Liang Dong, **Zhao Feng**, Li Yujia, Wang Yi-Xiang J., Ying Leslie. k-T ISD Compressed Sensing Reconstruction for T1ñ Mapping: A Study in Rat Brains at 3T. 20th ISMRM, 2012. 0939.

13. Pu-Xuan Lu, Hua Huang, Jing Yuan, **Feng Zhao**, and Yi-Xiang Wang. Intravoxel Incoherent Motion MR Imaging showed lower pure molecular diffusion in fibrotic livers: a report of preliminary results, 21st ISMRM, 2013. 4081.

14. Zhu Xiao-Ming, Leung Ken Cham-Fai, Lee Siu-Fung, Wang Da-Wei, **Zhao Feng**, Lai Josie M. Y., Wan Chao, Cheng Christopher H. K., Wang Yi-Xiang. Enhanced Cellular Uptake of Aminosilane Coated Superparamagnetic Iron Oxide

Nanoparticles in Mammalian Cell Lines, 20th ISMRM, 2012. 0641.